

https://dspace.org/

Improving the resilience of Free-Space Optical links using structured modes of light

Cox, Mitchell Arij

2020
https://hdl.handle.net/10539/30610

Downloaded from a DSpace repository. https://dspace.org/



UNIVERSITY OF THE
WITWATERSRAND,
JOHANNESBURG

Improving the Resilience of Free-Space Optical Links using Structured Modes of Light

Mitchell Arij Cox

ORCiD: 0000-0002-1115-3729

A thesis submitted to the Faculty of Engineering and the Built Environment, University of the Witwatersrand, Johannesburg, in fulfilment of the requirements for the degree of Doctor of Philosophy.

2019

Declaration

I, the undersigned, hereby declare that the work contained in this thesis is my own original work and that I have not previously in its entirety or in part submitted it at any university for a degree.



Mitchell Arij Cox

Braamfontein, Johannesburg
3 December 2019

Abstract

The work presented extends and contributes to research in mitigating the effects of turbulence in long-range Free Space Optical (FSO) links using structured modes of light. While there is an extensive body of existing research in the use of Orbital Angular Momentum (OAM) modes for mode division multiplexed communication channels, there has not been an investigation into the use of alternative mode sets and their resilience to atmospheric turbulence. In this thesis several different approaches are investigated, each with a corresponding journal publication.

In the research presented it is found that a carefully chosen subset of Hermite-Gauss modes are significantly more resilient to propagation in turbulence than the more commonly used Laguerre-Gauss modes. Knowledge of this independence is exploited in a "modal diversity" proof-of-principle system which is shown to be effective - an intriguing result which exposes several questions about the propagation of higher order modes in turbulence. In this research it is also found that the resilience of vector vortex modes over scalar vortex modes is in fact a misconception and the choice of mode set for FSO should not be based on its vectorial nature.

Motivated by the predominant effects of beam wander in the previous investigations, it is shown that turbulence-induced beam wander is neither a memoryless nor a first order memory system as expected when Taylor's frozen-turbulence model is invoked. A more accurate modelling approach for the time-varying nature of turbulence induced beam wander is presented which may be used to design optimised mode sets and digital signal processing schemes in future FSO systems.

Acknowledgements

First and foremost, thank you to Andrew Forbes and Ling Cheng for their fantastic supervision, mentorship and support over the duration of this PhD research. Through them, I have learnt many valuable lessons and been able to form a strong local and international network, which puts me in good stead for my academic career. I hope that we will continue our productive collaboration long into the future. I am also grateful to Jaco Versfeld for his supervision in the first year of my PhD.

Of course, my postgraduate and lately my academic career would not have been possible were it not for the support of my girlfriend and now my wife, Gillian! Thank you for the flexibility and understanding when I had to work late and when I had to leave you at home when I was off travelling the world... Thank you also to my friends and family for enabling me to get to this point in the first place.

On a more formal note, I would like to acknowledge the support of the South African National Research Foundation for their financial support in the first year of my PhD and to The School of Electrical and Information Engineering for employing me and therefore enabling me to restart my career while pursuing my passion for research. I trust that I have been a good employee so far! Another thank you to my supervisors (and indirectly whoever they received their grants from) for the financial support, allowing me to spend large sums of money on equipment, "consumables" and for attending excellent conferences.

Contents

Declaration i

Abstract ii

Acknowledgements iii

List of Figures vi

List of Acronyms x

Resulting Publications xii

1 Introduction 1
- 1.1 Research Question and Contributions . . . 3

2 Background 5
- 2.1 Spatial Modes of Light . . . 6
  - 2.1.1 Gaussian Beams . . . 7
  - 2.1.2 Higher Order Beams . . . 8
  - 2.1.3 Detection of Higher Order Modes . . . 10
- 2.2 Atmospheric Attenuation . . . 11
- 2.3 Atmospheric Turbulence . . . 12
  - 2.3.1 Temporal Effects . . . 15
  - 2.3.2 Turbulence Induced Fading Models . . . 15
  - 2.3.3 Turbulence Induced Modal Crosstalk Models . . . 16

3 The Resilience of Hermite- and Laguerre-Gauss Modes in Turbulence 17
- 3.1 Preliminaries . . . 18
  - 3.1.1 Laguerre- and Hermite-Gaussian Modes . . . 18
  - 3.1.2 Atmospheric Turbulence . . . 20
- 3.2 Experimental Setup and Methodology . . . 21
- 3.3 Results and Discussion . . . 23
- 3.4 Conclusion . . . 25

4 On the Resilience of Scalar and Vector Vortex Modes in Turbulence 26
- 4.1 Theory . . . 27
  - 4.1.1 Inter-mode crosstalk . . . 28
- 4.2 Experiment . . . 29
- 4.3 Results and discussion . . . 30

4.4 Conclusion 31

5 Modal Diversity for Robust Free-Space Optical Communications 33
5.1 Channel Model 34
5.2 Experiment 36
5.2.1 Choice of Modes for Diversity 36
5.2.2 Experimental Setup 36
5.3 Results and Discussion 37
5.4 Conclusion 39

6 Modelling the Memory of Turbulence-Induced Beam Wander 40
6.1 Existing Beam Wander Models 41
6.2 Methods 42
6.2.1 Experimental Setup 42
6.2.2 ARMA-based Memory Model 43
6.3 Fitting the Memory Model 44
6.4 Modelling Beam-Wander Induced Fading 45
6.5 Modelling Memory and Deep Fading 46
6.6 Modelling Mode Crosstalk 48
6.7 Conclusion 49

7 Conclusion 50

References 53

List of Figures

2.1 Simplified schematic of a typical FSO link. The Rayleigh range is labelled as z_R and a telescope arrangement is used at the transmitter and receiver. A turbulence phase screen, described in Sec. 2.3, is illustrated at the center of the link. 6

2.2 Left: The propagation of a Gaussian beam with the beam waist (with radius ω_0) in the centre. Right: An intensity profile of a Gaussian beam indicating the approximate position of the beam radius, w. The red line above the profile indicates the amplitude of the beam, $|U|$, and is the square root of the intensity. 7

2.3 Examples of LG and HG modes showing intensity (amplitude squared) and phase. The phase colourmap of the LG modes represents a 0 to 2π phase change (blue to yellow) and a 0 and π for the HG modes (blue and yellow). The intensity colourmap is 0 to 1 (blue to yellow). 9

2.4 Example atmospheric transmittance of different wavelengths due to molecular absorption in the atmosphere according to the LOWTRAN7 model [69]. 11

2.5 Example Kolmogorov turbulence screens with varying strength. A raw turbulence screen is shown in (a), however, when the screen is used on a digital hologram a grating is applied. Frames (b) to (d) show turbulence screens from weak to strong with gratings applied. 13

2.6 Example OAM crosstalk for no turbulence (SR = 1.0), weak turbulence (SR = 0.7) and strong turbulence (SR = 0.1) showing increasing crosstalk with turbulence strength. The crosstalk normalisation for the higher order modes (for example $\ell = \pm 2$) is inaccurate. 14

3.1 Modes used in the experiment, with wavefront to the left and intensity to the right of each, corresponding to Tab. 3.1. The arrows in the centre indicate the translational (or rotational) axis where the mode is robust and will still be detected correctly. The HG_1^1 mode does not have a robust axis. 19

3.2 Modal decomposition setup with sample insets of the holograms used: (a) LG_1^0, (b) HG_1^0 and (c) BHG_1^0. 21

3.3 Experimental setup verification showing the crosstalk matrices for the various mode sets at different turbulence strengths. Top: no turbulence (SR=1.0). Middle: mild turbulence (SR=0.7). Bottom: strong turbulence (SR=0.1). Mode groups corresponding to modes in Fig. 3.1 and Tab. 3.1 are highlighted as it is clear that there is relatively little crosstalk within each group. 22

3.4 Mode Dependent Loss (top) and Crosstalk (bottom) of the LG, HG and Binary HG mode sets for different turbulence strengths form strong turbulence (SR=0.1) to no turbulence (SR=1.0). The shaded area of each curve represents the measurement error. From Tab. 3.1, the 3^* case excludes the HG_1^1 mode and is shown as the additional HG* and BHG* curves. 23
3.5 Effective propagation distance calculated from the Strehl Ratio using Eqs. 3.9 and 3.12 for the average ($M^2 = 1$, 2 and 3^*) of each mode set. At the vertical dotted line the difference between HG and LG is 51 km and BHG and LG is 12 km. This represents an upper bound due to weak turbulence alone as aperture collection losses due to divergence and beam wander are neglected, as are atmospheric attenuation effects such as aerosol scattering. 23
3.6 Experimental images of Gaussian beam wander in the far field of the turbulence screen. The top left image is the beam without turbulence. . . 25

4.1 Illustration of the scalar (top) and Cylindrical Vector Vortex (CVV) (bottom) modes described in Eq. 4.1 and Eq. 4.2 respectively, with arrows indicating polarisation distribution which is constant for scalar and variable for CVV modes, for $\ell = \pm 1$. The phase of the four scalar modes in the transverse plane increases from $-\pi$ (red) to π (blue) for positive ℓs and decreases in the opposite direction for negative ℓs whereas the phase for CVV modes is a superposition of both. 27
4.2 Simplified schematic diagram of the experimental setup showing the three main parts. The polarisation invariant Spatial Light Modulator (SLM) is made up by a Polarising Beam Splitter (PBS), mirror and half wave plate rotated to 45° so that arbitrarily polarised scalar and vector beams can be modulated by the SLM, which is encoded with random Kolmogorov turbulence screens. The perturbed beams which return along the same path as the incoming beams are directed by a Beam Splitter (BS) to the detection part of the setup which performs modal decomposition. 29
4.3 Comparison of vector and scalar crosstalk for $SR = 1.0$ (top) for experimental setup validation and $SR = 0.6$ (middle) and $SR = 0.2$ (bottom). . 30
4.4 Percentage of the signal in the crosstalk of scalar and vector cases showing insets of the beam with increasing turbulence. Both mode sets have the same crosstalk performance. Error bars are the standard error of the mean. 31

5.1 Illustrative comparison of spatial multiplexing which is used for increased bandwidth (top left), conventional spatial diversity which is used for increased robustness (top right) and our modal diversity scheme which does not require path separation (bottom). In conventional diversity the transmitted beams, irrespective of mode, take different paths separated by some distance greater than r_0. In modal diversity, different modes are used with half the original transmit power (g_i) but with each travelling the same path: the separation is in mode space not physical space. 34

5.2 Experimental demonstration of the orthogonality of HG_2^2 and LG_2^1 modes with no turbulence (SR $= 1.0$ or $D/R_0 < 0.01$) and slight turbulence (SR $= 0.95$ or $D/r_0 = 0.05$) with measurement points shown as "+". On the left, only an HG_2^2 is transmitted and it is clear that there is no LG_2^1 component after modal decomposition. Similarly, on the right there is an LG_2^1 component but no HG_2^2 component in the decomposed beam. . . . 35
5.3 Experimental setup showing two transmitters and a single receiver for transmit diversity with example turbulence as an inset (a). The holograms along the bottom are for (b) generating an $LG_{\ell=2}^{p=1}$ beam, (c) generating an $HG_{n=2}^{m=2}$ beam and (d) superposition for decomposition of the generated LG and HG beams to a single detector. The flat grey areas on the holograms is due to complex amplitude modulation. 35
5.4 Bit Error Rate of modes with order $N = 4$ and 8 where $D = 1.4$ and 1.98 mm respectively with varying turbulence strength showing a clear improvement for the diversity cases. Larger modes are expected to experience lower turbulence in comparison to smaller modes. 37
5.5 Bit Error Rate of modes with order $N = 4$ and 8 with varying turbulence strength in terms of the Strehl Ratio for $D = 1.4$ mm. The diversity case is typically better than the non diversity cases with significant gains in weaker turbulence. 38

6.1 (a) Simplified schematic diagram of the experimental setup with insets of the beam intensity at the transmitter and receiver. (b) A diagram that illustrates the relationship between short- and long-term beam wander parameters. 43
6.2 Experimental measurements of the beam wander showing a plot of the centroid position in (a), the long-term beam in (b) and sample short term beam images in (c). 44
6.3 (a) A short sample of the beam wander in x. (b) Scatter plots showing temporal correlation between samples at $t-1$, some correlation at $t-3$ but no correlation at $t-10$. (c) Auto-correlation and partial auto-correlation plots of the data with the 95% significance region shaded (± 0.037). 45
6.4 Plots to show that the residuals of the model and the measured samples are white Gaussian noise. (a) The ACF and PACF indicate no correlations. (b) A short sample of the standardised residuals showing no visible pattern. (c) The histogram of the residuals has a random Gaussian characteristic shape. 46
6.5 Plots to demonstrate the fading statistics of the model in comparison to experimental data. (a) and (b) are PDFs of simulated and measured intensities with an overlay (orange) of the theoretical PDF showing excellent agreement with existing theory. (c) Simulated beam wander positions with the resulting long-term intensity in (d). 47
6.6 Run length distribution plots of the simulated ARMA model and the experimental measurements with a transition threshold set at 50% intensity for illustrative purposes. Overlaid on the plots in green is the run length distribution of data simulated using the conventional PDF-based model which clearly does not match the experimental measurements. 48

6.7 (Top) Mode crosstalk from the transmitted Gaussian mode ($\ell = 0$) into OAM modes $\ell = -5$ to 5 due to lateral displacement over time. (Bottom) The corresponding normalised beam wander radii, r_c. The highlighted section shows good examples of crosstalk with well aligned (minimal crosstalk) and misaligned (high crosstalk) cases. 49

List of Acronyms

ADSL Asynchronous Digital Subscriber Line

AWGN Additive White Gaussian Noise

BER Bit Error Rate

BHG Binary Hermite-Gauss

BS Beam Splitter

CVV Cylindrical Vector Vortex

DWDM Dense Wavelength Division Multiplexing

FEC Forward Error Correction

FSO Free Space Optical

FTTH Fibre To The Home

Gbps Gigabits per second

HG Hermite-Gauss

HWP Half-Wave Plate

LEO Low Earth Orbit

LG Laguerre-Gauss

Mbps Megabits per second

MD Modal Decomposition

MDL Mode Dependent Loss

MDM Mode Division Multiplexing

MIMO Multiple Input Multiple Output

NIR Near Infrared

OAM Orbital Angular Momentum

PBS Polarising Beam Splitter

PDF Probability Distribution Function

QKD Quantum Key Distribution

QWP Quarter-Wave Plate

SDM Space Division Multiplexing

SISO Single Input Single Output

SLM Spatial Light Modulator

SMF Single Mode Fibre

SNR Signal to Noise Ratio

SR Strehl Ratio

WDM Wavelength Division Multiplexing

Resulting Publications

Journal Papers

1. M. A. Cox, L. Maqondo, R. Kara, G. Milione, L. Cheng and A. Forbes, "The Resilience of Hermite- and Laguerre-Gaussian Modes in Turbulence," *Journal of Lightwave Technology*, vol. 37, no. 16, pp. 3911–3917, 2019. (Invited Paper)
2. M. A. Cox, L. Cheng, C. Rosales-Guzmán and A. Forbes, "Modal Diversity for Robust Free-Space Optical Communications," *Physical Review Applied*, vol. 10, no. 2, p. 024020, 2018.
3. M. A. Cox, C. Rosales-Guzmán, M. P. J. Lavery, D. J. Versfeld and A. Forbes, "On the resilience of scalar and vector vortex modes in turbulence," *Optics Express*, vol. 24, no. 16, p. 18105, 2016.
4. M. P. J. Lavery, M. M. Abadi, R. Bauer, G. Brambilla, L. Cheng, M. A. Cox, A. Dudley, A. D. Ellis, N. K. Fontaine, A. E. Kelly, C. Marquardt, S. Matlhane, B. Ndagano, F. Petruccione, R. Slavík, F. Romanato, C. Rosales-Guzmán, F. S. Roux, K. Roux, J. Wang and A. Forbes, "Tackling Africa's digital divide," *Nature Photonics*, vol. 12, no. 5, pp. 249–252, 2018.
5. B. Ndagano, I. Nape, M. A. Cox, C. Rosales-Guzmán and A. Forbes, "Creation and detection of vector vortex modes for classical and quantum communication," *Journal of Lightwave Technology*, vol. 36, pp. 292–301, 2017. (Invited Paper)
6. C. Kamwangala, M. A. Cox and L. Cheng, "Transmitter power control for a multicarrier visible light communication system," *Transactions in Emerging Telecommunication Technology*, p. e3453, 2018.
7. M. A. Cox, E. Toninelli, L. Cheng, M. J. Padgett and A. Forbes, "A High-Speed, Wavelength Invariant, Single-Pixel Wavefront Sensor With a Digital Micromirror Device," *IEEE Access*, vol. 7, pp. 85860–85866, 2019.
8. E. Toninelli, M. A. Cox et al., "A compact acoustic spanner to rotate macroscopic objects," *Scientific Reports*, vol. 9, no. 1, p. 6757, 2019. URL: http://www.nature.com/articles/s41598-019-43046-4

Under Review

1. M. A. Cox, L. Gailele, L. Cheng and A. Forbes, "Modelling the Memory of Turbulence-Induced Beam Wander," submitted to *Journal of Lightwave Technology*, 2019.
2. M. A. Cox, L. Cheng and A. Forbes, "Measuring the Memory of Turbulence-Induced Beam Wander," submitted to *Optics Express*, 2019.

Selected Conference Proceedings

1. M. A. Cox, L. Cheng and A. Forbes, "Bridging the digital divide: a South African perspective," in Photonic Networks and Devices, Zurich, 2018, p. NeW2F–3. (Invited Talk)
2. M. A. Cox and A. Forbes, "Scalar and Vector Vortex Modes through SLM-based Kolmogorov Turbulence," in Frontiers in Optics, Washington DC, 2017, p. JW4A–7.
3. M. A. Cox, A. Forbes and L. Cheng, "Digital micro-mirror devices for laser beam shaping," in Fifth Conference on Sensors, MEMS, and Electro-Optic Systems, Kruger Park, 2019, vol. 11043, p. 37.

CHAPTER 1

Introduction

COMMUNICATION in the modern era was revolutionised by the invention of the electric telegraph and subsequently the conventional telephone in 1837 and 1876 respectively. The use of the copper and microwave radio infrastructure built for telephones eventually led to the Internet, which is now ubiquitous. In the 1970s, fibre optic communications technology began to replace the existing copper back haul infrastructure due to the fact that it is cheaper, higher bandwidth and longer range [1]. Globally, annual growth rates have been between approximately 30% and 90% since the advent of the internet [2].

In terms of the access network it is clear that consumers were delighted with the service provided by copper wires and even today many Internet users still make use of Asynchronous Digital Subscriber Line (ADSL) instead of Fibre To The Home (FTTH), which is often unavailable. The cost and complexity of upgrading the historical copper infrastructure has been a limiting factor in the deployment of FTTH. For instance, in 2017 according the the FTTH/B Global Rankings from the IDATE for FTTH Council in Europe, the household penetration of FTTH was approximately 17% in the Netherlands, 14% in the United States and only 4% in South Africa. All other continental African countries have less than 1% FTTH penetration.

In developing countries such as those in Africa, access to the Internet with bandwidth sufficient for audio or video streaming, for example, is rare. Africa has 16% of the world's population but only 4% of the internet users. This is the basis of the so-called "digital divide" and is due to various factors both socio-economic and geographic [3]. Using Africa as an example, the distances between human settlements and existing fibre infrastructure can be immense and given that the installation of fibre is expensive, bridging this digital divide in Africa is a significant challenge.

Existing internet infrastructure in Africa, where fibre is not available, is provided by satellite and terrestrial microwave links. Terrestrial microwave links consist of point-to-point, line of sight towers typically situated tens of kilometres apart, depending on the terrain. For instance, on flat ground, two 50 m high towers could be separated by approximately 40 km before the curvature of the Earth becomes an issue. Carrier-grade microwave technology is able to sustain throughputs in the region of 10 Gbps per link.

Current satellite connectivity is also limited by high latencies, low bandwidth and high cost. The fledgling Starlink project by SpaceX, among others, is a commercial attempt to provide world-wide high-speed, low latency access to Internet via thousands of Low Earth Orbit (LEO) satellites [4]. The satellites will rely on a high speed Free Space Optical (FSO) mesh network between each other, but currently require radio for connectivity to the ground.

The ground connectivity will likely be on the order of Megabits per second (Mbps) due to the 550 km altitude. It is unknown whether this technology will be viable for typical consumers, especially those affected by the digital divide.

FSO communication technology may be a viable technology to provide high bandwidth over longer distances, without the expense of installing long distance fibre back haul [3, 5, 6]. Existing high-sites and towers that are currently used for microwave links could be retro-fitted with FSO which can operate in parallel to the existing infrastructure to maintain high availability albeit at lower capacity. This may be seen as an interim technology to bridge the gap until higher bandwidth fibre is installed, in the case of large towns and cities.

Unfortunately, existing commercial in-atmosphere FSO solutions have a limited range of about 2 km at several Gigabits per second (Gbps). It is relatively trivial to increase the bandwidth of a short range FSO system by simply harnessing additional degrees of freedom such as polarisation or wavelength. Approximately one hundred, 10 Gbps (12.5 GHz) channels are available through off the shelf Dense Wavelength Division Multiplexing (DWDM) components [7]. The so-called "capacity crunch", which is due to the bandwidth of fibre optic communications fast approaching the non-linear Shannon limit, has spurred research into the spatial degree of freedom in both fibre and free space [1, 8–11]. There have been multiple demonstrations of extremely high bandwidth but short range FSO communication links as well as numerous theoretical investigations using Mode Division Multiplexing (MDM) [6, 11–13].

MDM is a subset of the degree of freedom afforded by Space Division Multiplexing (SDM), where a physical separation of information carrying beams is created through the use of orthogonal spatial modes which can propagate co-linearly without conventional, "physical" separation. There are numerous modal bases that may be used for MDM, for example Laguerre-Gauss (LG) and Hermite-Gauss (HG) modes. Each of these sets has an infinite number of orthogonal modes, making them attractive for high capacity communication systems. Unfortunately, the long distance challenge for MDM-FSO has not been solved, although there have indeed been some promising demonstrations of MDM links outside a lab environment [14–23].

One of the primary issues with FSO is atmospheric turbulence, which arises from localised changes in temperature and pressure, causing spatial variations in the refractive index of the atmosphere [24–27]. This results in what is typically called optical scintillation and manifests as the random fluctuations (or fading) of the received signal's intensity. For MDM, turbulence also distorts the wavefront resulting in crosstalk, thus reducing the link capacity. It is difficult to mitigate the effects of turbulence and common strategies are to use signal processing techniques such as Multiple Input Multiple Output (MIMO) and strong forward error correction as well as adaptive optics [11, 28]. Channel diversity is another well-known technique where multiple transmitters or receivers are spatially separated to reduce the probability of errors [29–31].

Almost all of the aforementioned high-speed demonstrations have made use of Orbital Angular Momentum (OAM) modes. It has been suggested that the use of OAM modes in isolation do not provide a channel capacity gain but these information theoretical claims may not be completely accurate as they rely on turbulence models that are not physically verified for higher order modes [20, 32–35].

The question of whether there are "better" optical modes, for example modes that may be more resilient to atmospheric turbulence than a standard Gaussian mode, is longstanding as this would be an effective way to passively increase the range of a FSO link. This is also an important goal for quantum systems such as Quantum Key Distribution (QKD) [36]. Typical beams that have been well investigated in turbulence are OAM or LG modes, Bessel-Gauss modes and also vector modes with spatially varying polarisation, with varying degrees of success [37–41]. In general it has been found that higher order modes are indeed more resilient than Gaussian modes [38]. In the presence of a restricted aperture, LG (often colloquially referred to as OAM) modes have a larger information capacity than HG modes [42], but if this is not the case then HG modes are a promising candidate as they are robust

against lateral displacements (or beam wander) and angle of arrival aberrations [35, 43–45].

The range and capacity of FSO links are inextricably linked. While there has been much work in increasing the bandwidth of FSO links, there has been very little work in increasing their range, which is critical to their versatility. The focus of this PhD is therefore on increasing the range of free space optical communication links. As this is an extremely large field, this work is focused on the physical aspects of a FSO link rather than digital techniques.

This thesis is structured into chapters that individually address the research questions in Sec. 1.1 below. There is some overlap in the introductions to each chapter to provide context for the work within. In Chapter 2, a broad background of FSO is provided in order to supplement the readers understanding of subsequent chapters, which are largely self contained due to the fact that they are based on publications. General topics such as spatial modes of light, atmospheric attenuation and atmospheric turbulence are summarised. Chapter 7 provides a summary and conclusions of the findings present in this thesis and suggests some future avenues of research.

1.1 Research Question and Contributions

The ability to achieve more robust FSO communication "passively" (rather, optically), before the use of DSP, MIMO, FEC and other digital techniques, would be highly beneficial. Firstly, lower error rates could be achieved, which is especially important to ultra high bit-rate communication. At multi-terabit bit-rates, which is the current state-of-the-art for a single optical channel, digital processing resources are an extremely valuable and scarce resource [1]. As a result, it is not always possible to implement robust error correction that is capable of operating in real-time, for instance. Secondly, if extremely high speed is not a priority, the range of a link can be increased within similar error margins. To this end, the overarching question driving this PhD research is as follows:

How can spatial modes of light be used to improve the resilience of laser-based free-space optical communication to atmospheric turbulence?

The research is focused on several high-impact sub-questions, each of which forms part of the overall contribution of the thesis.

1. *Is there a specific mode set that is more robust than other sets in atmospheric turbulence?*

   There are numerous sets of modes that can be used for FSO communications. LG modes are the most widely used, probably due to the ease with which they can be created and detected for MDM. HG modes have not been as rigorously studied in FSO communications, but due to their symmetry we hypothesised that they should be more robust to beam wander than LG modes. It was found that this is indeed the case and the results have published and details of the research can be found in Chapter 3 [35].

2. *Are vector modes more resilient to atmospheric turbulence than scalar modes?*

   In existing literature it is commonly implied that so-called vector vortex modes (modes with a spatially varying polarisation) are more robust to atmospheric turbulence aberrations than their scalar counterparts (modes with uniform polarisation). Only weak arguments on the topic have been put forward, however, if true, vector modes would be an excellent way to increase the range of FSO links. In light of this, we have shown that there is in fact no significant difference between the two types of modes in atmospheric turbulence insofar as modal crosstalk is concerned, and the publication of this result has been highly cited so far [40, 46]. This work is described in Chapter 4.

3. *Given that HG modes are more robust than LG modes in turbulence, can this independence be used to achieve "modal diversity", without the conventionally required r_0 physical separation of the co-propagating beams?*

   Since the wavefronts of HG and LG beams are significantly different, when they co-propagate through turbulence we hypothesise that they will experience independent aberrations. If the two beams do in fact experience independent aberrations then there will be a diversity gain, which will manifest as an improvement in Bit Error Rate (BER). One consequence of this would be significantly more robust FSO systems in the same form-factor as existing systems; no additional apertures are required for "modal diversity" as opposed to standard "spatial diversity" schemes. This hypothesis was tested and shown to be feasible with details in Chapter 5 [47].

4. *Several of the conclusions drawn from the previous research questions can be attributed to the effects of turbulence-induced beam wander. Existing models for beam wander assume a memoryless random system. Is there a more accurate model for the time-varying nature of beam wander?*

   The dynamics of beam wander can be used to explain the difference in propagation performance of HG and LG modes in turbulence. In addition, if beam wander is a memory process, the dynamics can be used to explain the slow-fading, "burstiness" of the FSO channel - one of the main reasons why long distance, high speed communications is so challenging.

   In Chapter 6, it is found that existing memoryless, or single order memory models brought about by Taylor's frozen turbulence hypothesis for beam wander are insufficient. A more accurate memory modelling approach for turbulence-induced beam wander is presented based on experimental measurements. This model may be useful in developing optimised burst error correcting codes and perhaps even less computationally complex diversity schemes and MIMO. The work has been submitted for publication in The Journal of Lightwave Technology.

CHAPTER 2

Background

THIS chapter provides a general background on Free Space Optical (FSO) communication systems, as well as some optical theory that is applicable to this thesis. The focus is on the physical aspects of the system rather than electronics, communication theory and signal processing. In subsequent chapters, elements of this background may be repeated and sometimes extended where necessary.

A typical Single Input Single Output (SISO) free-space optical communication system is illustrated in Fig. 2.1. An intensity modulated beam produced by a laser diode is expanded to a size so that beam divergence is minimised. After some distance, a large receive aperture collects as much light as possible and a telescope arrangement is used to reduce the size of the beam for detection by a photodiode. In essence, the intensity of the received signal with time, $y(t)$, in this setup can be expressed mathematically as

$$y(t) = \underbrace{x(t)}_{Signal} * [\underbrace{h_d(t)}_{Divergence} + \underbrace{h_a(t)}_{Attenuation} + \underbrace{h_t(t)}_{Fading}] + \underbrace{n(t)}_{Noise}, \tag{2.1}$$

where $x(t)$ is an arbitrary transmitted signal. The channel response (h_x) factors represent beam divergence, attenuation and fading, which will be described later. The noise term, $n(t)$, may be assumed to be Additive White Gaussian Noise (AWGN), but realistically is made up of noise from the transmit and receive electronics as well as noise from stray light interference. While this model appears simple, there are numerous trade-offs and issues associated with each term and indeed each component of the system - as expected in any complex system.

The beam produced by the laser diode can be structured optically to attain characteristics that suit the design of the FSO communication system. The physical properties of an optical beam have a significant impact on its propagation characteristics. As such, the various channel response factors in Eq. 2.1 strongly depend on this initial structuring, forming the basis of the contributions of this thesis. In Sec. 2.1, some introductory theory of optical modes and their propagation characteristics is provided.

When a laser beam propagates through the atmosphere, it is attenuated by absorption and scattering. The transmitted beam will also diverge, and since the receiver is of finite size, the detected intensity will be reduced if the size of the beam at the receiver is larger or not centred on the aperture. These attenuation effects are relatively constant and mainly depend on the initial alignment as well as the weather, which typically changes quite slowly, and can be largely mitigated by careful selection of wavelength and by increasing the transmit

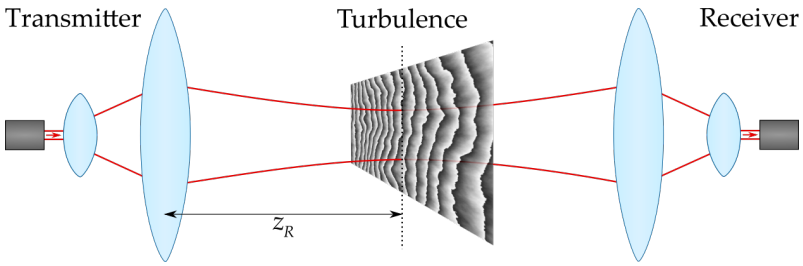


Figure 2.1: Simplified schematic of a typical FSO link. The Rayleigh range is labelled as z_R and a telescope arrangement is used at the transmitter and receiver. A turbulence phase screen, described in Sec. 2.3, is illustrated at the center of the link.

power (or intensity), within reason. Careful design of transmit and receive aperture sizes, as well as tracking systems to mitigate the effects of building sway, for example, are important engineering problems [48]. Atmospheric attenuation due to absorption and scattering is described in Sec. 2.2, after which these issues will not be discussed further as they are not the focus of this research.

A more severe source of attenuation in long distance links is atmospheric turbulence, described in Sec. 2.3. Random fluctuations in the atmosphere cause wandering and scintillation of the beam which manifests as signal fading at the receiver. Typical solutions to the turbulence issue are adaptive optics, which are often prohibitively expensive and complex signal processing.

Multiple Input Multiple Output (MIMO) based FSO systems that make use of Mode Division Multiplexing (MDM), which is a subset of Space Division Multiplexing (SDM), are largely similar to their SISO counterparts in terms of attenuation, but respond very differently to misalignment and turbulence. MDM uses orthogonal spatial modes of light to create multiple separate channels that propagate co-linearly, with Orbital Angular Momentum (OAM) modes often being the mode of choice due to their ease of use [8, 11]. In theory, there are an infinite number of orthogonal spatial modes, but in practise their use is not feasible.

Extremely high bandwidth systems have been successfully demonstrated. One of the first high capacity demonstrations was in 2011 over 1 m using four OAM modes and both polarisations at 1.4 Tbps [49], and soon after, by combining 24 OAM modes with Wavelength Division Multiplexing (WDM), just over 1 Pbps has been achieved [50]. To date, almost all high capacity demonstrations are over very short distances in lab environments.

The reason for this is that spatial modes are extremely susceptible to aberrations (from atmospheric turbulence, for instance), which degrade their orthogonality. The detection of optical modes is also difficult, and alignment is critical. Both of these effects lead to crosstalk between channels which must be mitigated using signal processing, if it cannot be done optically. Clearly if a set of orthogonal modes is more robust to these effects, they would be highly desirable.

2.1 Spatial Modes of Light

From Maxwell's equations, electromagnetic fields in free space, such as laser beams, can be described by the so-called Helmholtz equation, given by

$$[\nabla^2 + n^2 k^2]\mathbf{E} = 0, \tag{2.2}$$

for vector electric fields, $\mathbf{E}$. Here, $k = (2\pi)/\lambda$ is the wave number in vacuum and n is the refractive index of the medium in which the field propagates, where $n = 1$ in a vacuum. The

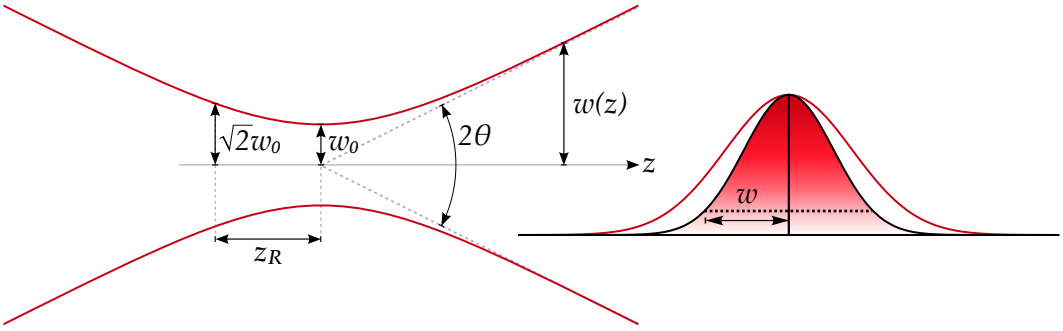


Figure 2.2: Left: The propagation of a Gaussian beam with the beam waist (with radius ω_0) in the centre. Right: An intensity profile of a Gaussian beam indicating the approximate position of the beam radius, w. The red line above the profile indicates the amplitude of the beam, $|U|$, and is the square root of the intensity.

wavelength is given by λ and for visible and infrared wavelengths (for example between 400 and 1600 nm) is on the order of hundreds of terahertz. In the case of scalar fields where the electric and magnetic components of the field have similar directions at all points in space (i.e. a uniform polarisation), we treat the electric field as a scalar field, U, and call this the scalar Helmholtz equation:

$$[\nabla^2 + n^2k^2]U(\mathbf{s}, z) = 0, \tag{2.3}$$

where $\mathbf{s}$ refers to the transverse coordinates which can be Cartesian where $\mathbf{s} \triangleq (x, y)$ or cylindrical where $\mathbf{s} \triangleq (r, \phi)$ and z refers to the propagation direction of the field. Here we have separated the temporal component from the field and ignored it as we are only interested in its spatial characteristics.

Solutions to the Helmholtz equation are often referred to as modes. There are many solutions to the equation, typically characterised by the choice of coordinate system and boundary conditions. In general, it is convenient to express solutions after making the so-called paraxial approximation, where the scalar field vector is written in the form in Eq. 2.4. The paraxial approximation assumes that the fields propagation is predominantly in the z direction, and thus reduces the second order Helmholtz equation into a first order partial differential equation.

$$U(\mathbf{s}, z) = a(\mathbf{s}, z)e^{-jkz}, \tag{2.4}$$

where $a(\mathbf{s}, z)$ is the complex amplitude that describes the mode and e^{-jkz} represents a plane wave travelling in the positive z direction. Gaussian beams are widely used in free space optical communications since they are readily produced by laser diodes and are discussed in Sec. 2.1.1. Higher order beams are described in Sec. 2.1.2 since they have interesting properties and are the primary subject of this research.

2.1.1 Gaussian Beams

One solution of the paraxial wave equation leads to what is called a Gaussian beam, which has a Gaussian intensity profile and a uniform phase on the transverse (xy) plane at $z = 0$. Figure 2.2 diagrammatically shows many of the variables in this section. The field that describes a Gaussian beam is

$$U(r, z) = \frac{1}{z + jz_R} \exp\left[\frac{-r^2}{w^2(z)}\right] \exp\left[\frac{-j\pi r^2}{\lambda R(z)}\right] \tag{2.5}$$

where z is the distance to the beams focus or "waist" and r is the radial position. There is no azimuthal (ϕ) dependence as a Gaussian beam is radially symmetric. The radius of

the beam is w, which is the point at which the field amplitude drops to $1/e$ (or intensity $1/e^2 \approx 13.5\%$) of the axial value, and as a function of z is

$$w(z) = w_0 \sqrt{1 + \frac{z^2}{z_R^2}}. \tag{2.6}$$

The Rayleigh range is z_R, given by Eq. 2.7, which is a parameter that defines the the form of the Gaussian beam:

$$z_R = \frac{\pi w_0^2}{M^2 \lambda}, \tag{2.7}$$

where the beam propagation factor $M^2 = 1$ for a perfect Gaussian beam. If $z \ll z_R$ then the beam is collimated, which implies a flat wavefront and the beam radius is approximately constant. If $z \gg z_R$ then the beam is diverging, which implies a spherical wavefront with a radius of curvature $R(z) \approx z$. The radius of curvature of the wavefront as a function of z is more precisely defined as

$$R(z) = z \left(1 + \frac{z_R^2}{z^2}\right). \tag{2.8}$$

In long distance FSO, it is unlikely that it is possible to operate close to the Rayleigh range (i.e. when $z \gg z_r$), and so the radius of the beam can be approximated as a cone with half-angle, θ, in radians as

$$\theta \approx \frac{M^2 \lambda}{\pi w_0}, \tag{2.9}$$

which results in the beam radius

$$w(z) = z \tan\left(\frac{M^2 \lambda}{\pi w_0}\right). \tag{2.10}$$

A pertinent question for any optical system with apertures is how much power is collected by a certain aperture. In reality, since we use $1/e^2$ for the definition of the beam waist, an aperture must usually be slightly bigger than the waist at the aperture. As a rule of thumb, for 99% collection efficiency, the aperture radius, $r = 1.52 w(z)$. Factors for 95% and 90% are 1.22 and 1.07 respectively. The general calculation for the fractional power is given by

$$\frac{P(r,z)}{P_0} = 1 - e^{-2r^2/w^2(z)} \tag{2.11}$$

Most of the equations given in this section can be used as approximations for higher order beams as well - the M^2 factor should be adjusted accordingly. The obvious exception is the power through an aperture. Beams such as Laguerre-Gauss (LG) beams have a ring-like intensity structure and so Eq. 2.11 would be a poor estimate, for example.

2.1.2 Higher Order Beams

The higher order solution to the paraxial wave equation in cylindrical coordinates is called a LG mode and in Cartesian coordinates is called a Hermite-Gauss (HG) mode, with examples of the mode intensity and phase in Fig. 2.3 [51, 52]. The modes within each of these sets are orthogonal to each other, making them useful for multiplexing. When the beams are generated using a hologram or Spatial Light Modulator (SLM) we encode the modes at $z = 0$, resulting in Eqs. 2.12 and 2.13 respectively [53, 54].

$$U_{\ell,p}^{\mathrm{LG}}(r,\phi) = C_{\ell,p}^{\mathrm{LG}} \left(\frac{r\sqrt{2}}{w_0}\right)^{|\ell|} L_p^{|\ell|}\left(\frac{2r^2}{w_0^2}\right) \exp\left(-\frac{r^2}{w_0^2}\right) \exp(-i\ell\phi) \tag{2.12}$$

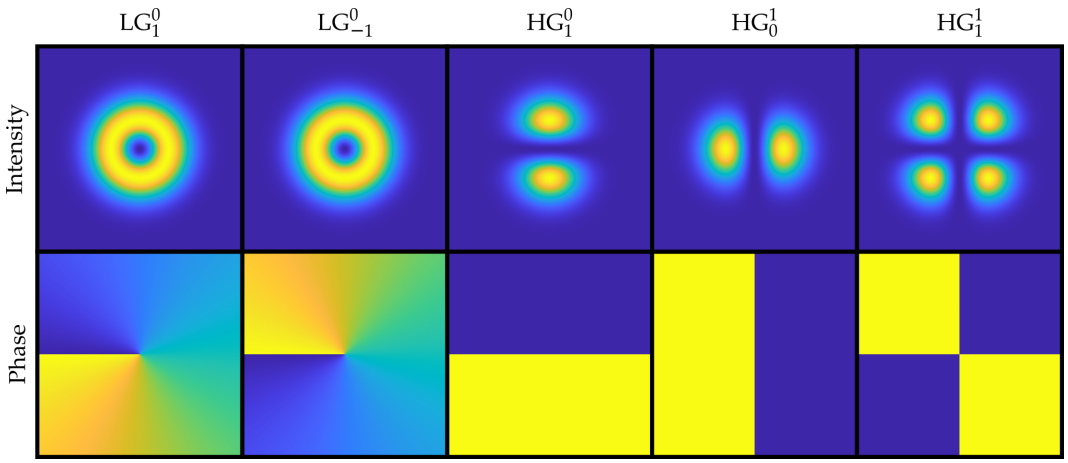


Figure 2.3: Examples of LG and HG modes showing intensity (amplitude squared) and phase. The phase colourmap of the LG modes represents a 0 to 2π phase change (blue to yellow) and a 0 and π for the HG modes (blue and yellow). The intensity colourmap is 0 to 1 (blue to yellow).

where ℓ and p are the mode indices, $C_{\ell p}^{LG}$ is a normalisation constant and $L_p^{|\ell|}(\cdot)$ is the generalised Laguerre polynomial and

$$U_{n,m}^{\mathrm{HG}}(x,y) = C_{n,m}^{\mathrm{HG}} H_n\left(\frac{\sqrt{2}\,x}{w_0}\right) H_m\left(\frac{\sqrt{2}\,y}{w_0}\right) \exp\left(-\frac{x^2+y^2}{w_0^2}\right) \tag{2.13}$$

where n and m are the mode indices, C_{nm}^{HG} is a normalisation constant and $H_n(\cdot)$ and $H_m(\cdot)$ are Hermite polynomials of order n and m respectively. The normalisation constants for LG and HG modes are given by Eqs. 2.14 and 2.15, respectively.

$$C_{\ell,p}^{LG} = \sqrt{\frac{2p!}{\pi(p+|\ell|)!}} \tag{2.14}$$

$$C_{n,m}^{HG} = \frac{1}{\omega_0}\sqrt{\frac{2^{(1-n-m)}}{\pi n!m!}} \tag{2.15}$$

There are numerous other higher order modes but they are not considered in this research. Two common examples are Ince-Gauss modes (elliptical coordinates) and Bessel-Gauss modes (cylindrical coordinates). The so-called OAM modes are in fact a subset of LG modes with $p = 0$ [55].

The propagation of LG and HG modes is similar to Gaussian modes except that the beam propagation factor, M^2, is different and depends on the order of the mode. Higher order modes expand faster with propagation distance than those with lower orders, and so the size of the transmit and receive apertures of a system must be carefully considered. The M^2 values of HG and LG beams are simply $M^2 = n + m + 1 = 2p + |\ell| + 1$ respectively. The beam waist can be calculated using Eqs. 2.6 and 2.7, but only in the case that the beam radius is defined using the second moment of the intensity, which is called the D4σ method, which results in $1/e^2$ for a Gaussian beam. Clearly, the M^2 factor has a direct influence on how rapidly a beam diverges and so for higher-order modes where $M^2 > 1$, this must be considered.

It has been shown that the number of modes that is supported by a link is given by the product of the Fresnel number of the transmitter and receiver [56, 57]. For identical

apertures separated by L with diameter D on both sides of a link, the highest order modes are governed by the limit

$$M^2 \leq \frac{\pi D^2}{4\lambda L}. \tag{2.16}$$

2.1.3 Detection of Higher Order Modes

Gaussian beams in an FSO system can be detecting simply by using a photodiode. Their intensity profile is such that, when focused, it forms a point of light which fills a photodiode well. An LG beam on the other hand has a ring shape even when focused, so it is likely that the photodiode will be in the dark region at the centre of the ring. In an MDM system, multiple modes are used which must be separated and directed to individual photodiodes. The technique to do this is called Modal Decomposition (MD). There are numerous approaches to MD and it is the subject of much research and development [58–65], but a first-principles approach using holograms will be explained in this section as it is the approach that is used for the work presented in later chapters [66, 67].

Any unknown field, $U(\mathbf{s})$, can be written in terms of an ortho-normal basis set, $\Psi_n(\mathbf{s})$,

$$U(\mathbf{s}) = \sum_{n=1}^{\infty} c_n \Psi_n(\mathbf{s}) = \sum_{n=1}^{\infty} |c_n| e^{i\phi_n} \Psi_n(\mathbf{s}), \tag{2.17}$$

with complex weights $c_n = |c_n| e^{i\phi_n}$ where $|c_n|^2$ is the power in mode $\Psi_n(\mathbf{s})$ and ϕ_n is the inter-modal phase, satisfying $\sum_{n=1}^{\infty} |c_n|^2 = 1$. In typical communication systems, the inter-modal phase is not required, simplifying the MD requirements. Equation 2.17 can ideally be thought of as the sum of several multiplexed modes, each of which is a separate communication channel.

The unknown modal coefficients, c_n, which carry the modulated information, can be found by the inner product

$$c_n = \langle \Psi_n | U \rangle = \int \Psi_n^*(\mathbf{s}) U(\mathbf{s}) d\mathbf{s}, \tag{2.18}$$

where we have exploited the ortho-normality of the basis, namely

$$\langle \Psi_n | \Psi_m \rangle = \int \Psi_n^*(\mathbf{s}) \Psi_m(\mathbf{s}) d\mathbf{s} = \delta_{nm}. \tag{2.19}$$

Note that Dirac notation, borrowed from quantum optics, has been used for the inner products. The calculation of Eq. 2.19 may be achieved experimentally using a lens to execute an optical Fourier transform, $\mathcal{F}$. Accordingly we apply the convolution theorem (using $\mathbf{k}$ as an auxiliary variable)

$$\mathcal{F}\{f(\mathbf{s})g(\mathbf{s})\} = F(\mathbf{k}) * G(\mathbf{k}) = \int F(\mathbf{k}) G(\mathbf{s} - \mathbf{k}) d\mathbf{k} \tag{2.20}$$

to the product of the incoming field modulated with a transmission function (for example a hologram), $T_n(\mathbf{s})$, that is the conjugate of the basis function, namely,

$$W_0(\mathbf{s}) = T_n(\mathbf{s}) U(\mathbf{s}) = \Psi_n^*(\mathbf{s}) U(\mathbf{s}), \tag{2.21}$$

to find the new field at the focal plane of the lens as

$$W_f(\mathbf{s}) = A_0 \, \mathcal{F}\{W_0(\mathbf{s})\} = A_0 \int \Psi_n^*(\mathbf{k}) U(\mathbf{s} - \mathbf{k}) d\mathbf{k} \tag{2.22}$$

Here $A_0 = \exp(i4\pi f/\lambda)/(i\lambda f)$ where f is the focal length of the lens and λ the wavelength of the light. If we set $\mathbf{s} = \mathbf{0}$, which experimentally is the on-axis intensity in the Fourier plane, then Eq. (2.22) becomes

$$W_f(\mathbf{0}) = A_0 \int \Psi_n^*(\mathbf{k}) U(\mathbf{k}) d\mathbf{k} \tag{2.23}$$

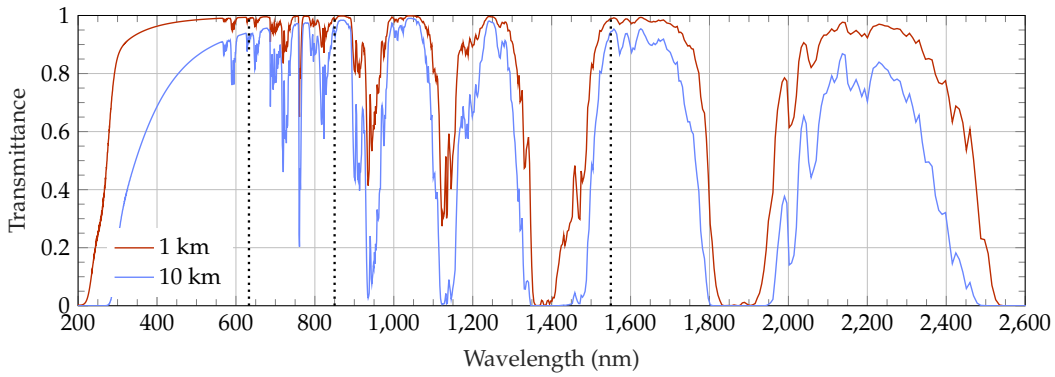


Figure 2.4: Example atmospheric transmittance of different wavelengths due to molecular absorption in the atmosphere according to the LOWTRAN7 model [69].

which is the desired inner product of Eq. (2.18). Therefore we can find our modal weightings from an intensity measurement of the on axis light

$$|W_f(\mathbf{0})|^2 = |A_0|^2 |\langle \Psi_n | U \rangle|^2 = |c_n|^2. \tag{2.24}$$

Practically, the transmission functions are encoded onto Spatial Light Modulators (SLMs) which can be thought of as digital holograms. Usually there is more than one mode of interest in a system. In order to detect all of the modes, several holograms can be cycled on the SLM in a time division multiplexed manner, or alternatively they can all be added together with different grating functions so that the "spots" that represent each mode can be spatially separated. A photodiode can then be placed at the appropriate location at the focal length of the MD lens.

There exists a significant challenge in the placement of these photodiodes. The on-axis intensity must be measured precisely, and not any of the surrounding light, otherwise crosstalk will manifest. A simple approach is to ensure that the size of the photodiodes is sufficiently small. Alternatively, the spots can be carefully aligned with the tips of Single Mode Fibres (SMFs) [68].

2.2 Atmospheric Attenuation

Beam divergence is a critical factor in FSO communication where the Signal to Noise Ratio (SNR) is important for high capacity. Only a limited amount of light can be collected by the receive aperture, and so only a fraction of the transmitted light can be detected if the beam has expanded beyond the size of the aperture. This is a significant but almost unavoidable issue for long range links, for example Earth to Satellite or even terrestrial links over multiple kilometre distances. The only way to avoid this problem is to use lower order modes and to carefully design the optics of the system to capture as much light as possible.

As we are interested in atmospheric FSO, there is the additional issue of attenuation due to absorption and scattering as well as atmospheric turbulence which is described in detail in Sec. 2.3 as it is the focus of this research.

Figure 2.4 shows the typical atmospheric absorption of various wavelengths due to the different molecules present in the atmosphere. The precise amount of attenuation depends on the concentrations of these molecules, notably water vapour in the visible and Near Infrared (NIR) bands, which varies depending on the weather, for instance. In addition to absorption by molecules, there is scattering which is caused by small particles such as dust, pollution and water droplets (rain, fog, snow, etc.). There is also an element of scattering by molecules and absorption by particles. The Beer-Lambert law enables us to calculate the

overall atmospheric transmission loss taking all of these effects into account [48, 70]. This loss per unit length is called "specific attenuation" as is given by

$$\beta(\lambda) = \frac{10}{L}\log\left(\frac{P_0}{P_R}\right) = \frac{10}{L}\log\left(e^{\gamma(\lambda)L}\right) \quad [\text{dB/km}], \tag{2.25}$$

where

$$\gamma(\lambda) = \alpha_m(\lambda) + \alpha_a(\lambda) + \beta_m(\lambda) + \beta_a(\lambda), \tag{2.26}$$

which is called the atmospheric attenuation coefficient, L is the link length, P_0 is the transmit power and P_R is the received power. The first two terms in Eq. 2.26 represent the molecular and aerosol (particles) absorption coefficients, and the second two terms represent the respective scattering coefficients.

There are numerous models that describe these coefficients [70]. For common telecommunication wavelengths such as 850 nm and 1550 nm, where opto-electronic devices are readily available, the specific attenuation per kilometre is 0.41 dB and 0.01 dB respectively [70]. However, scattering clearly depends on the visibility (clarity) of the atmosphere and so rules of thumb should not be relied on. From Fig. 2.4, which is for LOWTRAN absorption/transmittance only, the transmittance of a mid-latitude summer, 1 km path at 850 nm is 0.988 and at 1550 nm is 0.999. If scattering is included using MODTRAN (30°C, 16 km visibility, which is good), the transmittance is 0.880 and 0.942 respectively - a significant difference. Over 10 km using MODTRAN, the transmittance's for 850 nm and 1550 nm are 0.764 and 0.895 respectively [69, 71].

Clearly, the choice of wavelength is a critical factor for a FSO communication system. This is largely an engineering problem and is therefore not discussed in detail in this work. While it may be tempting to increase the transmit power and use a wavelength that is not significantly attenuated by the atmosphere, energy consumption and eye safety must be taken into account.

2.3 Atmospheric Turbulence

When a laser beam propagates through the atmosphere it encounters spatially and temporally varying refractive indices, mainly due to random temperature variations and convective processes. This randomly aberrates the beam wavefront. The Kolmogorov model for turbulent flow is the basis for many contemporary theories of turbulence and is able to relate these temperature fluctuations to refractive index fluctuations [72]. The average size of the turbulent cells are specified by a so-called inner scale, l_0, which is typically on the order of millimetres and an outer scale, L_0, which is on the order of meters [73]. Kolmogorov turbulence assumes $l_0 = 0$ and $L_0 = \infty$ which simplifies the model significantly.

Models of turbulence typically only provide statistical averages for the random variations of the atmosphere, but in most cases this is sufficient. The power spectral density of the refractive index fluctuations given by the Kolmogorov model is described by

$$\Phi_n^K(\kappa) = 0.033 C_n^2 \kappa^{-11/3} \quad \text{for} \quad 1/L_0 \ll \kappa \ll 1/l_0, \tag{2.27}$$

where $\kappa = 2\pi(f_x \cdot \hat{x} + f_y \cdot \hat{y})$ is the angular spatial frequency vector and C_n^2 is the refractive index structure parameter, which is essentially a measure of the strength of the refractive index fluctuations. Values of C_n^2 vary from 10^{-17} $\text{m}^{-2/3}$ in "weak" turbulence and up to about 10^{-13} $\text{m}^{-2/3}$ in "strong" turbulence [73]. It is natural to assume that long distance propagation in weak turbulence may be "just as bad" as short propagation in strong turbulence. This assumption is indeed true and so the strength of turbulence is in fact denoted by a different parameter, the Rytov variance, which is given by

$$\sigma_R^2 = 1.23 C_n^2 k^{7/6} L^{11/6} \tag{2.28}$$

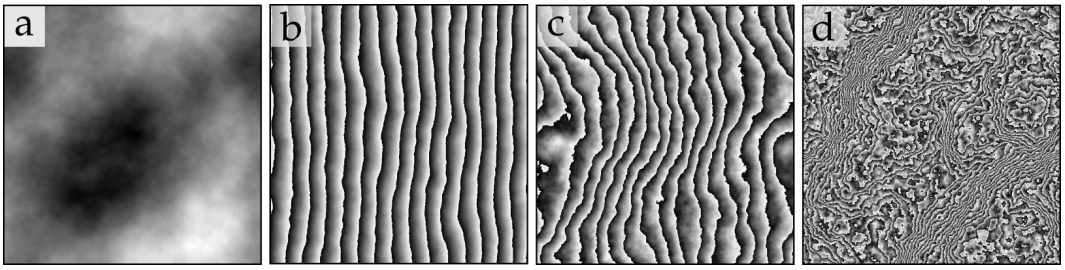


Figure 2.5: Example Kolmogorov turbulence screens with varying strength. A raw turbulence screen is shown in (a), however, when the screen is used on a digital hologram a grating is applied. Frames (b) to (d) show turbulence screens from weak to strong with gratings applied.

for plane wave propagation in Kolmogorov turbulence. As usual, k is the wave number given in Sec. 2.1 and L is the propagation distance in meters. Typically, weak fluctuations in turbulence are when $\sigma_R^2 \ll 1$, moderate fluctuations when $\sigma_R^2 \approx 1$ and strong fluctuations when $\sigma_R^2 \gg 1$.

There are several more accurate turbulence power spectrum models with increasing complexity, for example the Hill power spectrum (which has no analytical solution), the Tatarskii power spectrum and the von Kármán power spectrum, which is [73]

$$\Phi_n^{vK}(\kappa, l_0, L_0) = 0.033 C_n^2 \frac{\exp\left(-\kappa^2/k_m^2\right)}{(\kappa^2 + k_0^2)^{11/6}} \quad \text{for} \quad 0 \leq \kappa < \infty, \tag{2.29}$$

where $k_m = 5.92/l_0$ and $k_0 = 2\pi/L_0$. The current most accurate power spectrum is called the Modified Atmospheric Spectrum, and builds from the von Kármán and Hill spectrums:

$$\Phi_n^{M}(\kappa, l_0, L_0) = 0.033 C_n^2 \left[1 + 1.802\left(\frac{\kappa}{k_l}\right) - 0.254\left(\frac{\kappa}{k_l}\right)^{7/6}\right] \frac{\exp\left(-\kappa^2/k_l^2\right)}{(\kappa^2 + k_0^2)^{11/6}} \quad \text{for} \quad 0 \leq \kappa < \infty, \tag{2.30}$$

where $k_l = 3.3/l_0$. We can use these power spectrums to generate individual snapshots of turbulence in the form of phase screens with appropriate statistics, with examples shown in Fig. 2.5 [74]. These phase screens can be encoded as holograms for use experimentally. Several well-known methods exist to generate these phase screens and so it will not be discussed here [75].

The Fried parameter, r_0, commonly known as the atmospheric coherence length, is a useful alternative to C_n^2 as is given by Eq. 2.31 for a plane wave in Kolmogorov turbulence [76]:

$$r_0 = 1.68\left(C_n^2 L k^2\right)^{-3/5} \tag{2.31}$$

and more generally for a plane wave in unspecified turbulence,

$$r_0 = \left(0.423 k^2 \int_0^L C_n^2(z) dz\right)^{-3/5}. \tag{2.32}$$

The atmospheric coherence length is a radius after which the atmospheric turbulence becomes uncorrelated. In other words, in an FSO system, two beams separated by at least r_0 meters will experience uncorrelated fading - an excellent opportunity for channel diversity.

Finally, a common but less descriptive parameter to specify turbulence strength is the Strehl Ratio (SR), which is the ratio of the average on-axis beam intensity with, $\langle I(\mathbf{0})\rangle$, and without, $I_0(\mathbf{0})$, turbulence and is given by Eq. 2.33 generally and for a plane wave in

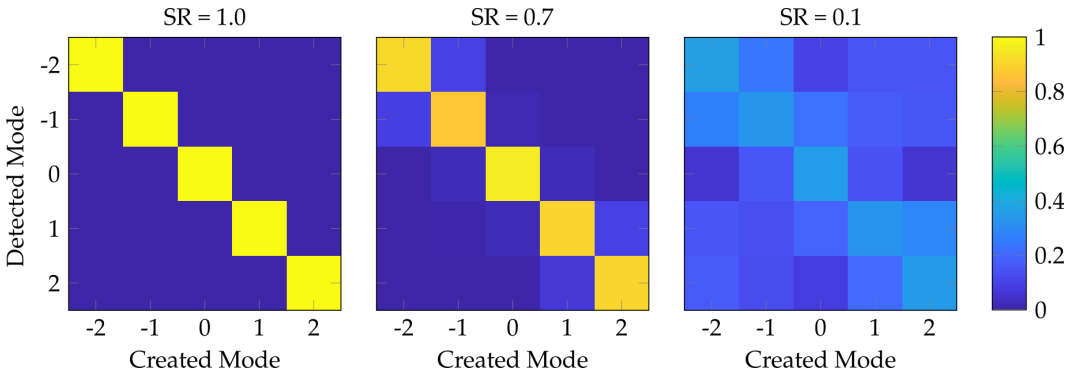


Figure 2.6: Example OAM crosstalk for no turbulence (SR = 1.0), weak turbulence (SR = 0.7) and strong turbulence (SR = 0.1) showing increasing crosstalk with turbulence strength. The crosstalk normalisation for the higher order modes (for example $\ell = \pm 2$) is inaccurate.

Kolmogorov turbulence.

$$\mathrm{SR} = \frac{\langle I(\mathbf{0}) \rangle}{I_0(\mathbf{0})} \approx \frac{1}{[1 + (D/r_0)^{5/3}]^{6/5}}, \tag{2.33}$$

where D is the aperture diameter. In summary, turbulence leads to scintillation, beam wandering and other effects, and is the reason why the on-axis beam intensity, $I(\mathbf{0})$, is reduced on average. The scintillation index, σ_I^2, is another common parameter similar to the SR, but is useful where knowledge of the intensity in the absence of turbulence is unknown.

$$\sigma_I^2 = \frac{\langle I^2(\mathbf{0}) \rangle - \langle I(\mathbf{0}) \rangle^2}{\langle I(\mathbf{0}) \rangle^2} = \frac{\langle I^2(\mathbf{0}) \rangle}{\langle I(\mathbf{0}) \rangle^2} - 1 \tag{2.34}$$

Similarly to the Rytov index, the scintillation index may be used to roughly characterise turbulence strength. Weak turbulence is when $\sigma_I^2 < 0.3$, medium is when $\sigma_I^2 \approx 1$ and strong is defined as $\sigma_I^2 \gg 1$. For weak fluctuations where $\sigma_R^2 \ll 1$, $\sigma_R^2 = \sigma_I^2$.

In an MDM system, the effect of turbulence not only causes attenuation of individual modes, an extension of the SR called Mode Dependent Loss (MDL), but also crosstalk between modes due to aberration of the wavefronts. An example measurement of this for OAM modes $\ell = -2$ to 2 is shown in Fig. 2.6. The precise mechanism and modelling of how turbulence induces crosstalk is very complex and not well studied but will be discussed further in Sec. 2.3.2.

For the intensity reduction of the individual modes, MDL, we use the intensity of individual modes, S_i, instead of the overall intensity of the beam, I,

$$\mathrm{MDL}_i = 1 - \frac{S_i}{S_{i,0}}, \tag{2.35}$$

where $S_{i,0}$ is the intensity of mode i in the absence of turbulence. Typically, the energy in the individual modes is spread to neighbouring modes [9]. This mode crosstalk with respect to mode i is defined as the fraction of the total intensity not in mode i:

$$C_i = 1 - \frac{S_i}{\sum_j S_j}, \tag{2.36}$$

where $\sum_j S_j$ is the sum of the intensities in all the modes, including mode i.

2.3.1 Temporal Effects

Since air is constantly mixing, turbulence effects change with time. It is possible to calculate a workable bandwidth for the changing turbulence. Using Taylor's "frozen turbulence" hypothesis, we can assume that the state of atmospheric turbulence is frozen for a period of time which changes at the Greenwood frequency and is typically on the order of Hz to several kHz [77]. Under this assumption, we imagine that the turbulence cells are stationary and are driven by the wind at a certain velocity. Accordingly, faster wind speed results in a higher Greenwood frequency.

The tilt Greenwood frequency, f_T, describes beam wander, which results from tip and tilt aberrations due to turbulence.

$$f_T = 0.33 D^{-1/6} \lambda^{-1} \sec^{1/2}(\beta) \left[\int_0^L C_n^2(z) V_{\text{Wind}}^2(z) dz \right]^2, \tag{2.37}$$

where β is the azimuthal angle of the beam propagation, 0° being horizontal, and $V_{\text{Wind}}(z)$ is the wind speed as a function of propagation distance in meters per second. The higher order aberrations of the beam are included in the Greenwood frequency, f_G,

$$f_G = 2.31 \lambda^{-6/5} \left[\sec(\beta) \int_0^L C_n^2(z) V_{\text{Wind}}^{5/3}(z) dz \right]^{3/5}. \tag{2.38}$$

The expression for the Greenwood frequency can be dramatically simplified if we assume a constant wind speed,

$$f_G = 0.43 (V_{\text{Wind}} / r_0). \tag{2.39}$$

2.3.2 Turbulence Induced Fading Models

Much the same as in radio, the statistics of a signal (a modulated laser beam) propagating though the atmospheric channel can be modelled stochastically with varying degrees of accuracy and complexity. There are several models that describe the random fluctuations of the received intensity, known as fading, of plane and spherical waves in atmospheric turbulence [73].

The most widely used model for fading is the log-normal model which was derived based on the first-order Rytov approximation with Probability Distribution Function (PDF) given by [78, 79],

$$p_I(i) = \frac{1}{i\sqrt{2\pi\sigma_I^2}} \exp\left(-\frac{[\ln(i) + \sigma_I^2/2]^2}{2\sigma_I^2} \right) \quad \text{where} \quad i > 0 \tag{2.40}$$

The log-normal model is inaccurate over long distances and is inappropriate for moderate to strong turbulence. In strong turbulence conditions a negative exponential distribution may be used [80],

$$p_I(i) = \frac{1}{\langle I \rangle} \exp\left(-\frac{i}{\langle I \rangle} \right) \quad \text{where} \quad i > 0 \tag{2.41}$$

where $\langle I \rangle$ is the expected (or mean) received intensity. Naturally, there have been efforts to determine a good model that is suitable under a wide range of turbulence conditions. The Double Generalised Gamma-Gamma distribution is currently the most accurate fading model available and relies on the doubly stochastic nature of turbulence on both large and small scales [81].

There are also some models for higher order modes, but analytical solutions of these modes are extremely difficult and thus empirical measurements are relied upon [9, 82]. Higher order modes have a wavefront that is not well approximated by a plane wave and as a result the effect of turbulence on these modes is not well understood. Experimental

results have shown that a Johnson-SB distribution is a good fit for OAM modes [82]. There has been no work identifying how the parameters of the Johnson-SB distribution map to standard variables such as C_n^2 or r_0, for example. There has been no work determining fading distributions for other higher-order mode sets such as the HG or general LG modes.

2.3.3 Turbulence Induced Modal Crosstalk Models

Crosstalk is an important statistic for MDM FSO channels and so it has been studied in some detail both empirically and analytically for OAM modes [9, 82–84]. The ensemble average, $\langle P_j \rangle$ of the normalised power in an OAM mode specified by ℓ_j when mode ℓ_i is transmitted is given by

$$\langle P_j \rangle = \begin{cases} 1 - 1.01\left(\frac{D}{r_0}\right)^{5/3} & \text{for } \Delta = 0 \\ 0.142\frac{\Gamma(\Delta - 5/6)}{\Gamma(\Delta + 11/6)}\left(\frac{D}{r_0}\right)^{5/3} & \text{otherwise} \end{cases} \tag{2.42}$$

where $\Delta = |i - j|$ and $\Gamma(\cdot)$ is the gamma function. Equation 2.42 has been verified but recently was shown to be inaccurate over long distances (1.7 km), probably due to beam wander [20]. Similar expressions for LG radial modes as well as HG modes do not currently exist.

CHAPTER 3

The Resilience of Hermite- and Laguerre-Gauss Modes in Turbulence

This chapter is based on the following publication:

M. A. Cox, L. Maqondo, R. Kara, G. Milione, L. Cheng and A. Forbes, "The Resilience of Hermite- and Laguerre-Gaussian Modes in Turbulence," *Journal of Lightwave Technology*, vol. 37, no. 16, pp. 3911–3917, Aug. 2019.

The author conceptualised the work, assisted with experimental measurements, analysed the data and wrote the majority of the paper.

ONE of the primary issues with Free Space Optical (FSO) communication is turbulence, which results in what is typically called optical scintillation and manifests as the random fluctuations (or fading) of the received signal's intensity. For Mode Division Multiplexing (MDM), turbulence also distorts the wavefront resulting in crosstalk, thus reducing the link capacity. It is difficult to mitigate the effects of turbulence and common strategies are to use techniques such as Multiple Input Multiple Output (MIMO) signal processing, strong forward error correction as well as adaptive optics [11]. Channel diversity is another usable technique, detailed further in Chap. 5.

The question of whether there are optical modes that are more resilient to atmospheric turbulence than a standard Gaussian mode is pertinent as this would be an effective way to passively increase the range of a FSO link. Typical beams that have been well investigated in turbulence are Orbital Angular Momentum (OAM) or Laguerre-Gauss (LG) modes, Bessel-Gauss modes and also vector modes with spatially varying polarisation, with varying degrees of success [37–41]. Specifically, the use of vector vortex modes is investigated in Chap. 4. In general it has been found that higher order modes are indeed more resilient than Gaussian modes [38]. In the presence of a restricted aperture, LG (or rather OAM) modes have a larger information capacity than Hermite-Gauss (HG) modes [42], but if this is not the case then HG modes are a promising candidate as they are robust against lateral displacements (or beam wander) [43–45].

Given this observation, assuming no aperture restrictions, are HG modes (or a subset of HG modes) more resilient than LG modes in atmospheric turbulence and what gains in terms of propagation distance can be expected? We hypothesise that since the dominant effect of turbulence is tip/tilt [85], HG modes will indeed be more resilient than LG modes,

however, it is unknown whether the higher order effects of turbulence will counteract this gain.

In Sec. 3.1 we provide a summarised background of HG and LG modes, as well as a convenient, phase-only approximation of an HG mode which we call a Binary Hermite-Gauss (BHG) mode. Orthogonality is critical to MDM and so we briefly discuss and show how the BHG modes are not always orthogonal, as one might naively assume. Furthermore, we provide a short overview of atmospheric turbulence and how it affects the orthogonality of these mode sets. Due to their different phase structure, it is logical to assume that different modes will be affected by atmospheric turbulence in different ways. It would be highly advantageous to an MDM system if a certain set of modes exhibited lower losses or less crosstalk. An experimental setup and methodology to determine whether (B)HG modes are "better" than LG modes in these respects is described in Sec. 3.2 with results and discussion in Sec. 3.3. The chapter is concluded in Sec. 3.4.

3.1 Preliminaries

For the reader's convenience, we provide a brief background of HG, Binary HG and LG modes, their orthogonality and how the impact of atmospheric turbulence on the modes is typically measured.

3.1.1 Laguerre- and Hermite-Gaussian Modes

The higher order solution to the paraxial wave equation in cylindrical coordinates is called a LG mode and in Cartesian coordinates is called an HG mode, with examples of the mode intensity and phase in Fig. 3.1. The modes within each of these sets are orthogonal to each other, making them useful for multiplexing. When the beams are generated with a Spatial Light Modulator (SLM) we encode the modes at $z = 0$, resulting in Eqs. 3.1 and 3.2 respectively.

$$U^{\mathrm{LG}}_{\ell,p}(r,\phi) = C^{\mathrm{LG}}_{\ell,p}\left(\frac{r\sqrt{2}}{w_0}\right)^{|\ell|} L_p^{|\ell|}\left(\frac{2r^2}{w_0^2}\right)\exp\left(-\frac{r^2}{w_0^2}\right)\exp(-i\ell\phi) \tag{3.1}$$

where ℓ and p are the mode indices, $C^{LG}_{\ell p}$ is a normalisation constant and $L_p^{|\ell|}(\cdot)$ is the generalised Laguerre polynomial and

$$U^{\mathrm{HG}}_{n,m}(x,y) = C^{\mathrm{HG}}_{n,m}\, H_n\left(\frac{\sqrt{2}\,x}{w_0}\right) H_m\left(\frac{\sqrt{2}\,y}{w_0}\right)\exp\left(-\frac{x^2+y^2}{w_0^2}\right) \tag{3.2}$$

where n and m are the mode indices, C^{HG}_{nm} is a normalisation constant and $H_n(\cdot)$ and $H_m(\cdot)$ are Hermite polynomials of order n and m respectively.

We can encode HG modes without amplitude (i.e. only phase) information, resulting in what we call a Binary HG (BHG) mode. A BHG mode has only two phase values (similar to an HG mode) of 0 and π with the amplitudes constrained to be either 0 or 1. This is achieved simply using Eq. 3.3:

$$U^{\mathrm{BHG}}_{n,m}(x,y) = \frac{1}{2} + \frac{1}{2}\mathrm{sign}\left[U^{\mathrm{HG}}_{n,m}(x,y)\right] \tag{3.3}$$

We consider BHG modes in addition to standard HG modes because they can easily be created and decomposed with a refractive element. Unfortunately, while LG and HG modes form an orthonormal basis, the BHG modes are not always orthogonal:

$$\langle U^{\mathrm{BHG}}_{n,m}\rangle\, U^{\mathrm{BHG}}_{n',m'} = \begin{cases} 0 & m \neq m' \text{ and } m \text{ is even} \\ 0 & n \neq n' \text{ and } n \text{ is even} \\ c & \text{elsewhere,} \end{cases} \tag{3.4}$$

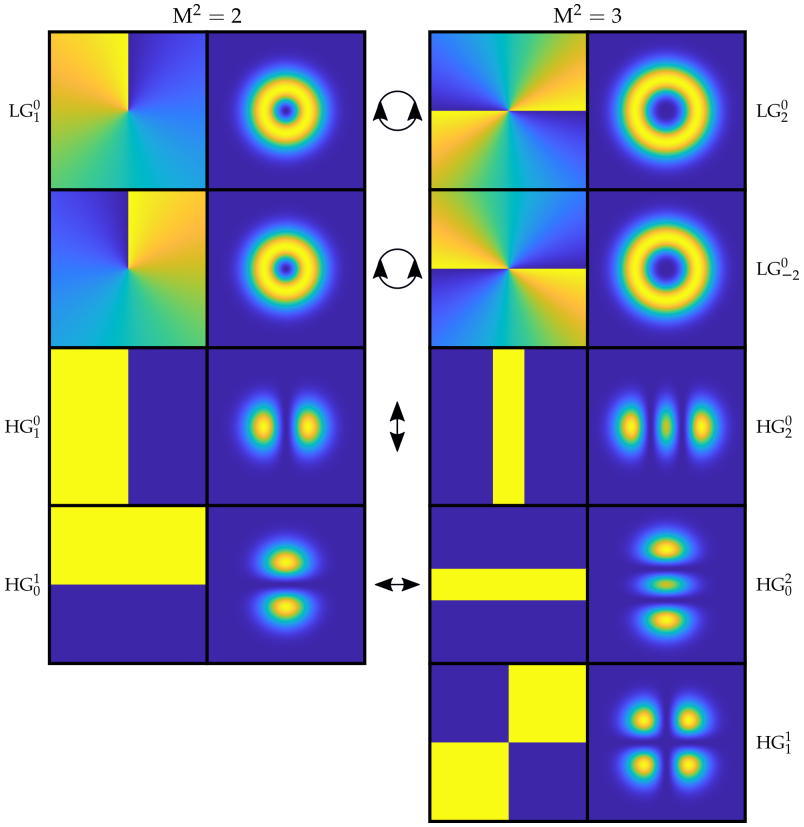


Figure 3.1: Modes used in the experiment, with wavefront to the left and intensity to the right of each, corresponding to Tab. 3.1. The arrows in the centre indicate the translational (or rotational) axis where the mode is robust and will still be detected correctly. The HG_1^1 mode does not have a robust axis.

where c is some normalisation constant. The HG modes are also not always orthogonal to BHG modes, as an example, the orthogonality result is an asymmetric matrix when you keep one index equal to zero, $m = 0$ or $n = 0$.

Since the detection system for higher order modes often makes use of a hologram which works as a matched filter or inner product measurement, the alignment of the incoming beam onto the hologram is critical. Adaptive optics are effective at reducing Mode Dependent Loss (MDL), which is the intensity reduction, or fading, of individual modes making up the beam and mode-crosstalk [86]. This is because adaptive optics, and indeed even a simple tip/tilt mirror, are able to correct any misalignments in addition to wavefront corrections.

Figure 3.1 shows the phase and intensity of several different LG and HG modes. For an LG mode to be correctly detected it must be aligned so that the vortex of the mode is centred on the corresponding phase singularity encoded on the hologram. Any translation (called tip or tilt) from this overlap will manifest as crosstalk into neighbouring modes, however, because the beam is radially symmetric, rotation of the beam will not affect the detection. HG modes are symmetric with respect to a horizontal and/or vertical axis. Unlike LG modes, rotation of an HG mode will adversely affect the integrity of the measurement, however, it is clear from the figure that HG modes which are symmetric about only one axis will be resilient to translation along that axis. For instance, the HG_0^1 mode can move left or right without any detection error whereas the HG_1^1 mode must be well aligned similar to the LG modes.

The completeness property of the LG and HG bases allow us to express any element of

one basis as a linear combination of elements from the other basis using the transformation relations in Eqs. 3.5 and 3.6 [87]. Note that here the LG modes have been written in terms of n and m, which are indices typically used for HG modes. The usual indices can be recovered as $\ell = n - m$ and $p = \min(n, m)$.

$$U^{\mathrm{LG}}_{n,m}(x, y, z) = \sum_{k=0}^{N} i^k b(n, m, k) U^{\mathrm{HG}}_{N-k,k}(x, y, z) \tag{3.5}$$

$$b(n, m, k) = \left[\frac{(N-k)!k!}{2^N n!m!}\right]^{1/2} \frac{1}{k} \frac{d^k}{dt^k}[(1-t)^n (1+t)^m]|_{t=0} \tag{3.6}$$

where $N = n + m = 2p + |\ell|$ is the order of the beam. It has been shown that because of this unitary transformation between all LG and HG modes, there is no capacity benefit in atmospheric turbulence when the average of the entire basis is considered [88]. This appears contradictory to the hypothesis presented in this work, however, we propose that a carefully chosen subset of HG modes is not subject to the work in [88]. In addition, there is a diversity benefit due to differences in the wavefront of the modes and short-term changes in atmospheric turbulence [47].

3.1.2 Atmospheric Turbulence

When a laser beam propagates through the atmosphere it encounters spatially and temporally varying refractive indices, mainly due to random temperature variations and convective processes. This randomly aberrates the beams wavefront. The Kolmogorov model for turbulent flow is the basis for many contemporary theories of turbulence and is able to relate these temperature fluctuations to refractive index fluctuations [72]. The average size of the turbulent cells are specified by a so-called inner scale, l_0, which is typically on the order of millimetres and an outer scale, L_0, which is on the order of meters [73]. Kolmogorov turbulence assumes $l_0 = 0$ and $L_0 = \infty$, thus the model's simplicity.

While models of turbulence typically only provide statistical averages for the random variations of the atmosphere, in most cases this is sufficient. The power spectral density of the refractive index fluctuations given by the Kolmogorov model is described by

$$\Phi^K_n(\kappa) = 0.033 C_n^2 \kappa^{-11/3} \quad \text{for} \quad 1/L_0 \ll \kappa \ll 1/l_0, \tag{3.7}$$

where $\kappa = 2\pi(f_x \cdot \hat{x} + f_y \cdot \hat{y})$ is the angular spatial frequency and C_n^2 is the refractive index structure parameter. We can use this to generate individual snapshots of turbulence in the form of phase screens with appropriate statistics [74]. Instead of C_n^2, turbulence strength is often specified using the Fried parameter [76], commonly known as the atmospheric coherence length,

$$r_0 = 0.185 \left(\frac{\lambda^2}{C_n^2 L}\right)^{-3/5} \tag{3.8}$$

where λ is the wavelength and L is the propagation distance. Furthermore, a more general parameter to specify turbulence strength is the Strehl Ratio (SR), which is the ratio of the average on-axis beam intensity with, I, and without, I_0, turbulence and is given by

$$\mathrm{SR} = \frac{\langle I \rangle}{I_0} \approx \frac{1}{[1 + (D/r_0)^{5/3}]^{6/5}}, \tag{3.9}$$

where D is the aperture diameter. In summary, turbulence leads to scintillation, beam wandering and other effects, and is the reason why the on-axis beam intensity, I, is reduced on average. For the intensity reduction of the individual modes (the MDL) we use the intensity of individual modes, S_i, instead of the overall intensity of the beam, I,

$$\mathrm{MDL}_i = 1 - \frac{S_i}{S_{i,0}}, \tag{3.10}$$

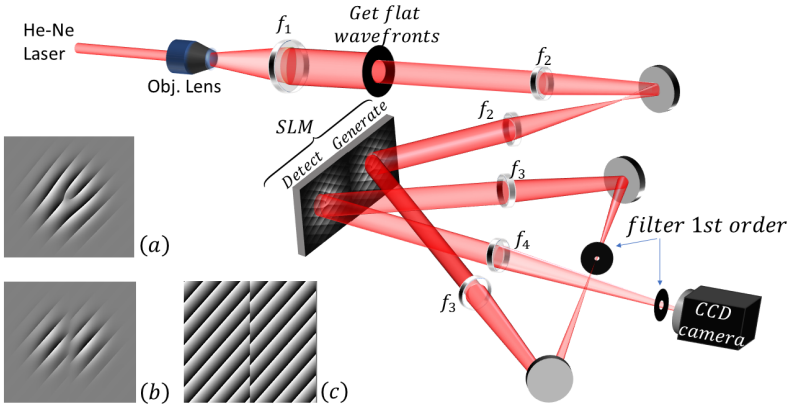


Figure 3.2: Modal decomposition setup with sample insets of the holograms used: (a) LG_1^0, (b) HG_1^0 and (c) BHG_1^0.

where $S_{i,0}$ is the intensity of mode i in the absence of turbulence. Typically, the energy in the individual modes is spread to neighbouring modes, as mentioned in the introduction. This mode crosstalk with respect to mode i is defined as the fraction of the total intensity not in mode i:

$$C_i = 1 - \frac{S_i}{\sum_j S_j}, \tag{3.11}$$

where $\sum_j S_j$ is the sum of the intensities in all the modes, including mode i.

3.2 Experimental Setup and Methodology

In order to determine whether the MDL and crosstalk characteristics of HG, BHG and LG modes is different and ultimately if one mode set performs better than the others in Kolmogorov turbulence, we use a modal decomposition setup which makes use of a Spatial Light Modulator (SLM) [66]. The SLM is used to create the required mode, aberrate that mode using emulated Kolmogorov turbulence, and finally perform a modal decomposition. The MDL and crosstalk for each set is then calculated.

A diagram of the experimental setup is shown in Fig. 3.2. A 633 nm laser beam from a Helium-Neon laser is expanded using an objective lens and lens f_1. The flat wavefront from the small central region of the expanded beam is selected using an aperture and is imaged onto the SLM screen using a $4f$ system. A HoloEye Pluto SLM is divided into two halves, for two separate holograms. The first hologram is used to modulate the incoming flat beam into the desired mode as well as to add turbulence. The resulting field is imaged to the second half of the SLM where modal decomposition is performed. A camera is placed at the focal point of lens f_4 to measure the on-axis intensity, which represents S_j in Sec. 3.1.2, Eqs. 3.10 and 3.11.

For each mode in each set, HG, BHG and LG, modal decomposition was performed for one hundred random turbulence screens for each Strehl Ratio from 1.0 (no turbulence) to 0.1 (strong turbulence). The results were then averaged according to Strehl Ratio. To ensure a fair comparison, we used modes with the same beam propagation factor, $M^2 = n + m + 1 = 2p + |\ell| + 1$, for (B)HG and LG modes respectively. Table 3.1, below, details which modes are used for each set, graphically shown in Fig. 3.1. Note that for $M^2 = 3$, we also include a case which does not include the "symmetrical" $(B)HG_1^1$ mode, denoted by the asterisk. This case is considered because the HG_1^1 mode does not have the same benefit of

tip/tilt invariance as the other (B)HG modes in the set. It is expected that when this mode is included, the average performance of the set will be more similar to the performance of the LG modes.

Table 3.1: Mode sets used in the experiment. The asterisk denotes the case that excludes the symmetrical (B)HG$_1^1$ mode.

M^2	LG (ℓ, p) Modes	(B)HG (n, m) Modes
2	(-1,0), (1,0)	(1,0), (0,1)
3	(-2,0), (2,0)	(2,0), (1,1), (0,2)
3*	(-2,0), (2,0)	(2,0), (0,2)

The experimental setup was verified by performing a modal decomposition for each mode set without turbulence. As shown in Fig. 3.3, there is no crosstalk except where it is expected in the case of the BHG modes.

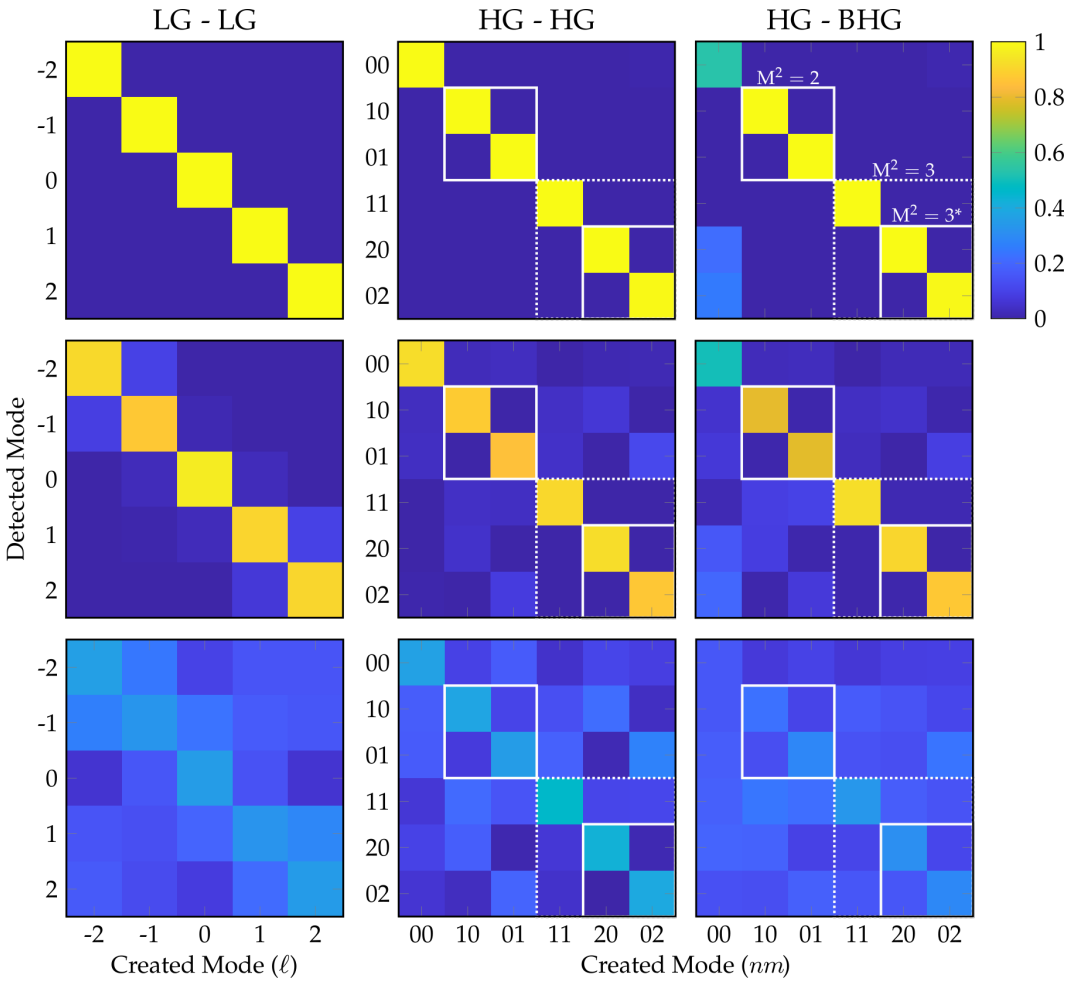


Figure 3.3: Experimental setup verification showing the crosstalk matrices for the various mode sets at different turbulence strengths. Top: no turbulence (SR=1.0). Middle: mild turbulence (SR=0.7). Bottom: strong turbulence (SR=0.1). Mode groups corresponding to modes in Fig. 3.1 and Tab. 3.1 are highlighted as it is clear that there is relatively little crosstalk within each group.

3.3 Results and Discussion

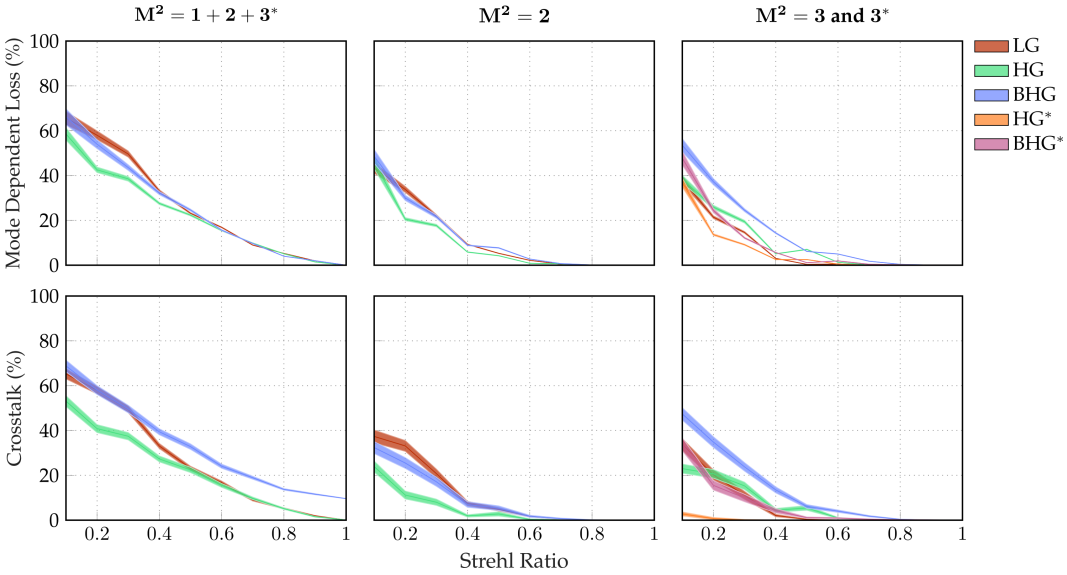


Figure 3.4: Mode Dependent Loss (top) and Crosstalk (bottom) of the LG, HG and Binary HG mode sets for different turbulence strengths form strong turbulence (SR=0.1) to no turbulence (SR=1.0). The shaded area of each curve represents the measurement error. From Tab. 3.1, the 3^* case excludes the HG_1^1 mode and is shown as the additional HG* and BHG* curves.

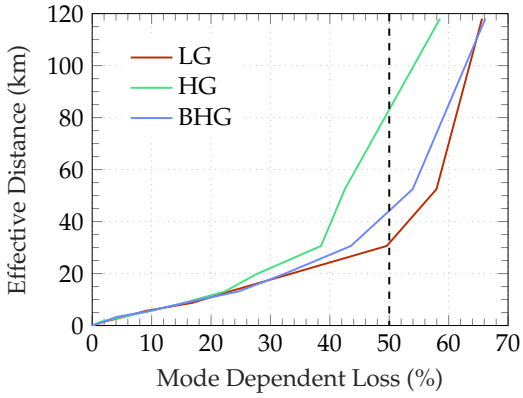


Figure 3.5: Effective propagation distance calculated from the Strehl Ratio using Eqs. 3.9 and 3.12 for the average ($M^2 = 1$, 2 and 3^*) of each mode set. At the vertical dotted line the difference between HG and LG is 51 km and BHG and LG is 12 km. This represents an upper bound due to weak turbulence alone as aperture collection losses due to divergence and beam wander are neglected, as are atmospheric attenuation effects such as aerosol scattering.

The MDL results are shown at the top of Fig. 3.4. We show three cases, defined by the beam propagation factor, M^2. The Gaussian case, where $M^2 = 1$ is not shown explicitly as it corresponds to the measurement of the Strehl Ratio but it is included in the average case. We see that compared to LG modes, HG modes almost always exhibit a lower (better) or

similar MDL. The BHG modes exhibit similar MDL to the LG modes, and are thus worse than HG modes, but this is expected because of their weaker orthogonality.

Interestingly, when the (B)HG$_1^1$ modes are included ($M^2 = 3$), the set exhibits significantly poorer performance in turbulence than without the (B)HG$_1^1$ mode ($M^2 = 3^*$). As visible in Fig. 3.1, the (B)HG$_1^1$ is not tip or tilt invariant, making it more similar to an LG mode.

The crosstalk results shown at the bottom of Fig. 3.4 agree with the MDL results in that HG modes exhibit lower crosstalk than LG modes. As expected, the BHG modes consistently show more crosstalk than either the HG or LG modes. Again, when the (B)HG$_1^1$ mode is excluded, the results agree with our hypothesis that HG modes are more resilient to turbulence than LG modes.

Strangely, the percentage crosstalk of the HG modes excluding the HG$_1^1$ is very low. This result agrees with a visual inspection of Fig. 3.3, where it is clear that in general the $M^2 = 3^*$ case experiences low crosstalk within the set, lending confidence to the result. While it has not been explicitly shown elsewhere, it is logical that the tip/tilt resilience of HG modes should extend to higher order modes with the same symmetry [45]. This resilience is visible in Fig. 3.3 in the crosstalk between the $M^2 = 2$ and 3^* sets.

The consequences of these results are important for FSO communications. Carefully chosen modes from the HG basis should result in superior MDM performance over modes from the LG basis, assuming the optical components such as the transmit and receive apertures have suitable geometry or are larger than the beams. The very low crosstalk results for HG modes with orthogonal symmetry is of particular interest. More important is the impact on FSO link distances. We see from Eqs. 3.8 and 3.9 that a lower Strehl Ratio is equivalent to a longer propagation distance, obviously ignoring atmospheric attenuation and beam divergence, for example. Using MDL as the factor of comparison, we can find the effective propagation difference for each turbulence strength,

$$L \approx \frac{0.060\lambda^2}{C_n^2 r_0^{5/3}}, \tag{3.12}$$

and arbitrarily assuming $C_n^2 = 10^{-14}$ m$^{-2/3}$, which is a typical value [73]. The effective propagation distance for each mode set is plotted in Fig. 3.5, where is it clear that HG and often BHG modes are superior to LG modes in terms of effective propagation distance for most MDL values. For instance, arbitrarily choosing a MDL of 50% in a turbulence strength $C_n^2 = 10^{-14}$ m$^{-2/3}$, an LG mode could propagate 31 km whereas an HG mode would propagate 83 km. This is a significant increase in range. It must be emphasised, however, that this calculation represents an upper bound due to weak turbulence alone as aperture collection losses due to divergence and beam wander are neglected, as are atmospheric attenuation effects such as aerosol scattering.

Our study has considered the typical scenario where the beam is sufficiently expanded so that the Rayleigh length is much larger than the propagation distance. In this case the beam is assumed always to be in the near field (weak turbulence) and so the turbulence can be approximated as a single phase screen. This is also valid for any beam when the turbulence is weak, or when the turbulence is indeed a thin screen, e.g., a vertical path to a satellite. A consequence is that the aberrations remain phase-only, e.g., tip/tilt remain as angle of arrivals. In a real-world FSO link more practical issues such as divergence, attenuation and beam wander must be considered.

To this end we point out that we have selected modes with identical beam propagation factor and so their divergence is the same. Attenuation and scattering are largely beam size and wavelength dependent, so again the mode sets will have the same response, while it is already known that HG modes are more tolerant to beam wander (lateral off-sets at the detector as shown in Fig. 3.6) [43–45]. Thus, while the realisable propagation distance would indeed be limited by practical factors, the benefit of certain (B)HG modes over LG modes should still enable longer range FSO communications because of the lower MDL than LG

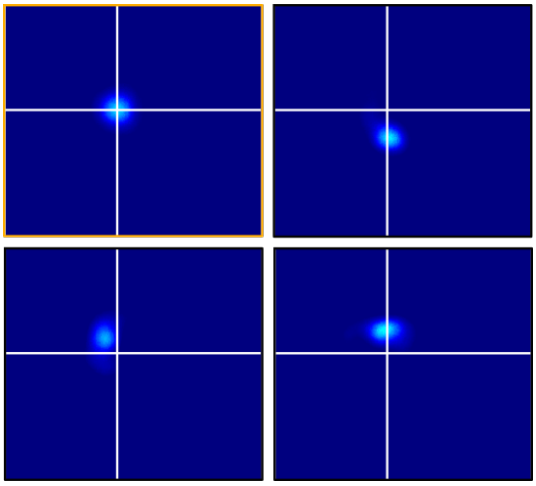


Figure 3.6: Experimental images of Gaussian beam wander in the far field of the turbulence screen. The top left image is the beam without turbulence.

modes and the identical or better resilience to other real-world effects. We hope that this laboratory prediction will encourage just such a real-world realisation.

3.4 Conclusion

Atmospheric turbulence predominantly manifests as angle of arrival fluctuations (tip/tilt) and thus wandering of a FSO laser beam, resulting in fading (or MDL) as well as mode-crosstalk. Given the complex phase structure of LG and HG modes, it was unknown whether the higher order effects of turbulence would overcome the known beam wander resilience of HG modes over LG modes. In this work we experimentally show that carefully chosen HG and binary HG modes are significantly more resilient to single phase screen Kolmogorov turbulence than LG beams with the same beam propagation factor, M^2. Lower crosstalk results in higher capacity mode division multiplexed systems, but more importantly, the lower MDL experienced by HG modes over LG modes means that they can propagate significantly further. At a MDL of 50%, we show a 167% increase in theoretical range of non-symmetric HG modes over similar order LG modes. FSO communications are a possible technology which can be used to bridge the digital divide in Africa where large geographical distances must be traversed, provided the range of such systems makes this course economical over the cost of laying fibre. This work is a significant step towards improving the range of FSO links.

CHAPTER 4

On the Resilience of Scalar and Vector Vortex Modes in Turbulence

This chapter is based on the following publication:

M. A. Cox, C. Rosales-Guzmán, M. P. J. Lavery, D. J. Versfeld and A. Forbes, "On the resilience of scalar and vector vortex modes in turbulence," *Optics Express*, vol. 24, no. 16, p. 18105, Aug. 2016.

The author conceptualised the work, performed the experimental measurements, assisted with the theoretical calculations, analysed the data and wrote the majority of the paper.

VECTOR vortex modes are non-separable states of light in which polarisation and Orbital Angular Momentum (OAM) are coupled, which results in an in-homogeneous polarisation distribution [89, 90]. Recently, the use of vector modes was proposed as an alternative to scalar modes to encode information [91]. It has been shown numerically that non-uniformly polarised beams such as a vector vortex beams are analogous to partially coherent beams, in as far as their resilience to atmospheric turbulence is concerned [41, 92]. Another study has postulated that the polarisation distribution of a vector vortex beam is maintained even after its intensity distribution has degraded and thus a portion of the information encoded in polarisation is still present [93]. From these studies it has been inferred that vector vortex beams are more resilient to turbulence as compared to their scalar counterparts [41, 92, 93].

Here we show that Cylindrical Vector Vortex (CVV) modes are *not* more resilient to atmospheric turbulence than their scalar OAM counterparts. We confirm this experimentally by measuring the crosstalk between basis elements of both mode sets, perturbed by Kolmogorov, thin phase screens encoded on a polarisation invariant Spatial Light Modulator (SLM). In comparing the modal crosstalk induced in each case, it is determined that although the crosstalk between modes within the scalar vortex and CVV bases is distributed differently, the total crosstalk is in fact identical within experimental error. The coupling between OAM and polarisation in CVV beams is not sufficient to make their phase variation less susceptible to atmospheric turbulence when compared to circularly polarised scalar vortex beams.

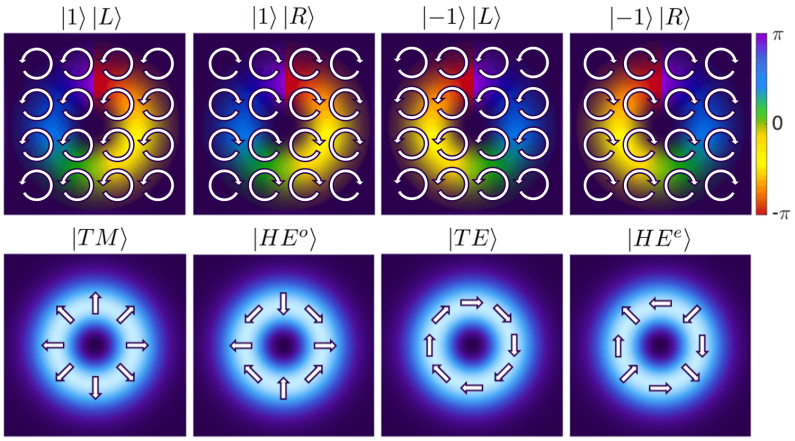


Figure 4.1: Illustration of the scalar (top) and CVV (bottom) modes described in Eq. 4.1 and Eq. 4.2 respectively, with arrows indicating polarisation distribution which is constant for scalar and variable for CVV modes, for $\ell = \pm 1$. The phase of the four scalar modes in the transverse plane increases from $-\pi$ (red) to π (blue) for positive ℓs and decreases in the opposite direction for negative ℓs whereas the phase for CVV modes is a superposition of both.

4.1 Theory

A scalar basis set can be constructed by combining the degree of freedom provided by circular polarisation with the degrees of freedom given by the infinite set of OAM modes, illustrated in Fig. 4.1. These modes can be written, using Dirac notation for brevity, as:

$$|R^+\rangle = |\ell\rangle\,|R\rangle\,, \tag{4.1a}$$

$$|L^+\rangle = |\ell\rangle\,|L\rangle\,, \tag{4.1b}$$

$$|R^-\rangle = |-\ell\rangle\,|R\rangle\,, \tag{4.1c}$$

$$|L^-\rangle = |-\ell\rangle\,|L\rangle\,, \tag{4.1d}$$

where, R and L denotes right and left circular polarisation, respectively, as opposed to link length as is used elsewhere in this work, and $\ell \in \mathbb{Z}$ relates to the amount of orbital angular momentum, $\ell\hbar$, per photon [94]. The elements of this set are orthogonal to each other.

CVV modes are non-separable states of light where polarisation and OAM modes are coupled. A basis set of four orthogonal CVV modes can be constructed as linear combinations of the scalar mode set in Eq. 4.1. The resulting modes carry no overall angular momentum and their transverse polarisation state is not constant, illustrated in the bottom row of Fig. 4.1. Akin to the scalar case, these modes can be represented in the circular polarisation basis using Dirac notation as:

$$|TM\rangle = 2^{-1/2}(|\ell\rangle\,|R\rangle + |-\ell\rangle\,|L\rangle), \tag{4.2a}$$

$$|TE\rangle = 2^{-1/2}(|\ell\rangle\,|R\rangle - |-\ell\rangle\,|L\rangle), \tag{4.2b}$$

$$|HE^e\rangle = 2^{-1/2}(|\ell\rangle\,|L\rangle + |-\ell\rangle\,|R\rangle), \tag{4.2c}$$

$$|HE^o\rangle = 2^{-1/2}(|\ell\rangle\,|L\rangle - |-\ell\rangle\,|R\rangle). \tag{4.2d}$$

Each mode in a given set (vector and scalar) is orthogonal with the others in the set, and mutually unbiased across the sets. Moreover, each of the modes described by Eq. 4.1 and 4.2 can be represented on a high order Poincaré sphere [89, 95]. Note that in Eq. 4.2 the relative amplitude and phase between the two components has not been shown.

4.1.1 Inter-mode crosstalk

In the presence of atmospheric turbulence, the polarisation of a beam is not affected because the atmosphere is not birefringent, which can readily be validated by tilting ones head when wearing polarised sunglasses (e.g., Kolmogorov turbulence assumes a homogeneous and isotropic atmosphere) [96]. The spatial degree of freedom, however, experiences aberrations which result in the coupling of modes into neighbouring modes, degrading their orthogonality. The amount of mode coupling or crosstalk is dependent on the strength of the turbulence in the channel, which can be expressed, in general, by:

$$|\ell\rangle \xrightarrow{turb.} \sum_{\ell'} p_{\ell-\ell'} |\ell'\rangle, \tag{4.3}$$

where $p_{\ell-\ell'}$ are the mode coupling weightings described by some distribution (e.g., p_0 would represent the modal power in the original OAM mode). This is used to find general expressions for what a given mode propagating through turbulence will transform into. For instance, the final state of the scalar mode $|R^+\rangle$ will be given by:

$$|R^+\rangle \xrightarrow{turb.} p_0 |\ell\rangle |R\rangle + p_{2\ell} |-\ell\rangle |R\rangle = |R^+_{turb.}\rangle \tag{4.4}$$

Analogous expressions can be found for $|R^-\rangle$, $|L^+\rangle$ and $|L^-\rangle$. Similarly, applying Equation 4.3 to a vector mode $|TM\rangle$:

$$|TM\rangle \xrightarrow{turb.} p_0 |\ell\rangle |R\rangle + p_0 |-\ell\rangle |L\rangle + p_{-2\ell} |\ell\rangle |L\rangle + p_{2\ell} |-\ell\rangle |R\rangle = |TM_{turb}\rangle . \tag{4.5}$$

Analogous relations for $|TE\rangle$, $|HE^e\rangle$ and $|HE^o\rangle$ can also be found.

The crosstalk for each input mode is the magnitude of the inner product between each input mode and all the expected output modes after turbulence. By way of example, the inner product of the scalar mode $|R^+\rangle$ with the mode $|R^+_{turb}\rangle$, will be:

$$|| \langle R^+|R^+_{turb}\rangle ||^2 = || \langle \ell| \langle R| (p_0 |\ell\rangle |R\rangle + p_{2\ell} |-\ell\rangle |R\rangle)||^2 = ||p_0||^2. \tag{4.6}$$

Similarly, the inner product of the vector mode $|TM\rangle$ with the mode $|TM_{turb}\rangle$ will be:

$$\begin{aligned} || \langle TM|TM_{turb}\rangle ||^2 = ||(\frac{1}{\sqrt{2}}(\langle \ell| \langle R| + \langle -\ell| \langle L|)(p_0 |\ell\rangle |R\rangle\, p_0 |-\ell\rangle |L\rangle + p_{-2\ell} |\ell\rangle |L\rangle \\ + p_{2\ell} |-\ell\rangle |R\rangle)||^2 = ||p_0||^2 \end{aligned} \tag{4.7}$$

The crosstalk terms for all of the modes can be summarised in the form of a matrix as

$$M_{scalar} = \begin{pmatrix} ||p_0||^2 & 0 & ||p_{-2\ell}||^2 & 0 \\ 0 & ||p_0||^2 & 0 & ||p_{-2\ell}||^2 \\ ||p_{2\ell}||^2 & 0 & ||p_0||^2 & 0 \\ 0 & ||p_{2\ell}||^2 & 0 & ||p_0||^2 \end{pmatrix}, \tag{4.8}$$

$$M_{vector} = \begin{pmatrix} ||p_0||^2 & \frac{||p_{-2\ell}+p_{2\ell}||^2}{4} & 0 & \frac{||p_{-2\ell}-p_{2\ell}||^2}{4} \\ \frac{||p_{-2\ell}+p_{2\ell}||^2}{4} & ||p_0||^2 & \frac{||(p_{-2\ell}-p_{2\ell}||^2}{4} & 0 \\ 0 & \frac{||p_{-2\ell}-P_{2\ell}||^2}{4} & ||p_0||^2 & \frac{||p_{-2\ell}+P_{2\ell}||^2}{4} \\ \frac{||p_{-2\ell}-p_{2\ell}||^2}{4} & 0 & \frac{||p_{-2\ell}+p_{2\ell}||^2}{4} & ||p_0||^2 \end{pmatrix}. \tag{4.9}$$

Note that here M is different to the beam quality factor, M^2. Notice that the terms in the diagonal are identical both cases. Under zero turbulence, where the mode coupling weightings for the crosstalk terms can be assumed to be zero ($p_{2\ell} = p_{-2\ell} = 0$), only the terms in the diagonal remain. This is consistent with the notion that when propagating in free-space with no aberrations induced by atmospheric turbulence, the output mode

equals the input mode. The total crosstalk, N, in each case can be computed by adding the off-diagonal elements as:

$$N_{vector} = \sum_{i \neq j} M_{vector} = (||p_{2\ell} + p_{-2\ell}||^2 + ||p_{2\ell} - p_{-2\ell}||^2) = 2(||p_{-2\ell}||^2 + ||p_{2\ell}||^2), \quad (4.10)$$

$$N_{scalar} = \sum_{i \neq j} M_{scalar} = 2(||p_{-2\ell}||^2 + ||p_{2\ell}||^2), \quad (4.11)$$

which therefore leads to our claim that the total crosstalk in each case is in fact identical:

$$N_{scalar} = N_{vector} = 2(||p_{-2\ell}||^2 + ||p_{2\ell}||^2). \quad (4.12)$$

4.2 Experiment

Figure 4.2 shows the experimental setup used to corroborate our theoretical findings. It consisted of three main stages: generation of scalar and CVV modes, turbulence using a Spatial Light Modulator (SLM) and finally, detection. In the first stage, both scalar and CVV modes were generated using a q-plate ($q = 1/2$) in conjunction with polarisers and wave plates [97]. For the second stage, a HoloEye Pluto SLM was used (PLUTO-VIS, 1920×1080 pixels with 8 μm pitch, calibrated for a 2π maximum phase shift at 633 nm) to simulate atmospheric turbulence. Random Kolmogorov phase screens were used, specified by their Strehl Ratio (SR) [98]. Since this SLM is only able to modulate horizontally polarised light, a polarisation invariant arrangement was implemented, as illustrated in Fig. 4.2, following the approach in [99, 100]. In the last stage, the perturbed modes were detected by inverting the creation stage (exploiting the reciprocity of light) followed by an inner product measurement to quantitatively infer the mode coupling weightings by using a technique known as modal decomposition [58, 101].

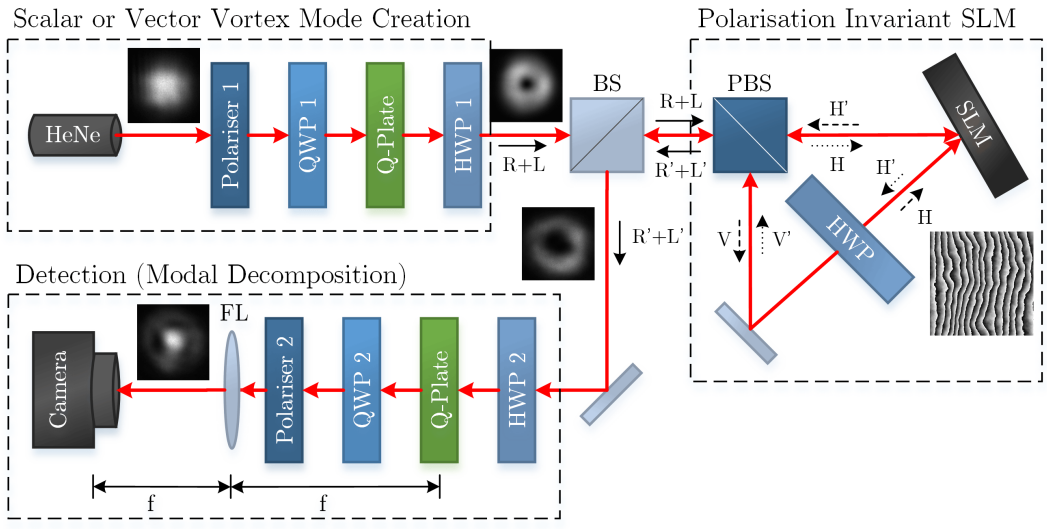


Figure 4.2: Simplified schematic diagram of the experimental setup showing the three main parts. The polarisation invariant SLM is made up by a PBS, mirror and half wave plate rotated to 45° so that arbitrarily polarised scalar and vector beams can be modulated by the SLM, which is encoded with random Kolmogorov turbulence screens. The perturbed beams which return along the same path as the incoming beams are directed by a BS to the detection part of the setup which performs modal decomposition.

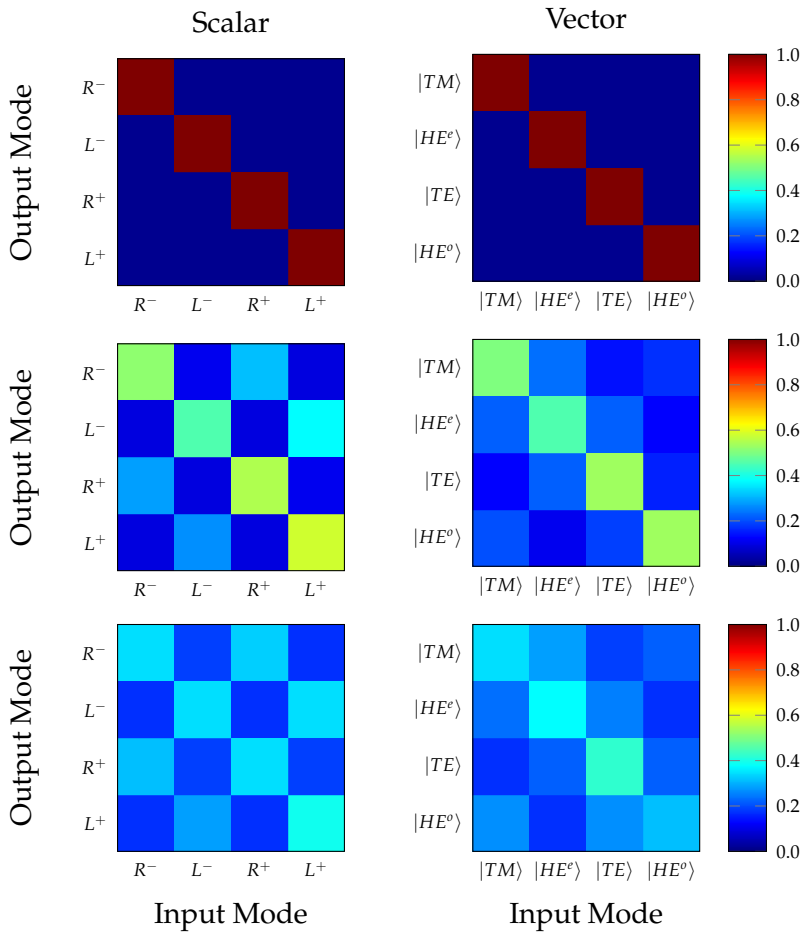


Figure 4.3: Comparison of vector and scalar crosstalk for $SR = 1.0$ (top) for experimental setup validation and $SR = 0.6$ (middle) and $SR = 0.2$ (bottom).

Each input mode was perturbed by one hundred discrete instances of thin phase atmospheric turbulence of a specific strength. The strength of turbulence was increased in increments of 0.1 from SR 0.1 to 1.0. The channel matrices, M_{scalar} and M_{vector}, described in Sec. 4.1 were then generated for each turbulence strength using the averaged and normalised intensity data for comparison to the theoretical calculations in Eqs. 4.8 and 4.9.

4.3 Results and discussion

The experimental setup was verified by encoding the SLM with SR $= 1.0$ turbulence, which is simply a grating. This is the control measurement for the experiment and the crosstalk was zero, as expected, shown in Fig. 4.3.

Figure 4.3 also shows the channel matrix comparison for SR $= 0.6$ and 0.2 of scalar and vector cases. These two Strehl Ratio's are arbitrary but were chosen because they demonstrate cases for medium and strong turbulence and the clear effect of stronger turbulence, where power is spread from the signal on the diagonal into the crosstalk elements.

The distribution of crosstalk visible in Fig. 4.3 is very similar to the theory presented in Eqs. 4.8 and 4.9. However, according to the theory and the assumption that crosstalk does not occur across polarisation states, some elements in the matrices shown in Fig. 4.3 should

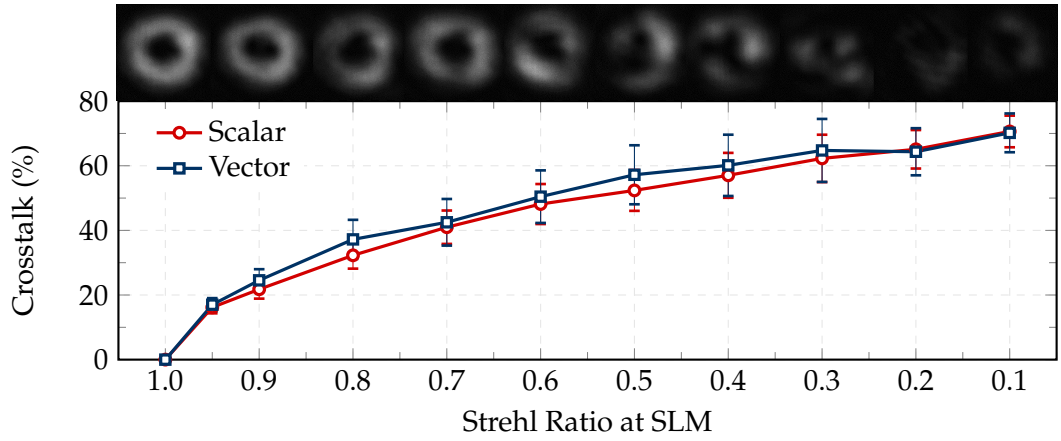


Figure 4.4: Percentage of the signal in the crosstalk of scalar and vector cases showing insets of the beam with increasing turbulence. Both mode sets have the same crosstalk performance. Error bars are the standard error of the mean.

be dark blue (zero) when in fact they show a small amount of signal. This is attributed to the normalisation of the low dynamic range signal in strong turbulence and the efficiency of the PBS.

In order to compare the scalar and vector cases against each other, the crosstalk elements for each input mode were added to each other according to Eq. 4.13, similar to the theory in Sec. 4.1.1. Since each row of the crosstalk matrix is already normalised, the sum must be re-normalised to a percentage, resulting in a total average crosstalk percentage for each turbulence strength for each mode set, visible in Fig. 4.4.

$$C = \frac{1}{4} \times \sum_{i \neq j} M \times 100\%, \tag{4.13}$$

where M is the measured scalar or vector channel matrix and C is the associated crosstalk percentage. The crosstalk performance for both scalar and vector modes is identical within the measurement error for all turbulence strengths. These results agree well with the theory presented in Sec. 4.1 and indicate that there is no performance benefit to using CVV modes over scalar vortex modes in a thin phase turbulence regime with no birefringence. It should be noted that a similar approach may be used for other basis sets of vector and scalar modes, however, the results in this paper cannot be extended to modes with asymmetric spatial indices such as $|\ell\rangle |R\rangle + |p\rangle |L\rangle$, for example, as their resilience to turbulence cannot be assumed to be equal. Additionally, while it is expected that scalar and CVV modes with higher topological charge will continue to have identical overall crosstalk performance as the theory is general, the absolute values of the crosstalk percentage will vary [38].

Although the overall crosstalk performance for scalar and CVV beams is identical, the crosstalk distribution across modes within the bases are different. It is clearly visible in Fig. 4.3 that the polarisation component of the scalar basis strongly limits crosstalk between certain modes, however in the vector basis this is not the case. Consequently, the use of CVV modes may in fact limit the possible information capacity of a communication system.

4.4 Conclusion

It has been inferred in the literature that vector vortex modes are more resilient to atmospheric turbulence than their scalar counterparts. Here we define two similar scalar and cylindrical vector vortex mode bases and theoretically show that their crosstalk in turbulence

is the same. This result was then verified experimentally in the thin phase, Kolmogorov regime with various turbulence strengths. The experimental results show identical crosstalk performance within the experimental error.

CHAPTER 5

Modal Diversity for Robust Free-Space Optical Communications

This chapter is based on the following publication:

M. A. Cox, L. Cheng, C. Rosales-Guzmán and A. Forbes, "Modal Diversity for Robust Free-Space Optical Communications," *Physical Review Applied*, vol. 10, no. 2, p. 024020, Aug. 2018.

The author conceptualised the work, performed the experimental measurements, analysed the data and wrote the majority of the paper.

UPON propagation through the atmosphere, turbulence distorts the wave-front, amplitude and phase of the launched modes. Amplitude and phase fluctuations lead to so-called fading errors in a communication system with a certain probability, and hence deteriorate the overall performance. In an MDM system these distortions also cause correlation between channels, leading to crosstalk and which usually results in further communication errors [9, 82]. These effects are dependent on the path that the beam propagates through and so when several statistically independent paths are used, due to a separation of at least r_0 (the Fried Parameter, which is a measure of the transverse distance over which the refractive index is correlated [76]), the probability of error is reduced [31]. This is the basis for what is known as diversity and the so-called diversity gain can often be predicted by using probabilistic models applied to a range of mode types [81, 82, 102–106]. Diversity is considered the complement to multiplexing, reducing errors rather than directly increasing capacity [48]. While optical MDM has been extensively studied, diversity, and in particular modal diversity, has received little attention. This is not the case in fields such as radio communications, where diversity is harnessed as a matter of course [107, 108].

In this work, we hypothesize and then experimentally demonstrate that a carefully chosen combination of identical radius HG and LG modes, each transmitted co-linearly at a lower intensity to conserve the total transmit power, will result in a diversity gain, thus alleviating the issue of large (or multiple) transmit and receive apertures while also significantly improving the robustness of the channel.

In the following section, a generalised model for the diversity channel is provided. An explanation of the difference between conventional multiplexing and diversity is also given. Section 5.2 describes the specific choice of modes required to achieve diversity without r_0

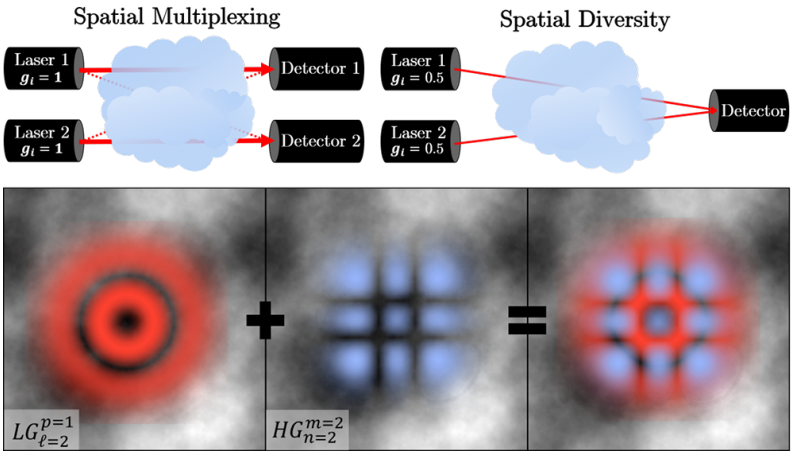


Figure 5.1: Illustrative comparison of spatial multiplexing which is used for increased bandwidth (top left), conventional spatial diversity which is used for increased robustness (top right) and our modal diversity scheme which does not require path separation (bottom). In conventional diversity the transmitted beams, irrespective of mode, take different paths separated by some distance greater than r_0. In modal diversity, different modes are used with half the original transmit power (g_i) but with each travelling the same path: the separation is in mode space not physical space.

aperture separation, as well as the experimental setup. Results of the experiment and a discussion thereof can be found in Sec. 5.3 and the conclusion is in Sec. 5.4.

5.1 Channel Model

In a typical, un-coded diversity model, multiple (N) transmitters (lasers) transmit identical signals, $x_i(t)$, at the same time with amplitude g_i. In comparison to a single transmitter case, the amplitude of each transmitter is scaled by $1/N$ to conserve overall transmit power. These signals propagate through separate channels represented by channel impulse responses, $h_i(t)$. This impulse response is typically modelled using a so-called "fading" probability distribution. The signal is then detected by a single receiver (photodiode) with receiver sensitivity r. The resulting received signal, $y(t)$, is then found from

$$y(t) = \frac{r}{N} \sum_{i}^{N} g_i x_i(t) * h_i(t) + n(t), \tag{5.1}$$

where an Additive White Gaussian Noise (AWGN) component, $n(t)$, may be incorporated.

Traditionally, "separate channels" means physically distinct paths, which in atmospheric turbulence requires a physical separation of at least r_0 (atmospheric coherence length). This is because atmospheric turbulence results in spatially distributed random changes in the refractive index of air, which cause random distortions to the spatial profile of a beams wave-front [76]. In modal diversity we interpret "separate channels" as distinct modes with differing behaviour in turbulence *without* being separated by a distance of r_0. We illustrate this concept in Fig. 5.1.

If the channel impulse responses are statistically independent, as well as the noise, then we can simply summarise the overall probability of an error in the diversity case as

$$\Pr[E_{\text{diversity}}] = \prod_{i} \Pr[E_i], \tag{5.2}$$

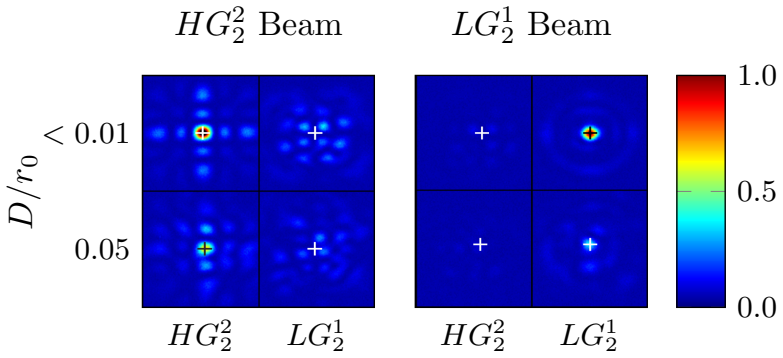


Figure 5.2: Experimental demonstration of the orthogonality of HG_2^2 and LG_2^1 modes with no turbulence (SR $= 1.0$ or $D/R_0 < 0.01$) and slight turbulence (SR $= 0.95$ or $D/r_0 = 0.05$) with measurement points shown as "+". On the left, only an HG_2^2 is transmitted and it is clear that there is no LG_2^1 component after modal decomposition. Similarly, on the right there is an LG_2^1 component but no HG_2^2 component in the decomposed beam.

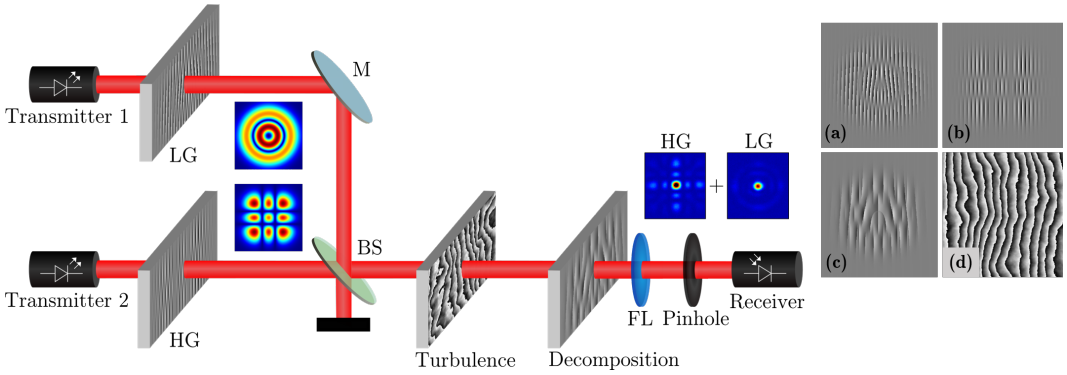


Figure 5.3: Experimental setup showing two transmitters and a single receiver for transmit diversity with example turbulence as an inset (a). The holograms along the bottom are for (b) generating an $LG_{\ell=2}^{p=1}$ beam, (c) generating an $HG_{n=2}^{m=2}$ beam and (d) superposition for decomposition of the generated LG and HG beams to a single detector. The flat grey areas on the holograms is due to complex amplitude modulation.

where the probability of an error occurring for the i^{th} channel is defined as $\Pr[E_i]$. This always results in a lower probability of error than a single channel case (since $\Pr[E_i] \leq 1$). This particular diversity scheme is similar to Equal Gain Combining (EGC) which is well known in radio communications [109, 110] and is in fact one of the reasons why we find multiple antennas on WiFi routers, for instance. The pertinent point is that if the different channels, whether formed by spatial modes or spatial paths, are not statistically independent then we can expect that there will be no gain in terms of robustness, measurable by Bit Error Rate (BER) or outage probability.

5.2 Experiment

5.2.1 Choice of Modes for Diversity

In Ref. [111], diversity was simulated using LG modes with a large mode spacing, with indices $\ell = +1, +8$ and $+15$. The results showed an improvement to the outage probability, or robustness, of a FSO link. Using modes from the same set necessitates differing (larger) mode orders, with the result that the receive aperture becomes impractically large with long propagation distances.

We address this issue in a novel manner by using identical order yet orthogonal HG_n^m and LG_ℓ^p beams, motivated by the fact that HG modes are robust to tip/tilt which are the primary aberrations of atmospheric turbulence [45]. Beams with the same mode order have the same propagation parameters resulting in the same field size at the receiving aperture (or detector). The order of the beams is given by $N = n + m = 2p + |\ell|$ for HG and LG beams respectively. An example of this are the modes in Fig. 5.1.

The completeness property of both bases allow us to express any element of one basis as a linear combination of elements from the other basis using the transformation relations below [87]:

$$LG_{n,m}(x,y,z) = \sum_{k=0}^{N} i^k b(n,m,k) HG_{N-k,k}(x,y,z) \tag{5.3}$$

$$b(n,m,k) = \left[\frac{(N-k)!k!}{2^N n!m!}\right]^{1/2} \frac{1}{k}\frac{d^k}{dt^k}[(1-t)^n(1+t)^m]|_{t=0} \tag{5.4}$$

The LG modes have been written in terms of n and m, which are indices typically used for HG modes. Traditionally, LG modes are given in terms of azimuthal index ℓ and radial index p, which can be recovered as $\ell = n - m$ and $p = \min(n, m)$. For example, the LG_2^1 mode may be written as

$$LG_2^1 = \frac{1}{2}HG_4^0 - \frac{i}{2}HG_3^1 + 0 \times HG_2^2 - \frac{i}{2}HG_1^3 - \frac{1}{2}HG_0^4. \tag{5.5}$$

Notice that the HG_2^2 component has a zero weighting, making the HG_2^2 mode orthogonal to the LG_2^1 mode. Figure 5.2 shows an experimental verification of this orthogonality. Conveniently, both of these modes have an order of $N = 4$, however, not all LG modes contain an orthogonal HG mode with the same mode order, and vice versa. Similarly, HG_4^4 is orthogonal to LG_6^1 with $N = 8$. Both of these mode sets were tested in the experiment.

5.2.2 Experimental Setup

The experimental setup consisted of two laser diodes which were individually modulated with identical On-Off Keying signals. In this modulation scheme, which is common in FSO systems, the presence of light (on) represents a binary "1" and the absence of light (off) is a binary "0". For demodulation, a threshold is used to determine whether the received signal if "off" or "on". As mentioned in the introduction, atmospheric turbulence will randomly modify the intensity of the signal by attenuation or crosstalk which may lead to incorrect detections and subsequent errors. The modulation was performed at low bandwidth using a custom Arduino-based system at approximately 1 kbit/s. A high bandwidth demonstration using expensive telecommunications equipment was deemed unnecessary for the purposes of this investigation as it is a proof of concept only.

As shown in Fig. 5.3, each beam was transformed using a Spatial Light Modulator (SLM) into either an LG or HG mode. The first diffraction order from each SLM was spatially filtered and both beams were then combined using a beam splitter to propagate co-linearly. Kolmogorov turbulence and modal decomposition were performed by another SLM [54, 73]. Finally, the resulting beam was filtered using a 50 μm precision pinhole after which the

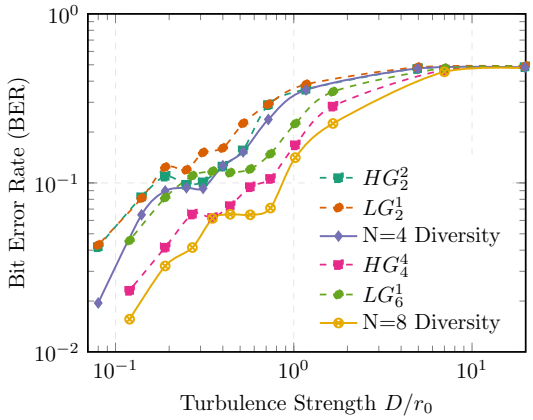


Figure 5.4: Bit Error Rate of modes with order $N = 4$ and 8 where $D = 1.4$ and 1.98 mm respectively with varying turbulence strength showing a clear improvement for the diversity cases. Larger modes are expected to experience lower turbulence in comparison to smaller modes.

intensity was measured by a photodiode for demodulation. The experiment was performed with varying turbulence strengths corresponding to a range of atmospheric coherence lengths (r_0) from 0.1 to 17 mm. These coherence lengths correspond to the Strehl Ratios 0.01 to 0.9 when applied to the beams with mode order $N = 4$. For each turbulence strength and each mode, one million random bits were tested against 1024 random Kolmogorov phase screens. The Bit Error Rate (BER) was then determined for each test case. Each mode was first tested individually at a specific intensity in a conventional single channel configuration to determine baseline BER performance for the experimental setup without diversity. Transmit diversity was then tested by transmitting a random bit-stream over the HG and LG modes simultaneously. It is important to note that in the diversity case half of the single channel intensity was used for each transmitter, resulting in the same total intensity as in the single channel case at the receiver. This is done to ensure a fair SNR comparison.

5.3 Results and Discussion

The BER results versus turbulence strength (D/r_0) are shown in Figs. 5.4 and 5.5. The BER of the diversity case is on average 23% better than that of the LG single channel case for almost all turbulence strengths. At the weakest turbulence strength, the improvement in diversity BER over both single channel cases is 54%. Due to the fact that the laser intensities were normalised, this can only be due to a diversity gain. It should be noted that the measured BER values are worse than what would be normally expected due to SLM flickering at a frequency close to that of the signal, which introduces noise and thus degrades the SNR. This issue does not affect our diversity claims, however, in a commercial communication system, BER's with an order of magnitude improvement over the results presented here can be expected.

Interestingly, the HG case is noticeably better than the LG case at medium turbulence strengths. Given that tip/tilt is the dominant aberration in atmospheric turbulence, this result agrees with the findings in Ref. [45] which demonstrate that HG modes are more resilient to tip/tilt aberrations than LG modes. At weaker turbulence strengths, characterised by smaller D/r_0 values, the difference between the HG_2^2 and LG_2^1 is no longer clearly visible where the difference between the HG_4^4 and LG_6^1 is quite prominent. The exact reason for this difference is the subject of further study, but we assume that this difference is due

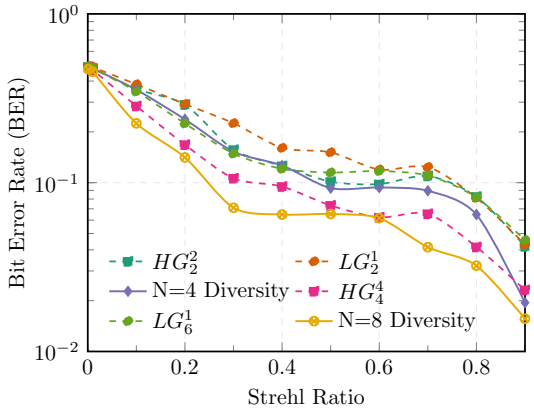


Figure 5.5: Bit Error Rate of modes with order $N = 4$ and 8 with varying turbulence strength in terms of the Strehl Ratio for $D = 1.4$ mm. The diversity case is typically better than the non diversity cases with significant gains in weaker turbulence.

to the fact that in comparison to lower order modes, the wavefronts of the higher order modes have a larger diameter as well as more phase variation and therefore would interact with turbulence in a more dissimilar manner. It is for this reason that modal diversity is possible. The diversity gain for the lower order modes is indeed still present because of the independent nature of the effect of turbulence on the HG and LG modes.

It is interesting to note that in the $N = 4$ case the BER converges to the worst case of 0.5 at $D/r_0 > 1$, as expected, however in the $N = 8$ case this only happens at approximately $D/r_0 > 6$. This indicates that even in stronger turbulence, where a conventional "single mode" system is overcome by errors, there is still a margin provided by the diversity which may prove useful when engineering a FSO link.

These results can be put into context by calculating the effective propagation distance gain at a specific BER [73]. If Kolmogorov turbulence is assumed, then we can write r_0 as a function of C_n^2, the refractive index structure parameter, the wavelength, λ, and the propagation distance, z:

$$r_0 = 0.185 \left(\frac{\lambda^2}{C_n^2 z} \right)^{3/5} \tag{5.6}$$

This equation can then be solved for z, resulting in:

$$z \approx \frac{0.0600647 \lambda^2}{C_n^2 r_0^{5/3}} \tag{5.7}$$

In this experiment, $\lambda = 660$ nm was used for ease of alignment as opposed to a standard telecommunications wavelength of 850 nm or even 1550 nm, for example. A typical value for C_n^2 is 10^{-14} m$^{-2/3}$ in strong turbulence [73]. Three arbitrary BERs were selected and in Table 5.1 the corresponding D/r_0 values are provided. From Eq. 5.7, the corresponding theoretical propagation distances have been calculated are shown in the table. It is clear that significant improvements in propagation distance are possible using modal diversity. In a well engineered system, with the inclusion of additional techniques such as forward error correction, robust modulation and interleaving as well as sensitive, low noise detectors and laser drivers, the BER performance will be improved significantly.

Table 5.1: Example relations between D/r_0 and the equivalent propagation distance, z, with $C_n^2 = 10^{-14}$ m$^{-2/3}$ for selected BERs according to Eq. 5.7 for the LG and diversity cases.

	Bit Error Rate		
	0.04	0.08	0.15
LG_2^1 D/r_0 (mm)	0.08	0.14	0.31
Diversity D/r_0 (mm)	0.10	0.19	0.52
LG_2^1 Distance (km)	0.24	0.55	2.13
Diversity Distance (km)	0.37	0.93	5.06
Distance Gain (%)	54	71	137

5.4 Conclusion

Traditionally, diversity has been theoretically and experimentally demonstrated with a r_0 (or greater) separation between transmit and/or receive apertures. In this work we have extended the concept of diversity to the modal diversity case, where a physical separation r_0 is not required, and have achieved significant diversity gain. Based on the proof-of-principle results presented in this letter, our technique is able to increase the allowable propagation distance (determined by a certain error rate) by a significant margin at both strong and weak turbulence strengths. This finding can be used to significantly improve future FSO communication links in terms of range and reliability.

Our novel approach makes use of two or more orthogonal, co-propagating beams from different modal bases to take advantage of the fact that modes with different spatial profiles will interact differently with turbulent space. Although modal diversity can also be achieved using sufficiently spaced LG modes [111], the required receive aperture size may become prohibitive. In our approach it is possible to choose orthogonal modes with the same order and thus the same size, negating the need for larger receive apertures than would otherwise be required.

A further implication of the use of different mode types is that the co-propagating modes may experience a lower degree of correlation than neighbouring adjacent modes within a single basis. This hypothesis should be tested in future, but this may indeed have interesting consequences and provide significant benefits to MDM or when MIMO signal processing is used. We speculate that it should be possible to formalise the concept of "separate" in terms of a newly defined modal distance, r_M, akin to the previous definition in terms of a physical distance, r_0. That is, how far would two modes have to be separated by in mode space, r_M, in order to ensure the same diversity gain as a physical separation of r_0?

CHAPTER 6

Modelling the Memory of Turbulence-Induced Beam Wander

This chapter is based on the following publication:

M. A. Cox, L. Gailele, L. Cheng and A. Forbes, "Modelling the Memory of Turbulence-Induced Beam Wander," submitted to *Journal of Lightwave Technology*, 2019.

The author conceptualised the work, performed the experimental measurements, analysed the data to create the model and wrote the majority of the paper.

ATMOSPHERIC turbulence can be described as two independent random processes, namely small and large scale [73]. The small scale effects of turbulence cause scintillation of a beam. This appears spatially as random deformations of intensity as well as phase aberrations of the beam wavefront which result in mode crosstalk - a significant problem for MDM. Large scale effects cause the beam itself to be deflected randomly as it propagates. This "cork-screwing" through the air eventually manifests as a lateral displacement at the receiver plane, where the beam randomly moves around the vicinity of the detection aperture (assuming reasonable alignment). Lateral displacement, in addition to angle of arrival fluctuations, manifest as beam wander at the focal (Fourier) plane of a receive aperture lens. Therefore, a small detector placed at this focal plane will measure fluctuations in intensity predominantly caused by beam wander, but also to a lesser extent by scintillation in the weak-to-moderate turbulence regime.

In a communication system, this is called turbulence induced signal fading. There have been numerous studies into mitigating this using spatial modes, diversity and various signal processing techniques [11, 13, 35, 44, 45, 47, 112], but turbulence remains a significant challenge. A key reason why turbulence is difficult to mitigate using signal processing and error correction coding is because the significant probability that the received intensity will drop below a usable threshold *for an extended period of time*. The situation when the received intensity is too low for reliable communication is called a "deep fade". In addition to this, the channel has memory which causes the received intensity to remain in a certain state for a finite period of time. The combined effect of deep fading and memory is generally catastrophic to communication, where millions or even billions of bits can be lost. Techniques exist to deal with these so-called slow fading memory channels in power-line communications, for instance, but they cannot be applied or tailored to FSO communications

in the absence of a suitable channel model [113].

This memory behaviour is not sufficiently accounted for in existing models for turbulence induced fading. Existing fading models, for example the recent double generalised gamma-gamma model [81], are able to accurately predict the average time a channel will be in deep fade over the long term, but inherently cannot provide information about the channel memory, which in this case is the average duration of deep fade intervals.

A potential solution exists in Taylor's frozen turbulence hypothesis. In this hypothesis, turbulent cells are assumed to move across the beam at a constant velocity. This would in essence result in a first order memory system. Based on this hypothesis, some temporal statistics of propagating beams have been measured and calculated in Refs. [30, 114, 115]. While these works make progress towards finding expressions for the temporal evolution of turbulence, there are still significant inaccuracies in the results when compared to measured data.

In this work we propose a novel approach to modelling beam wander and beam wander induced fading, which is the dominant cause of fading in weak-to-moderate turbulence [73]. This approach is based on the hypothesis that the movement of the wandering beam is not a true random walk, but rather a random walk that has a level of correlation between successive position samples. To demonstrate this new approach, we experimentally measure beam wander over a 150 m link and present an Auto-Regressive Moving-Average (ARMA) based random walk modal which not only reproduces the results of existing models, but more importantly, allows for accurately simulating and determining the parameters of the channel memory. We show how this approach allows for the simulation of beam wander induced modal crosstalk using Orbital Angular Momentum (OAM) modes as an example. The unique ability of this approach to realistically simulate the evolution of modal crosstalk may facilitate the future development of robust FSO-MDM systems.

6.1 Existing Beam Wander Models

In existing models, beam wander is spatially modelled by a Gaussian distribution which is characterised by a long-term average radial variance, $\langle r_c^2 \rangle$, as well as the size of the received beam without any averaging (the short-term beam), denoted by ω_{ST}, illustrated in Fig. 6.1 [73, 116–120]. It is intuitive to think that a smaller short-term beam which wanders around a receive aperture will result in a larger Gaussian shaped long-term beam, according to the central limit theorem [121]. The size of the long-term beam, ω_{LT}, is given by

$$\omega_{\mathrm{LT}}^2 = \omega_{\mathrm{ST}}^2 + \langle r_c^2 \rangle \,. \tag{6.1}$$

Several analytical solutions for the beam wander radial variance exist. For infinite outer scale Kolmogorov turbulence, the beam wander radial variance is given by

$$\langle r_c^2 \rangle = 2.42 C_n^2 L^3 \omega_0^{-1/3} {}_2F_1(1/3, 1; 4; 1 - |\Theta_0|) \,, \tag{6.2}$$

where C_n^2 is the refractive index structure constant which describes the strength of the turbulence, L is the propagation distance, ω_0 is the initial beam waist, ${}_2F_1$ is the hypergeometric function and Θ_0 is the beam parameter [73]. For a collimated beam ($\Theta_0 = 1$) the expression reduces to

$$\langle r_c^2 \rangle = 2.42 C_n^2 L^3 \omega_0^{-1/3}, \tag{6.3}$$

and for a finite outer scale turbulence and a collimated laser beam, Eq. 6.2 becomes

$$\langle r_c^2 \rangle = 2.42 C_n^2 L^3 \omega_0^{-1/3} \left[1 - \left(\frac{\kappa_0^2 \omega_0^2}{1 + \kappa_0^2 \omega_0^2} \right)^{1/6} \right]. \tag{6.4}$$

In addition to the information provided by long-term averages and variances, it is often a requirement to perform Monte-Carlo simulations which require short-term information.

In a well aligned optical communication system, the receiver photodiode would ideally be situated at the centre of the long term beam. By approximating the received beam as Gaussian with size ω_{ST}, the received intensity at a moment in time when the beam wanders to a random radius is given by

$$I_t(r) = I_0 \exp\left[-2\frac{r_{c,t}^2}{\omega_{ST}^2}\right], \tag{6.5}$$

where I_0 is the intensity at the centre of the beam and as before, the random variable $r_c = N(0, \langle r_c^2 \rangle)$. The position of the short-term beam can instead be represented in Cartesian rather than Polar coordinates, and the angle can be ignored due to symmetry:

$$r_{c,t}^2 = \beta_{x,t}^2 + \beta_{y,t}^2 \tag{6.6}$$

where $\beta_{x,t}$ and $\beta_{y,t}$ are Cartesian coordinates for beam wander. The use of Cartesian coordinates is required for reasons important to the new modelling approach proposed in this work. As an aside, the effects of scintillation may be incorporated into this beam wander induced fading model by treating I_0 as a random variable representing scintillation [122, 123].

The Probability Distribution Function (PDF) of the received intensity, I, due to beam wander, as measured at the centre of the long-term beam is given by

$$p(I) = \gamma I^{\gamma - 1} \quad \text{where} \quad 0 \leq I \leq 1, \tag{6.7}$$

where γ is a parameter related to the ratio of beam wander displacement and the receiver size [124].

While these expressions are extremely useful, they are limited by a lack of temporal information about the evolution of the beam wander: there is no correlation from one moment to the next as r_c is simply a normal random variable. Consequently, while it is indeed possible to determine the overall percentage of time a link may be in deep fade, for instance, it is impossible to accurately determine the average duration of the deep fades. This information is required to inform the design of optimised Forward Error Correction (FEC) code rates and lengths, interleaving depth and other techniques used to make a link more robust to atmospheric turbulence and in its absence results in over- or under-engineered systems based on potentially incorrect assumptions.

6.2 Methods

6.2.1 Experimental Setup

Empirical measurements of beam wander were performed on a $L = 150$ m horizontal outdoor link that was built at the CSIR in Pretoria, South Africa, which is at an altitude of 1.4 km. The link was approximately 5 m above the ground and used a 635 nm collimated laser beam with a diameter of approximately $\omega_0 = 7$ mm at the transmit aperture. A simplified diagram of the setup is shown in Fig. 6.1 (a). The transmitted and received laser beams were expanded and reduced by a telescope and imaged onto a high speed camera at the Fourier plane. The received beam was measured by a camera to resolve the spatial movement of the beam over approximately ten seconds.

The frame rate of the camera is an important parameter in this experiment as the movement of the beam must be recorded without loss of information. The Greenwood frequency, f_G, is a measure of the rate at which turbulence affects a beam and is easily calculated given the wind speed and atmospheric coherence length, r_0, as $f_G = 0.43(V/r_0)$ in Hertz [77]. The weather at the time of measurement was clear, 28 °C with an average wind speed of $V = 10$ km/h with gusts of up to $V = 12$ km/h. With preliminary measurements of

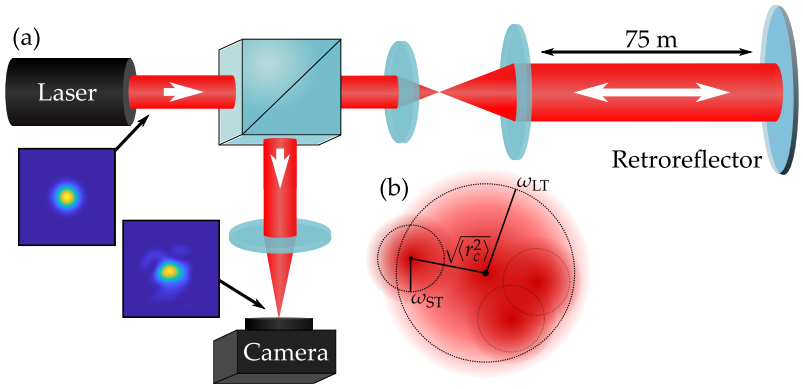


Figure 6.1: (a) Simplified schematic diagram of the experimental setup with insets of the beam intensity at the transmitter and receiver. (b) A diagram that illustrates the relationship between short- and long-term beam wander parameters.

r_0 and assuming a constant but worst-case wind speed over the the course of a measurement, the Greenwood frequency was approximately $f_G = 130$ Hz. The camera frame rate was therefore conservatively set at 300 Frames Per Second (FPS) to capture the movement of the beam without loss of temporal information.

The position of the beam in each frame is found using the weighted centroid and stored as separate time series of x and y coordinates. Since the atmosphere is isotropic and the axes are orthogonal and thus independent, we restrict analysis to a single axis for convenience. When both axes are required for simulation of the resulting beam wander model, we simply run two models independently.

6.2.2 ARMA-based Memory Model

There are several classes of model that are suitable for correlated time series, depending on the characteristics of the signal [125–127]. For stationary signals such as beam wander a so-called ARIMA (Auto-Regressive Integrated Moving Average) model is elegantly suitable, as evidenced by the results presented in Sec. 6.3, and can be fit using the Box-Jenkins method [125]. Auto-Correlation and Partial Auto-Correlation Functions (ACFs and PACFs) are used to approximately determine the order and suitability of the various model parameters, but ultimately the model fits performed using least-squares regression are verified by minimising the Akaike Information Criterion (AIC) and Bayesian Information Criterion (BIC).

A long term trend in the data is not expected, since a constant turbulence strength is assumed over the short duration of the measurements. Consequently, an ARMA(p,q) model can be used without any Integral terms, where in general the position of the current sample is given by

$$\beta_{x,t} = c + \sum_{i=1}^{p} M_i \beta_{x,t-i} + \sum_{j=1}^{q} N_j \epsilon_{t-j} + \epsilon_t, \tag{6.8}$$

where c is a constant mean term, p is the order of the auto-regressive series, q is the order of the moving average series and M_i and N_j are the model factors of their respective series. Randomness is introduced to the model by the addition of ϵ_t which is zero mean Gaussian white noise with a suitable variance, σ^2.

As Eq. 6.8 is directly modelling the position of the beam at a specific time, $\beta_{x,t}$, we are conveniently able to map this to a receive intensity using Eqs. 6.5 and 6.6. The required $\beta_{y,t}$ values are found using an identical but independent model since the atmosphere is isotropic.

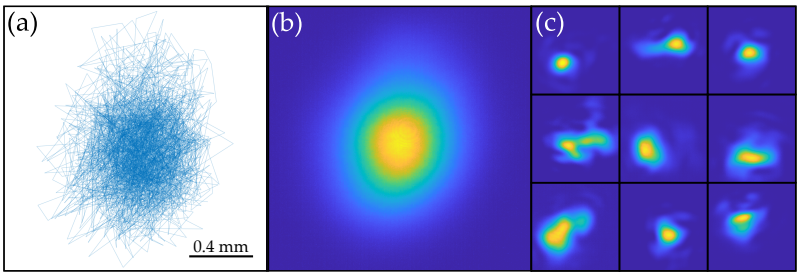


Figure 6.2: Experimental measurements of the beam wander showing a plot of the centroid position in (a), the long-term beam in (b) and sample short term beam images in (c).

Table 6.1: Weights for the ARMA(2,2) model. As expected, the constant term is zero.

c	M_1	M_2	N_1	N_2	σ^2
0	1.759	-0.7626	-1.289	0.3166	2150

6.3 Fitting the Memory Model

To demonstrate the feasibility, effectiveness and advantages of the proposed modelling approach, we present a model for the link described in Sec. 6.2.1 under moderate-to-strong turbulence conditions where deep fading is more likely than in weak turbulence.

The turbulence parameters at the time of measurement are as follows, with images of the long- and short-term beams as well as the path that the short term beam took over the 10 s measurement window shown in Fig. 6.2. The average refractive index structure constant $C_n^2 = 4.1 \times 10^{-13}$, the atmospheric coherence length $r_0 = 0.01$ m and the scintillation index is $\sigma_I = 0.55$, indicating that the link is in the weak to moderate turbulence regime.

One thousand samples of the change in centroid position over time, focusing on $\beta_{x,t}$, are shown in Fig. 6.3 (a). Note that while we refer to discrete samples of t, the sample period is in fact 3.3 ms. The hypothesised temporal correlation between subsequent samples is made clear by simply plotting $\beta_{x,t}$ against the previous position, $\beta_{x,t-1}$, shown in Fig. 6.3 (b). It is clear that there is a correlation with sample $t-1$ and also a correlation at sample $t-3$, however, at a lag of $t-10$ there is no obvious correlation. The ACF and PACFs of the beam position are a more rigorous measure for this and are shown in Fig. 6.3 (c). Clearly, a strong correlation exists for multiple samples and hence several milli-seconds. We can use this observation to build a model of the beam wander that is not simply a random walk as historically assumed, but rather a time series with temporal structure.

It was found that $\beta_{x,t}$ (and by nature $\beta_{y,t}$) is well modelled by an ARMA(2,2) process with the model factors shown in Tab. 6.1, which were found using a least squares regression on the approximately 3000 measurement samples. The order of the model was verified by testing orders from zero to twenty and simultaneously minimising the AIC and BIC criterion's, as per Sec. 6.2.2. Another test of the resulting model is given by the statistics of the residuals, which should resemble random noise. Some of the residual statistics are visualised in Fig. 6.4. It is clear from the figure that there is no correlation between subsequent residual samples and a histogram of the residual values has a Gaussian shape, implying that the residuals are Gaussian white noise. The proposed ARMA(2,2) model is an excellent fit of the measured data in a theoretical sense, but is it a good fit in the physical sense and how can we use it to our advantage?

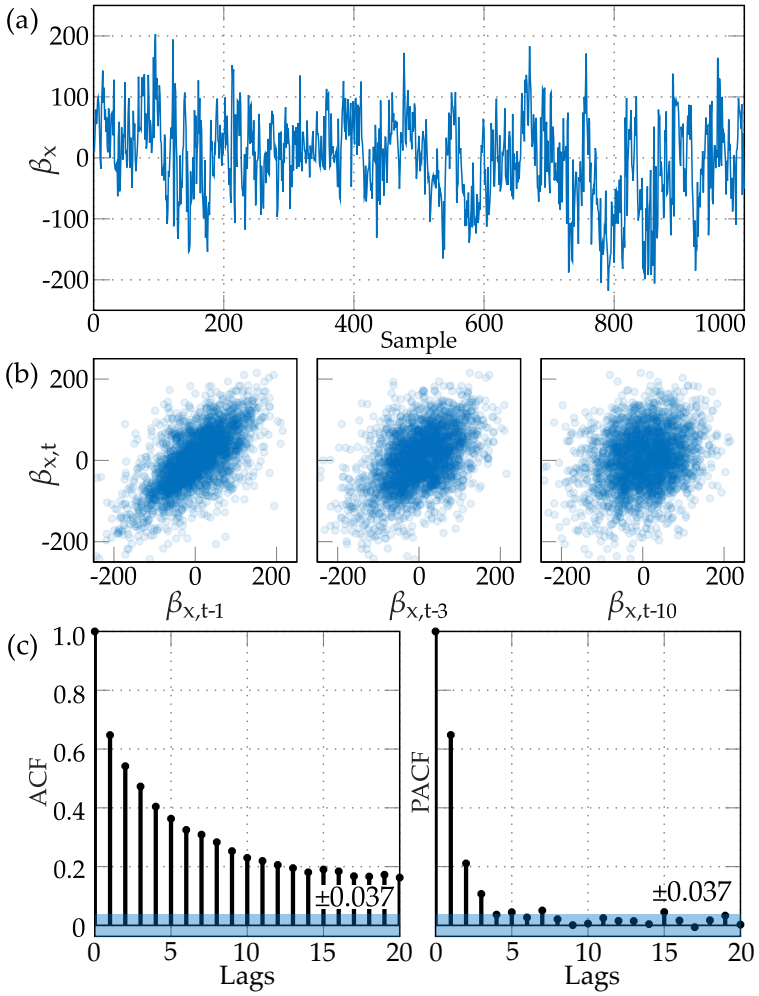


Figure 6.3: (a) A short sample of the beam wander in x. (b) Scatter plots showing temporal correlation between samples at $t-1$, some correlation at $t-3$ but no correlation at $t-10$. (c) Auto-correlation and partial auto-correlation plots of the data with the 95% significance region shaded (± 0.037).

6.4 Modelling Beam-Wander Induced Fading

In order to verify this new model, and hence this new approach, we must show that it is able to reproduce the results of existing models for beam wander. For a fair statistical comparison to the experimental data, the same number of samples of the ARMA(2,2) model presented in Sec. 6.3 are generated as the number of experimental data samples. Plots of the results in this section are shown in Fig. 6.5.

As discussed in Sec. 6.1, it is possible to calculate a simulated long-term intensity by summing the short-term beams over all of the simulated position samples. The resulting long term intensity distribution should have a Gaussian shape with a radial variance that matches that of the experimental data. The radial variance of the measured data gives $\langle r_c^2 \rangle = 4.31 \times 10^{-4}$ and for the simulated data $\langle r_c^2 \rangle = 4.26 \times 10^{-4}$. According to theory in Eq. 6.3 for the estimated C_n^2 of the experiment, $\langle r_c^2 \rangle = 7.10 \times 10^{-4}$. The simulated and measured beam wander radial variances are very similar whereas the theory value is in the same order of magnitude but slightly different. This is due to the fact that the theory used does not take outer-scale effects into account because the outer scale was not measured.

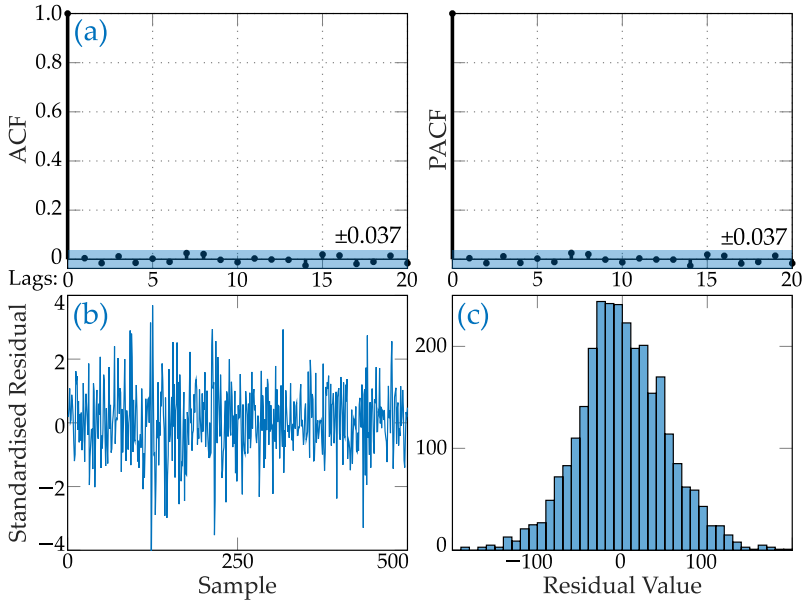


Figure 6.4: Plots to show that the residuals of the model and the measured samples are white Gaussian noise. (a) The ACF and PACF indicate no correlations. (b) A short sample of the standardised residuals showing no visible pattern. (c) The histogram of the residuals has a random Gaussian characteristic shape.

In addition to the long term intensity, by applying Eq. 6.5 to the simulated and measured data, a comparison between the fading PDFs of the two data sets can be made. For a valid model, the shape of the simulated PDF must be similar to that of the measured data. Upon examination of Fig. 6.5, we see that this is indeed the case. It is clear that this new approach results in models that accurately reduce to existing models for beam wander, however, their real benefit is the ability to model the channels memory.

6.5 Modelling Memory and Deep Fading

As discussed in the introduction and Sec. 6.1, an important property in the design of a FSO link with memory is the average length of time the received intensity spends above or below a certain threshold. If the threshold is set to a low value that represents a deep fade for example, one can estimate the expected average duration of a deep fade and optimally design the system. This complements the conventional metric that is the expected probability that the link will be in deep fade, which is typically used to calculate channel capacity.

Rather than referring to the length of time on either side of a threshold in seconds, for example, we instead refer to the so-called "transition run length" which is the number of consecutive samples on either side of the threshold. If required, this can be converted to time by multiplying by the sample period. This terminology is typically used for memory channels, for instance those described by Gilbert-Elliot Markov processes [113].

A Run Length Distribution (RLD) is a histogram of the number of occurrences of a certain transition run length above or below the specified threshold. Logically, with more data, longer transition run lengths (which have correspondingly lower probabilities) will begin to appear. For this reason, we can only compare data sets with the same number of samples. Due to the limited number of experimental samples available, we set the transition threshold to the mean intensity value for illustrative purposes.

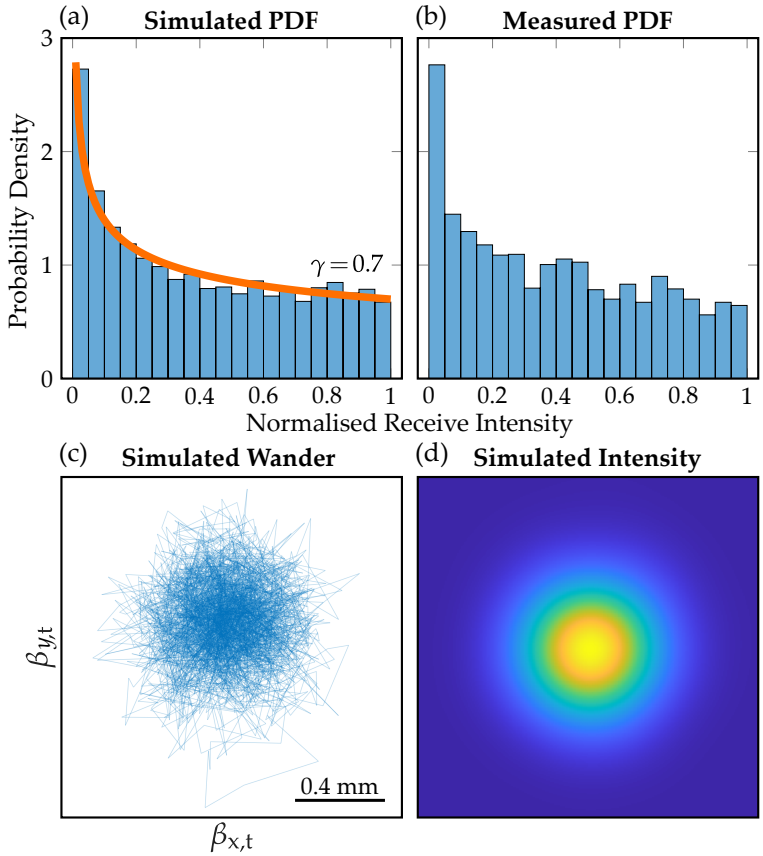


Figure 6.5: Plots to demonstrate the fading statistics of the model in comparison to experimental data. (a) and (b) are PDFs of simulated and measured intensities with an overlay (orange) of the theoretical PDF showing excellent agreement with existing theory. (c) Simulated beam wander positions with the resulting long-term intensity in (d).

Figure 6.6 shows run length distribution plots for the ARMA simulated and experimentally measured beam wander induced fading data. The simulated data matches the experimental data well. Superimposed on the figure is a run length distribution plot for simulated data based on the conventional PDF-based model for beam wander (see Eq. 6.7 with $\gamma = 0.7$, which is shown in Fig. 6.5). The run length distribution of the conventional PDF-based model drops off steeply and is clearly not a match for the experimental data.

Run lengths of longer than eight consecutive samples above or below the threshold are rare when using the existing PDF model when using only 3000 samples. Obviously, if a larger number of random samples were generated, longer run lengths would be measured, but this would also be the case with more experimental data. In comparison with the measured data, longer run lengths of up to 15 consecutive samples are present even in a small data set.

This is a clear deficiency of a PDF-based model: it is unlikely that any PDF which simultaneously matches both the PDF of the received intensity and of the run length distribution can be found. In contrast, the model produced by the approach proposed in this work accurately matches both the measured run length distribution as well as the fading distribution with only a marginal increase in complexity.

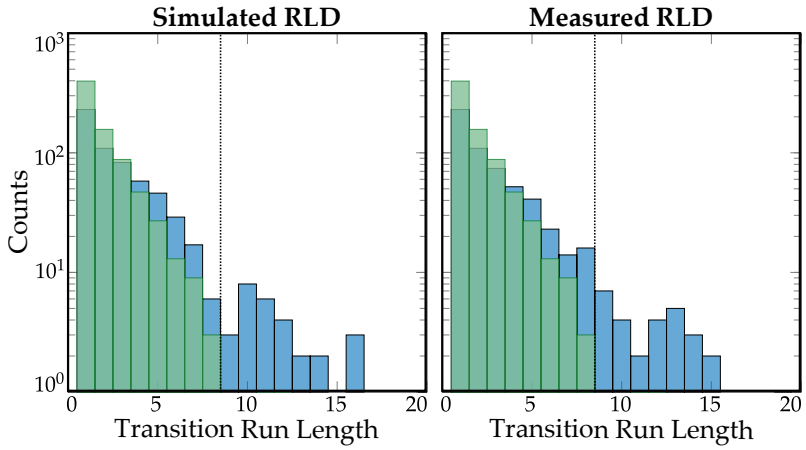


Figure 6.6: Run length distribution plots of the simulated ARMA model and the experimental measurements with a transition threshold set at 50% intensity for illustrative purposes. Overlaid on the plots in green is the run length distribution of data simulated using the conventional PDF-based model which clearly does not match the experimental measurements.

6.6 Modelling Mode Crosstalk

The proposed model has further utility than modelling received intensity fluctuations and their memory. Reliable and high speed long distance MDM systems are extremely challenging because of crosstalk issues. The computational complexity of strong error correction codes and MIMO is prohibitive at link speeds requiring the use of MDM in the first place. One of the dominant causes of crosstalk error in MDM systems is lateral displacement and tip / tilt at the receiver [35, 128, 129]. Alternatively, in modal diversity systems, modal crosstalk may be advantageous, in a sense, and can be used to design longer distance or more robust FSO systems [47, 130, 131]. Using the modelling approach in this paper it becomes possible to simulate and even predict the temporal evolution of mode crosstalk due to lateral displacement and hence facilitate the creation of optimised (and possibly less computationally intensive) schemes to correct errors due to crosstalk in both MDM and modal diversity.

Here we briefly demonstrate this concept using Laguerre-Gaussian (LG) mode crosstalk. A transmitted LG mode with $\ell = 0$, which is a standard Gaussian, will result in a spectrum of detected OAM modes at the receiver. Similarly, a transmitted higher-order mode in the presence of lateral displacement would result in a different spectrum of received modes.

This is often thought of simply as misalignment, where it is a challenge to efficiently couple the received light into a single mode optical fibre. In essence, it is for this reason that the use of few- or even multi-mode fibres (which can accept neighbouring OAM modes) has been demonstrated to be advantageous, especially when combined with digital signal processing [131]. A knowledge of the expected number of modes in this system could inform the choice of few-mode fibre.

The detected OAM spectrum due to a lateral displacement of $r_{c,t}$ at a time t is given by [128]

$$C_\ell = \exp\left(-\frac{r_{c,t}^2}{\omega_{\mathrm{ST}}^2}\right) I_{|\ell|}\left(\frac{r_{c,t}^2}{\omega_{\mathrm{ST}}^2}\right) \tag{6.9}$$

where C_ℓ is the weight for the ℓth mode and $I_n(x)$ is the nth-order modified Bessel function of the first kind. Figure 6.7 shows a sample of consecutive OAM crosstalk calculations from the simulated beam wander. Since we have shown a temporal correlation between beam wander positions, there will also be a similar temporal correlation between mode crosstalk

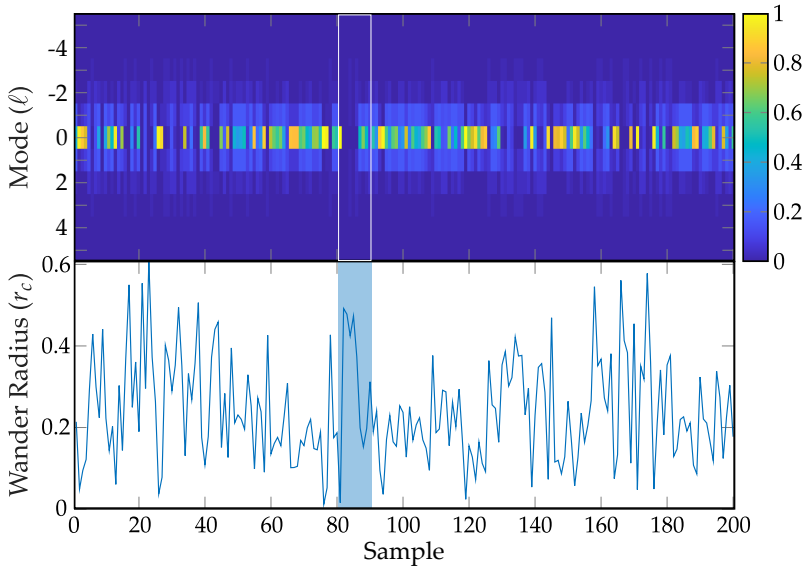


Figure 6.7: (Top) Mode crosstalk from the transmitted Gaussian mode ($\ell = 0$) into OAM modes $\ell = -5$ to 5 due to lateral displacement over time. (Bottom) The corresponding normalised beam wander radii, r_c. The highlighted section shows good examples of crosstalk with well aligned (minimal crosstalk) and misaligned (high crosstalk) cases.

spectrums. This may be harnessed in a predictive manner to implement more efficient signal processing strategies for MDM or modal diversity.

6.7 Conclusion

We have experimentally shown that turbulence induced beam wander has significant temporal correlation that is not predicted by existing models for atmospheric turbulence. In addition, using the run-length distributions for the intensity of the received beam, we show that there is a significant difference in what is expected according to conventional probabilistic models for beam wander and reality. These differences can be explained by considering turbulence induced beam wander - and perhaps the mechanisms for turbulence itself - as a high-order memory system, as opposed to the conventional memoryless or first-order frozen-turbulence assumptions as visible in other works.

We have developed a new approach for modelling turbulence-induced beam wander and tested the approach on a model for a 150 m experimental link in weak-to-moderate turbulence. The resulting models are able to accurately reproduce the effects of memory in the atmospheric turbulence channel, where there is a temporal correlation in the movement of the beam. In addition to accurately modelling the received intensity distribution as well as the temporal evolution of the received intensity, we briefly show how the model may be used to simulate the evolution of crosstalk in MDM systems using OAM as an example. Our model will enable the development of optimised signal processing and error correction coding techniques for free-space optical communications which were not previously possible, for instance, interleaving. Models based on this new approach will inform the depth of the required interleaving code for mitigating beam wander induced errors.

CHAPTER 7

Conclusion

Every day the demand for fast, low latency internet connectivity increases. The demand for data globally has been increasing exponentially, with annual growth rates between 30% and 90% since the advent of the Internet. This incredible growth was initially supported by fibre-optic back-haul and dial-up modems. Eventually, consumers moved from dial-up to ADSL. Personal WiFi networks became pervasive and connectivity requirements increased further, resulting in the demand for even faster Internet. Many people now have their own personal fibre connection to their homes that is faster than the undersea cables of the 1990's. One cannot forget smart phones - with 3G technology data became a commodity and the ability to browse the Internet on demand, anywhere, drove the deployment of 4G which provided lower latencies and faster data rates. Deployment of 5G is now imminent, promising one hundred times faster data-rates to consumers - but can the network sustain such high aggregate bandwidths?

Fibre optic interfaces are extremely fast, and in laboratory experiments they have been demonstrated to sustain bandwidths of over one terabit per second per wavelength. Conceivably, this is sufficient even for massive 5G connectivity - but what about in developing countries where major cities are fed via old terrestrial microwave and satellite links that can only sustain gigabits per second? Huge geographical distances in Africa, for example, make it prohibitively expensive for inter-city optical fibre to be widely deployed in the short term.

Free Space Optical (FSO) communication is a possible solution to this issue. Not only can FSO be used for the relatively short distances between cell towers (where line of site permits) thus avoiding the need to trench, but if their range can be improved, they may form part of a retrofit interim solution for long-haul terrestrial infrastructure. Current commercial FSO solutions can sustain bandwidths of several gigabits per second over distances on the order of 2 km. In laboratory experiments, massive data-rates (hundreds of gigabits to just over one petabit per second) have been demonstrated over several meters. Military FSO systems have been demonstrated to sustain hundreds of megabits per second over approximately 100 km. A clear gap is gigabits per second over tens of kilometres. This thesis makes several contributions to the field in order to try bridge this gap in the hope that one day the so-called "digital divide" may be bridged too.

One of the dominant, unsolved issues with FSO is the effect of atmospheric turbulence. Broadly speaking, the resulting effect of turbulence is a degradation in the Signal to Noise Ratio (SNR), limiting the possible data rates of a system. Strong Forward Error Correction (FEC) could be coupled with signal processing techniques such as Multiple Input Multiple Output (MIMO) which can harness channel diversity to increase the resilience of a link,

however, this is predominantly a subject for future investigation.

This work is focused on "passive" optical techniques to improve the resilience, and hence the range, of FSO links at a more fundamental level through the use of higher order spatial modes, before the addition of digital techniques. Three pertinent answers to the question "How can spatial modes of light be used to improve the resilience of laser-based free-space optical communication to atmospheric turbulence?" have been published over the duration of this work and have been described in detail in this thesis. Finally, a memory model for beam wander is proposed in an attempt to describe the nature of the effects observed in the previous contributions. In addition, this model can be used to describe the "burstiness" of the FSO channel. The bursty nature of the FSO channel has not been previously modelled, but it is in fact one of the primary reasons why reliable communications and conventional digital processing schemes do not work as expected.

Atmospheric turbulence predominantly manifests as angle of arrival fluctuations (tip/tilt) and thus wandering of a FSO laser beam, resulting in fading (or Mode Dependent Loss (MDL)) as well as mode-crosstalk. Given the complex phase structure of Laguerre-Gauss (LG) and Hermite-Gauss (HG) modes, it was unknown whether the higher order effects of turbulence would overcome the known beam wander resilience of HG modes over LG modes. In Chapter 3 we experimentally show that carefully chosen HG and binary HG modes are significantly more resilient to single phase screen Kolmogorov turbulence than LG beams with the same beam propagation factor (M^2). Lower crosstalk results in higher capacity mode division multiplexed systems, but more importantly, the lower MDL experienced by HG modes over LG modes means that they should theoretically be able to propagate significantly further. At a MDL of 50%, we show a 167% increase in theoretical range of non-symmetric HG modes over similar order LG modes. [35]

While both scalar and vector vortex modes have been used as transmission bases for FSO systems, it had been suggested that the latter is more robust in turbulence. In Chapter 4, using orbital angular momentum modes as an example, we demonstrate theoretically and experimentally that the crosstalk due to turbulence is in fact the same in the scalar and vector basis sets of such modes. This result brings new insights about the behaviour of vector and scalar modes in turbulence, but more importantly it demonstrates that when considering optimal modes for MDM, the choice should not necessarily be based on their vectorial nature. [40]

One of the most common solutions to overcome channel fading is to exploit diversity. Diversity (or more commonly MIMO) is common in radio-based systems such as WiFi but it is less common in FSO systems. In this approach, information is sent in parallel over different paths using two or more transmitters or receivers that are spatially separated. Provided the separation is sufficient (greater than r_0 meters), each beam experiences independent atmospheric turbulence which lowers the probability of a receive error. In Chapter 5 we propose and experimentally demonstrate a new method of diversity based on spatial modes of light, which we call modal diversity. The need for a physical separation of the transmitters is removed by exploiting the fact that spatial modes of light experience different perturbations, even when travelling along the same path, as evidenced by Chapter 3. For this proof-of-principle, identical radius modes from the HG and LG basis sets were chosen. A relative improvement in Bit Error Rate (BER) of up to 54% was measured without increasing the total transmit power or the receive aperture radius. This finding can be used to significantly improve future FSO communication links in terms of range and reliability, without adding additional (expensive) apertures. [47]

A further implication of the use of different modal bases in a single system is that the co-propagating modes may experience a lower degree of crosstalk than neighbouring adjacent modes within a single basis. This hypothesis should be tested in future, but this may indeed have interesting consequences and provide significant benefits to Mode Division Multiplexing (MDM) or when MIMO signal processing is used. We speculate that it should be possible to formalise the concept of "separate" in terms of a newly defined but as-yet

hypothetical modal distance, akin to the previous definition in terms of a physical separation, r_0.

In both the HG versus LG, as well as the modal diversity contributions above, the most likely underlying physical mechanism that best describes the observed differences is beam wander. Existing models for beam wander make use of memoryless probability distributions and long term averages. These models are not able to accurately model time-dependent intensity fluctuations which sometimes result in deep fading, where the received intensity is too low to maintain reliable communication for an extended period of time. In Chapter 6, an elegant new memory model is presented which models the behaviour of beam wander and therefore also beam wander induced intensity fluctuations with the unique capability to accurately simulate deep fading in a bursty manner. This is invaluable for the development of optimised burst error correction coding and digital signal processing in order to improve the throughput and reliability of FSO systems. In addition, since the positions of the beam are modelled, it is possible to calculate the expected crosstalk due to misalignment in MDM systems for any modal basis including LG and HG beams.

The work presented provides answers to some pertinent questions in line with increasing the range of FSO communication systems. While no actual communication system was built and tested, the contributions within this thesis will enable better design decisions by providing a guideline to the choice of modes and the use of diversity, both modal and conventional. A 300 m physical link is in the process of being built and is the subject of future work. More accurate simulations of a system are now possible through the use of the proposed memory model approach for turbulence induced beam wander. This enables the design of crosstalk mitigation schemes if MDM is required (in high capacity systems), or potentially lower computational complexity decoders for diversity. Lower computational complexity is critical in high capacity systems but also in cost effective systems where more processing power is usually associated with higher cost. The use of modal diversity allows for a more compact system with a single transmit or receive aperture, also reducing cost. The ability to keep costs to a minimum is crucial in a technology that is to be deployed on a massive scale, for example in bridging the digital divide in Africa.

Future avenues for research in the digital domain would be the development of optimised burst error correction codes and signal processing techniques. The new knowledge that the FSO channel is in fact a memory channel opens many exciting opportunities in this domain. In terms of atmospheric optics, more work must be done to precisely characterise the extent and possibilities of modal diversity. An analytical model that allows for the calculation of a so-called modal distance, akin to the atmospheric coherence length, would be a high impact contribution to the field both for diversity but also for MDM in general. Finally, there are some information theoretical papers that suggest that high order modes cannot be used to increase the capacity of a system [6]. In opposition to existing experimental demonstrations, these papers degrade confidence in this exciting, emerging field. The common assumption that LG modes, which have been well studied, are identical to HG modes, is incorrect as we have shown in Chapter 3 and as such, it will be interesting to see if the aforementioned information theoretical papers can be refined. The consequences of this is as yet unknown, but would be an excellent avenue for further research.

References

[1] P. J. Winzer, "Making spatial multiplexing a reality," *Nature Photonics*, vol. 8, no. 5, pp. 345–348, Apr. 2014.

[2] P. J. Winzer, D. T. Neilson, and A. R. Chraplyvy, "Fiber-optic transmission and networking: the previous 20 and the next 20 years [Invited]," *Optics Express*, vol. 26, no. 18, p. 24 190, Sep. 2018.

[3] M. P. J. Lavery, M. M. Abadi, R. Bauer, G. Brambilla, L. Cheng, M. A. Cox, A. Dudley, A. D. Ellis, N. K. Fontaine, A. E. Kelly, C. Marquardt, S. Matlhane, B. Ndagano, F. Petruccione, R. Slavík, F. Romanato, C. Rosales-Guzmán, F. S. Roux, K. Roux, J. Wang, and A. Forbes, "Tackling Africa's digital divide," *Nature Photonics*, vol. 12, no. 5, pp. 249–252, May 2018.

[4] SpaceX, *Starlink*. [Online]. Available: `www.starlink.com`.

[5] M. A. Khalighi and M. Uysal, "Survey on Free Space Optical Communication: A Communication Theory Perspective," *IEEE Communications Surveys & Tutorials*, vol. 16, no. 4, pp. 2231–2258, Jan. 2014.

[6] N. Zhao, X. Li, G. Li, and J. M. Kahn, "Capacity limits of spatially multiplexed free-space communication," *Nature Photonics*, vol. 9, no. 12, pp. 822–826, Nov. 2015.

[7] International Telecommunication Union - ITU-T, "G.694.1 (06/2002), Spectral grids for WDM applications: DWDM frequency grid," *Series G.694.1*, p. 14, 2002.

[8] G. Gibson II, J. Courtial, M. Vasnetsov, S. Barnett, S. Franke-Arnold, and M. Padgett, "Increasing the data density of free-space optical communications using orbital angular momentum," in *Free-Space Laser Communications IV*, J. C. Ricklin and D. G. Voelz, Eds., International Society for Optics and Photonics, Oct. 2004, p. 367.

[9] J. A. Anguita, M. A. Neifeld, and B. V. Vasic, "Turbulence-induced channel crosstalk in an orbital angular momentum-multiplexed free-space optical link," *Applied Optics*, vol. 47, no. 13, p. 2414, May 2008.

[10] J. Wang, "Advances in communications using optical vortices," *Photonics Research*, vol. 4, no. 5, B14, Oct. 2016.

[11] A. E. Willner, Y. Ren, G. Xie, Y. Yan, L. Li, Z. Zhao, J. Wang, M. Tur, A. F. Molisch, and S. Ashrafi, "Recent advances in high-capacity free-space optical and radio-frequency communications using orbital angular momentum multiplexing," *Philosophical Transactions of the Royal Society of London A: Mathematical, Physical and Engineering Sciences*, vol. 375, no. 2087, 2017.

[12] A. Trichili, C. Rosales-Guzmán, A. Dudley, B. Ndagano, A. Ben Salem, M. Zghal, and A. Forbes, "Optical communication beyond orbital angular momentum," vol. 6, p. 27 674, Jun. 2016.

[13] M. Chen, K. Dholakia, and M. Mazilu, "Is there an optimal basis to maximise optical information transfer?" *Scientific reports*, vol. 6, p. 22 821, Mar. 2016.

[14] G. Gibson, J. Courtial, M. J. Padgett, M. Vasnetsov, V. Pas'ko, S. M. Barnett, and S. Franke-Arnold, "Free-space information transfer using light beams carrying orbital angular momentum," EN, *Optics Express*, vol. 12, no. 22, p. 5448, Nov. 2004.

[15] M. Krenn, R. Fickler, M. Fink, J. Handsteiner, M. Malik, T. Scheidl, R. Ursin, and A. Zeilinger, "Communication with spatially modulated light through turbulent air across Vienna," *New Journal of Physics*, vol. 16, no. 11, p. 113 028, Nov. 2014.

[16] A. E. Willner, H. Huang, Y. Yan, Y. Ren, N. Ahmed, G. Xie, C. Bao, L. Li, Y. Cao, Z. Zhao, J. Wang, M. P. J. Lavery, M. Tur, S. Ramachandran, A. F. Molisch, N. Ashrafi, and S. Ashrafi, "Optical communications using orbital angular momentum beams," *Advances in Optics and Photonics*, vol. 7, no. 1, p. 66, 2015.

[17] J. Wang, J.-Y. Yang, I. M. Fazal, N. Ahmed, Y. Yan, H. Huang, Y. Ren, Y. Yue, S. Dolinar, M. Tur, and A. E. Willner, "Terabit free-space data transmission employing orbital angular momentum multiplexing," *Nature Photonics*, vol. 6, no. 7, p. 488, 2012.

[18] G. Funes, M. Vial, and J. A. Anguita, "Orbital-angular-momentum crosstalk and temporal fading in a terrestrial laser link using single-mode fiber coupling," EN, *Optics express*, vol. 23, no. 18, pp. 23 133–42, Sep. 2015.

[19] R. Brüning, B. Ndagano, and M. Mclaren, "Data transmission with twisted light through a free-space to fiber optical communication link," *Journal of Optics*, vol. 18, no. 3, 03LT01, 2016.

[20] M. P. J. Lavery, C. Peuntinger, K. Günthner, P. Banzer, D. Elser, R. W. Boyd, M. J. Padgett, C. Marquardt, and G. Leuchs, "Free-space propagation of high-dimensional structured optical fields in an urban environment," *Science Advances*, vol. 3, no. 10, e1700552, Oct. 2017.

[21] M. Krenn, J. Handsteiner, M. Fink, R. Fickler, R. Ursin, M. Malik, and A. Zeilinger, "Twisted light transmission over 143 km," *Proceedings of the National Academy of Sciences of the United States of America*, vol. 113, no. 48, pp. 13 648–13 653, Nov. 2016.

[22] Y. Zhao, J. Liu, J. Du, S. Li, Y. Luo, A. Wang, L. Zhu, and J. Wang, "Experimental Demonstration of 260-meter Security Free-Space Optical Data Transmission Using 16-QAM Carrying Orbital Angular Momentum (OAM) Beams Multiplexing," in *Optical Fiber Communication Conference*, Washington, D.C.: OSA, Mar. 2016, Th1H.3.

[23] Y. Ren, Z. Wang, P. Liao, L. Li, G. Xie, H. Huang, Z. Zhao, Y. Yan, N. Ahmed, A. Willner, M. P. J. Lavery, N. Ashrafi, S. Ashrafi, R. Bock, M. Tur, I. B. Djordjevic, M. A. Neifeld, and A. E. Willner, "Experimental characterization of a 400 Gbit/s orbital angular momentum multiplexed free-space optical link over 120 m," EN, *Optics Letters*, vol. 41, no. 3, p. 622, Jan. 2016.

[24] J. A. Anguita, M. A. Neifeld, and B. V. Vasic, "Turbulence-induced channel crosstalk in an orbital angular momentum-multiplexed free-space optical link," *Applied Optics*, vol. 47, no. 13, p. 2414, 2008.

[25] L. H.-C. Pu Ji-Xiong Wang Tao and L. Cheng-Liang, "Propagation of cylindrical vector beams in a turbulent atmosphere," *Chinese Physics B*, vol. 19, p. 89 201, 2010.

[26] R. Chen, Y. Dong, F. Wang, and Y. Cai, "Statistical properties of a cylindrical vector partially coherent beam in turbulent atmosphere," *Applied Physics B*, vol. 112, no. 2, pp. 247–259, Apr. 2013.

[27] C. Chen, H. Yang, S. Tong, and Y. Lou, "Changes in orbital-angular-momentum modes of a propagated vortex Gaussian beam through weak-to-strong atmospheric turbulence," EN, *Optics Express*, vol. 24, no. 7, p. 6959, Mar. 2016.

[28] C. Kamwangala, M. A. Cox, and L. Cheng, "Transmitter power control for a multicarrier visible light communication system," *Transactions on Emerging Telecommunications Technologies*, e3453, Jun. 2018.

[29] S. M. Haas, J. H. Shapiro, and V. Tarokh, "Space-time codes for wireless optical communications," *EURASIP Journal on Applied Signal Processing*, vol. 2002, no. 1, pp. 211–220, 2002.

[30] J. A. Anguita and J. E. Cisternas, "Experimental evaluation of transmitter and receiver diversity in a terrestrial FSO link," in *2010 IEEE Globecom Workshops*, IEEE, Dec. 2010, pp. 1005–1009.

[31] S. Navidpour, M. Uysal, and M. Kavehrad, "BER Performance of Free-Space Optical Transmission with Spatial Diversity," *IEEE Transactions on Wireless Communications*, vol. 6, no. 8, pp. 2813–2819, Aug. 2007.

[32] M. Andersson, E. Berglind, and G. Björk, "Orbital angular momentum modes do not increase the channel capacity in communication links," *New Journal of Physics*, vol. 17, no. 4, p. 043 040, Apr. 2015.

[33] N. Zhao, X. Li, G. Li, and J. M. Kahn, "Capacity limits of spatially multiplexed free-space communication," *Nature Photonics*, vol. 9, no. 12, p. 822, 2015.

[34] X. Gu, L. Chen, and M. Krenn, "Phenomenology of complex structured light in turbulent air," *ArXiv*, p. 1906.03581v1, 2019.

[35] M. A. Cox, L. Maqondo, R. Kara, G. Milione, L. Cheng, and A. Forbes, "The Resilience of Hermite- and Laguerre-Gaussian Modes in Turbulence," *Journal of Lightwave Technology*, vol. 37, no. 16, pp. 3911–3917, Aug. 2019.

[36] B. Ndagano, B. Perez-Garcia, F. S. Roux, M. McLaren, C. Rosales-Guzman, Y. Zhang, O. Mouane, R. I. Hernandez-Aranda, T. Konrad, and A. Forbes, "Characterizing quantum channels with non-separable states of classical light," *Nature Physics*, vol. 13, no. 4, pp. 397–402, 2017.

[37] W. Cheng, J. W. Haus, and Q. Zhan, "Propagation of scalar and vector vortex beams through turbulent atmosphere," in *SPIE LASE: Lasers and Applications in Science and Engineering*, O. Korotkova, Ed., International Society for Optics and Photonics, Feb. 2009, pp. 720 004–720 004.

[38] V. P. Aksenov, V V Kolosov, G. A. Filimonov, and C. E. Pogutsa, "Orbital angular momentum of a laser beam in a turbulent medium: preservation of the average value and variance of fluctuations," *Journal of Optics*, vol. 18, no. 5, p. 054 013, May 2016.

[39] N. Mphuthi, R. Botha, and A. Forbes, "Are Bessel beams resilient to aberrations and turbulence?" *Journal of the Optical Society of America A*, vol. 35, no. 6, p. 1021, Jun. 2018.

[40] M. A. Cox, C. Rosales-Guzmán, M. P. J. Lavery, D. J. Versfeld, and A. Forbes, "On the resilience of scalar and vector vortex modes in turbulence," *Optics Express*, vol. 24, no. 16, p. 18 105, Aug. 2016.

[41] Y. Gu, O. Korotkova, and G. Gbur, "Scintillation of nonuniformly polarized beams in atmospheric turbulence," EN, *Optics Letters*, vol. 34, no. 15, p. 2261, Jul. 2009.

[42] S. Restuccia, D. Giovannini, G. Gibson, and M. Padgett, "Comparing the information capacity of Laguerre–Gaussian and Hermite–Gaussian modal sets in a finite-aperture system," *Optics Express*, vol. 24, no. 24, p. 27 127, Nov. 2016.

[43] G. Xie, L. Li, Y. Ren, H. Huang, Y. Yan, N. Ahmed, Z. Zhao, M. P. J. Lavery, N. Ashrafi, S. Ashrafi, R. Bock, M. Tur, A. F. Molisch, and A. E. Willner, "Performance metrics and design considerations for a free-space optical orbital-angular-momentum multiplexed communication link," *Optica*, vol. 2, no. 4, p. 357, Apr. 2015.

[44] K. Pang, H. Song, Z. Zhao, R. Zhang, H. Song, G. Xie, L. Li, C. Liu, J. Du, A. F. Molisch, M. Tur, and A. E. Willner, "400-Gbit/s QPSK free-space optical communication link based on four-fold multiplexing of Hermite–Gaussian or Laguerre–Gaussian modes by varying both modal indices," *Optics Letters*, vol. 43, no. 16, p. 3889, Aug. 2018.

[45] B. Ndagano, N. Mphuthi, G. Milione, and A. Forbes, "Comparing mode-crosstalk and mode-dependent loss of laterally displaced orbital angular momentum and Hermite–Gaussian modes for free-space optical communication," *Optics Letters*, vol. 42, no. 20, p. 4175, Oct. 2017.

[46] B. Ndagano, I. Nape, M. A. Cox, C. Rosales-Guzman, and A. Forbes, "Creation and detection of vector vortex modes for classical and quantum communication," *Journal of Lightwave Technology*, vol. 36, pp. 292–301, 2017.

[47] M. A. Cox, L. Cheng, C. Rosales-Guzmán, and A. Forbes, "Modal Diversity for Robust Free-Space Optical Communications," *Physical Review Applied*, vol. 10, no. 2, p. 024 020, Aug. 2018.

[48] M. Uysal, C. Capsoni, Z. Ghassemlooy, A. Boucouvalas, and E. Udvary, Eds., *Optical Wireless Communications*, ser. Signals and Communication Technology. Cham: Springer International Publishing, 2016.

[49] J. Wang, J. Y. Yang, I. M. Fazal, N. Ahmed, Y. Yan, B. Shamee, A. E. Willner, K. Birnbaum, J. Choi, B. Erkmen, S. Dolinar, and M. Tur, "25.6-bit/s/Hz spectral efficiency using 16-QAM signals over pol-muxed multiple orbital-angular-momentum modes," in *IEEE Photonic Society 24th Annual Meeting, PHO 2011*, 2011, pp. 587–588.

[50] J. Wang, S. Li, M. Luo, J. Liu, L. Zhu, C. Li, D. Xie, Q. Yang, S. Yu, J. Sun, X. Zhang, W. Shieh, and A. E. Willner, "N-dimentional multiplexing link with 1.036-Pbit/s transmission capacity and 112.6-bit/s/Hz spectral efficiency using OFDM-8QAM signals over 368 WDM pol-muxed 26 OAM modes," in *European Conference on Optical Communication, ECOC*, Institute of Electrical and Electronics Engineers Inc., Nov. 2014.

[51] A. E. Siegman, *Lasers*. University Science Books, 1986, p. 1283.

[52] ——, "Hermite-gaussian functions of complex argument as optical-beam eigenfunctions," *Journal of the Optical Society of America*, vol. 63, no. 9, p. 1093, Sep. 1973.

[53] A. Forbes, *Laser Beam Propagation: Generation and Propagation of Customized Light*, A. Forbes, Ed. CRC Press, 2014, p. 364.

[54] C. Rosales-Guzmán and A. Forbes, *How to shape light with spatial light modulators*. SPIE Press, p. 57.

[55] L. Allen, M. W. Beijersbergen, R. J. C. Spreeuw, and J. P. Woerdman, "Orbital angular momentum of light and the transformation of Laguerre-Gaussian laser modes," *Physical Review A*, vol. 45, no. 11, pp. 8185–8189, Jun. 1992.

[56] B. Rodenburg, M. Mirhosseini, M. Malik, O. S. Magaña-Loaiza, M. Yanakas, L. Maher, N. K. Steinhoff, G. A. Tyler, and R. W. Boyd, "Simulating thick atmospheric turbulence in the lab with application to orbital angular momentum communication," en, *New Journal of Physics*, vol. 16, no. 3, p. 033 020, Mar. 2014.

[57] J. Shapiro, "The Quantum Theory of Optical Communications," *IEEE Journal of Selected Topics in Quantum Electronics*, vol. 15, no. 6, pp. 1547–1569, 2009.

[58] T. Kaiser, D. Flamm, S. Schröter, and M. Duparré, "Complete modal decomposition for optical fibers using CGH-based correlation filters," *Optics Express*, vol. 17, no. 11, p. 9347, May 2009.

[59] Litvin I.A., Dudley A., Roux F.S., and Forbes A., "Azimuthal decomposition with digital holograms," *Optics Express*, vol. 20, p. 10 996, 2012.

[60] D. Flamm, D. Naidoo, C. Schulze, A. Forbes, and M. Duparré, "Mode analysis with a spatial light modulator as a correlation filter.," EN, *Optics letters*, vol. 37, no. 13, pp. 2478–80, Jul. 2012.

[61] G. C. G. Berkhout, M. P. J. Lavery, J. Courtial, M. W. Beijersbergen, and M. J. Padgett, "Efficient sorting of orbital angular momentum states of light.," *Physical review letters*, vol. 105, no. 15, p. 153 601, Oct. 2010.

[62] R. Ryf, N. K. Fontaine, and R.-J. Essiambre, "Spot-Based Mode Couplers for Mode-Multiplexed Transmission in Few-Mode Fiber," *IEEE Photonics Technology Letters*, vol. 24, no. 21, pp. 1973–1976, Nov. 2012.

[63] C. Rosales-Guzmán, N. Bhebhe, N. Mahonisi, and A. Forbes, "Multiplexing 200 spatial modes with a single hologram," *Journal of Optics*, vol. 19, no. 11, p. 113 501, Nov. 2017.

[64] J. Pinnell, V. Rodríguez-Fajardo, and A. Forbes, "Quantitative orbital angular momentum measurement of perfect vortex beams," *Optics Letters*, vol. 44, no. 11, p. 2736, Jun. 2019.

[65] A. Vijayakumar, C. Rosales-Guzmán, M. R. Rai, J. Rosen, O. V. Minin, I. V. Minin, and A. Forbes, "Generation of structured light by multilevel orbital angular momentum holograms," *Optics Express*, vol. 27, no. 5, p. 6459, Mar. 2019.

[66] D. Flamm, M. Duparré, S. Schröter, and T. Kaiser, "Complete modal decomposition for optical fibers using CGH-based correlation filters," *Optics Express*, vol. 17, no. 11, pp. 9347–9356, May 2009.

[67] M. A. Cox, E. Toninelli, L. Cheng, M. J. Padgett, and A. Forbes, "A High-Speed, Wavelength Invariant, Single-Pixel Wavefront Sensor With a Digital Micromirror Device," *IEEE Access*, vol. 7, pp. 85 860–85 866, 2019.

[68] F. S. Roux and Y. Zhang, "Projective measurements in quantum and classical optical systems," *Physical Review A*, vol. 90, no. 3, p. 033 835, 2014.

[69] F. X. Kneizys, E. P. Shettle, L. W. Abreu, J. H. Chetwynd, and G. P. Anderson, "Users guide to LOWTRAN 7," AIR FORCE GEOPHYSICS LAB HANSCOM AFB MA, Tech. Rep., 1988.

[70] H. Kaushal, V. Jain, and S. Kar, *Free Space Optical Communication*, ser. Optical Networks. New Delhi: Springer India, 2017.

[71] A. Berk, P. Conforti, R. Kennett, T. Perkins, F. Hawes, and J. van den Bosch, "MODTRAN6: a major upgrade of the MODTRAN radiative transfer code," M. Velez-Reyes and F. A. Kruse, Eds., vol. 9088, International Society for Optics and Photonics, Jun. 2014, 90880H.

[72] A. N. Kolmogorov, "The local structure of turbulence in incompressible viscous fluid for very large Reynolds numbers," in *Dokl. Akad. Nauk SSSR*, JSTOR, vol. 30, 1941, pp. 301–305.

[73] Andrews, *Laser Beam Propagation through Random Media*, Second. SPIE Press, 2005.

[74] A. Hamadou Ibrahim, F. S. Roux, M. McLaren, T. Konrad, and A. Forbes, "Orbital-angular-momentum entanglement in turbulence," *Physical Review A*, vol. 88, no. 1, p. 012 312, Jul. 2013.

[75] J. B. Breckinridge and D. G. Voelz, *Computational Fourier Optics: A MATLAB Tutorial*. Society of Photo Optical, 2011, p. 232.

[76] D. L. Fried, "Statistics of a Geometric Representation of Wavefront Distortion," *Journal of the Optical Society of America*, vol. 55, no. 11, p. 1427, Nov. 1965.

[77] D. P. Greenwood, "Bandwidth specification for adaptive optics systems," *Journal of the Optical Society of America*, vol. 67, no. 3, p. 390, Mar. 1977.

[78] H. Weichel, *Laser Beam Propagation in the Atmosphere*. SPIE Press, 1990, p. 98.

[79] L. R. Bissonnette and L. R., "Log-normal probability distribution of strong irradiance fluctuations: An asymptotic analysis," *In AGARD Opt. Propagation in the Atmosphere 10 p (SEE N76-29815 20-46)*, 1976.

[80] L. R. Bissonnette and P. L. Wizinowich, "Probability distribution of turbulent irradiance in a saturation regime," *Applied Optics*, vol. 18, no. 10, p. 1590, May 1979.

[81] M. A. Kashani, M. Uysal, and M. Kavehrad, "A Novel Statistical Channel Model for Turbulence-Induced Fading in Free-Space Optical Systems," EN, *Journal of Lightwave Technology*, vol. 33, no. 11, pp. 2303–2312, Jun. 2015.

[82] J. A. Anguita, M. A. Neifeld, and B. V. Vasic, "Modeling channel interference in an orbital angular momentum-multiplexed laser link," A. K. Majumdar and C. C. Davis, Eds., International Society for Optics and Photonics, Aug. 2009, 74640U.

[83] G. A. Tyler and R. W. Boyd, "Influence of atmospheric turbulence on the propagation of quantum states of light carrying orbital angular momentum," EN, *Optics Letters*, vol. 34, no. 2, p. 142, Jan. 2009.

[84] B. Rodenburg, M. P. J. Lavery, M. Malik, M. N. O'Sullivan, M. Mirhosseini, D. J. Robertson, M. Padgett, and R. W. Boyd, "Influence of atmospheric turbulence on states of light carrying orbital angular momentum.," EN, *Optics letters*, vol. 37, no. 17, pp. 3735–7, Sep. 2012.

[85] R. J. Noll, "Zernike polynomials and atmospheric turbulence," *Journal of the Optical Society of America*, vol. 66, no. 3, p. 207, Mar. 1976.

[86] S. Li, S. Chen, C. Gao, and A. E. Willner, "Atmospheric turbulence compensation in orbital angular momentum communications: Advances and perspectives," *Optics Communications*, vol. 408, pp. 68–81, Feb. 2018.

[87] A. T. O'Neil and J. Courtial, "Mode transformations in terms of the constituent Hermite–Gaussian or Laguerre–Gaussian modes and the variable-phase mode converter," *Optics Communications*, vol. 181, no. 1-3, pp. 35–45, Jul. 2000.

[88] N. Chandrasekaran and J. H. Shapiro, "Photon Information Efficient Communication Through Atmospheric Turbulence–Part I: Channel Model and Propagation Statistics," *Journal of Lightwave Technology*, vol. 32, no. 6, pp. 1075–1087, Mar. 2014.

[89] G. Milione, H. I. Sztul, D. A. Nolan, and R. R. Alfano, "Higher-order poincar{é} sphere, stokes parameters, and the angular momentum of light," *Physical Review Letters*, vol. 107, no. 5, p. 53 601, 2011.

[90] C. Rosales-Guzmán, B. Ndagano, and A. Forbes, "A review of complex vector light fields and their applications," *Journal of Optics*, vol. 20, no. 12, p. 123 001, Dec. 2018.

[91] G. Milione, T. A. Nguyen, J. Leach, D. A. Nolan, and R. R. Alfano, "Using the nonseparability of vector beams to encode information for optical communication," *Optics Letters*, vol. 40, no. 21, p. 4887, 2015.

[92] Y. Gu and G. Gbur, "Reduction of turbulence-induced scintillation by nonuniformly polarized beam arrays.," EN, *Optics letters*, vol. 37, no. 9, pp. 1553–5, May 2012.

[93] W. Cheng, J. W. Haus, and Q. Zhan, "Propagation of vector vortex beams through a turbulent atmosphere," *Optics Express*, vol. 17, no. 20, p. 17 829, 2009.

[94] L. Allen, M. W. Beijersbergen, R. J. C. Spreeuw, and J. P. Woerdman, "Orbital angular momentum of light and the transformation of Laguerre-Gaussian laser modes," *Physical Review A*, vol. 45, no. 11, p. 8185, 1992.

[95] D. Naidoo, F. S. Roux, A. Dudley, I. Litvin, B. Piccirillo, L. Marrucci, and A. Forbes, "Controlled generation of higher-order Poincar{é} sphere beams from a laser," *Nature Photonics*, vol. 10, p. 327, 2016.

[96] M. Charnotskii, "Propagation of polarized waves in inhomogeneous media," *Journal of the Optical Society of America A*, vol. 33, no. 7, p. 1385, Jul. 2016.

[97] L. Marrucci, C. Manzo, and D. Paparo, "Optical spin-to-orbital angular momentum conversion in inhomogeneous anisotropic media.," *Physical Review Letters*, vol. 96, no. 16, p. 163 905, Apr. 2006.

[98] R. G. Lane, A. Glindemann, and J. C. Dainty, "Simulations of a Kolmogorov phase screen," *Waves in Random Media*, vol. 2, no. April, p. 209, 1992.

[99] J. Liu and J. Wang, "Demonstration of polarization-insensitive spatial light modulation using a single polarization-sensitive spatial light modulator.," *Scientific Reports*, vol. 5, p. 9959, 2015.

[100] C. Rosales-Guzmán, N. Bhebhe, and A. Forbes, "Simultaneous generation of multiple vector beams on a single SLM," *Optics Express*, vol. 25, no. 21, p. 25 697, Oct. 2017.

[101] A. Forbes, A. Dudley, and M. McLaren, "Creation and detection of optical modes with spatial light modulators," *Advances in Optics and Photonics*, vol. 8, no. 2, p. 200, 2016.

[102] J. H. Churnside and S. F. Clifford, "Log-normal Rician probability-density function of optical scintillations in the turbulent atmosphere," EN, *Journal of the Optical Society of America A*, vol. 4, no. 10, p. 1923, Oct. 1987.

[103] J. Zhou, J. Zong, and D. Liu, "Coupled mode theory for orbital angular momentum modes transmission in the presence of atmosphere turbulence," *Optics Express*, vol. 23, no. 25, p. 31 964, Dec. 2015.

[104] V. P. Aksenov, V. V. Kolosov, G. A. Filimonov, and C. E. Pogutsa, "Orbital angular momentum of a laser beam in a turbulent medium: preservation of the average value and variance of fluctuations," en, *Journal of Optics*, vol. 18, no. 5, p. 054 013, May 2016.

[105] Y. Ren, Z. Wang, G. Xie, L. Li, Y. Cao, C. Liu, P. Liao, Y. Yan, N. Ahmed, Z. Zhao, A. Willner, N. Ashrafi, S. Ashrafi, R. D. Linquist, R. Bock, M. Tur, A. F. Molisch, and A. E. Willner, "Free-space optical communications using orbital-angular-momentum multiplexing combined with MIMO-based spatial multiplexing," *Optics Letters*, vol. 40, no. 18, p. 4210, Sep. 2015.

[106] L. Zou, L. Wang, and S. Zhao, "Turbulence mitigation scheme based on spatial diversity in orbital-angular-momentum multiplexed system," *Optics Communications*, vol. 400, pp. 123–127, 2017.

[107] J. R. Barry, E. A. Lee, and D. G. Messerschmitt, *Digital Communication*, Third. Springer US, 2003.

[108] J. G. Proakis and M. Salehi, *Digital communications*, Fifth. McGraw-Hill, 2008.

[109] D. Brennan, "Linear Diversity Combining Techniques," *Proceedings of the IRE*, vol. 47, no. 6, pp. 1075–1102, Jun. 1959.

[110] E. M. Amhoud, A. Trichili, B. S. Ooi, and M.-S. Alouini, "OAM Mode Selection and Space–Time Coding for Atmospheric Turbulence Mitigation in FSO Communication," *IEEE Access*, vol. 7, pp. 88 049–88 057, 2019.

[111] G. R. Mehrpoor, M. Safari, and B. Schmauss, "Free space optical communication with spatial diversity based on orbital angular momentum of light," in *2015 4th International Workshop on Optical Wireless Communications (IWOW)*, IEEE, Sep. 2015, pp. 78–82.

[112] S. Huang, G. R. Mehrpoor, and M. Safari, "Spatial-Mode Diversity and Multiplexing for FSO Communication With Direct Detection," *IEEE Transactions on Communications*, vol. 66, no. 5, pp. 2079–2092, May 2018.

[113] A. D. Familua and L. Cheng, "First and Second-Order Semi-Hidden Fritchman Markov models for a multi-carrier based indoor narrowband power line communication system," *Physical Communication*, vol. 29, pp. 55–66, Aug. 2018.

[114] S. Trisno, I. I. Smolyaninov, S. D. Milner, and C. C. Davis, "Characterization of time delayed diversity to mitigate fading in atmospheric turbulence channels," D. G. Voelz and J. C. Ricklin, Eds., vol. 5892, International Society for Optics and Photonics, Aug. 2005, p. 589 215.

[115] F. S. Vetelino, C. Young, and L. Andrews, "Fade statistics and aperture averaging for Gaussian beam waves in moderate-to-strong turbulence," *Applied Optics*, vol. 46, no. 18, p. 3780, Jun. 2007.

[116] J. H. Churnside and R. J. Lataitis, "Wander of an optical beam in the turbulent atmosphere," *Applied Optics*, vol. 29, no. 7, p. 926, Mar. 1990.

[117] A. Rodriguez-Gomez, F. Dios, J. A. Rubio, and A. Comeron, "Temporal statistics of the beam-wander contribution to scintillation in ground-to-satellite optical links: an analytical approach," *Applied Optics*, vol. 44, no. 21, p. 4574, Jul. 2005.

[118] R. Esposito, "Power scintillations due to the wandering of the laser beam," *Proceedings of the IEEE*, vol. 55, no. 8, pp. 1533–1534, 1967.

[119] D. L. Fried, "Statistics of Laser Beam Fade Induced by Pointing Jitter," *Applied Optics*, vol. 12, no. 2, p. 422, Feb. 1973.

[120] P. J. Titterton, "Power Reduction and Fluctuations Caused by Narrow Laser Beam Motion in the Far Field," *Applied Optics*, vol. 12, no. 2, p. 423, Feb. 1973.

[121] R. Fante, "Electromagnetic beam propagation in turbulent media," *Proceedings of the IEEE*, vol. 63, no. 12, pp. 1669–1692, 1975.

[122] F. Dios, J. A. Rubio, A. Rodríguez, and A. Comerón, "Scintillation and beam-wander analysis in an optical ground station-satellite uplink," *Applied Optics*, vol. 43, no. 19, p. 3866, 2004.

[123] L. C. Andrews, R. L. Phillips, R. J. Sasiela, and R. Parenti, "PDF models for uplink to space in the presence of beam wander," in *Atmospheric Propagation IV*, C. Y. Young and G. C. Gilbreath, Eds., vol. 6551, International Society for Optics and Photonics, Apr. 2007, p. 655 109.

[124] K. Kiasaleh, "On the probability density function of signal intensity in free-space optical communications systems impaired by pointing jitter and turbulence," *Optical Engineering*, vol. 33, no. 11, p. 3748, Nov. 1994.

[125] G. E. P. Box, G. M. Jenkins, G. C. Reinsel, and G. M. Ljung, *Time series analysis: forecasting and control*. John Wiley & Sons, 2015.

[126] S. Hochreiter and J. Schmidhuber, "Long Short-Term Memory," *Neural Computation*, vol. 9, no. 8, pp. 1735–1780, Nov. 1997.

[127] L. E. Baum and T. Petrie, "Statistical Inference for Probabilistic Functions of Finite State Markov Chains," *The Annals of Mathematical Statistics*, vol. 37, no. 6, pp. 1554–1563, Dec. 1966.

[128] J. Lin, X.-C. Yuan, M. Chen, and J. C. Dainty, "Application of orbital angular momentum to simultaneous determination of tilt and lateral displacement of a misaligned laser beam," *Journal of the Optical Society of America A*, vol. 27, no. 10, p. 2337, Oct. 2010.

[129] M. V. Vasnetsov, V. A. Pas'ko, and M. S. Soskin, "Analysis of orbital angular momentum of a misaligned optical beam," *New Journal of Physics*, vol. 7, no. 1, pp. 46–46, Feb. 2005.

[130] D. J. Geisler, T. M. Yarnall, M. L. Stevens, C. M. Schieler, B. S. Robinson, and S. A. Hamilton, "Multi-aperture digital coherent combining for free-space optical communication receivers," *Optics Express*, vol. 24, no. 12, p. 12 661, 2016.

[131] D. J. Geisler, T. M. Yarnall, C. M. Schieler, G. Lund, M. L. Stevens, B. S. Robinson, and S. A. Hamilton, "Ground Receiver Architectures Enabled by Digital Coherent Combining," in *Advanced Photonics 2018 (BGPP, IPR, NP, NOMA, Sensors, Networks, SPPCom, SOF)*, Washington, D.C.: OSA, Jul. 2018, NeW4F.1.